TAMPEREEN TEKNILLINEN YLIOPISTO
TAMPERE UNIVERSITY OF TECHNOLOGY

Caroline Gaëlle Amiot

Novel Supercontinuum Sensing and Imaging Techniques in the Infrared

Julkaisu 1607 • Publication 1607

Tampere 2018

UBFC
UNIVERSITÉ
BOURGOGNE FRANCHE-COMTÉ

SPIM

Tampereen teknillinen yliopisto. Julkaisu 1607
Tampere University of Technology. Publication 1607

Caroline Gaëlle Amiot

Novel Supercontinuum Sensing and Imaging Techniques in the Infrared

Thesis for the degree of Doctor of Science in Technology to be presented with due permission for public examination and criticism in Rakennustalo Building, Auditorium RG202, at Tampere University of Technology, on the 30th of November 2018, at 15:30.

Tampereen teknillinen yliopisto - Tampere University of Technology
Université de Bourgogne Franche-Comté
Tampere 2018

Doctoral candidate: Caroline Gaëlle Amiot, M.Sc.
Laboratory of Photonics
Faculty of Natural Sciences
Tampere University of Technology
Finland
Université de Bourgogne Franche-Comté
France

Supervisors: Goëry Genty, Prof.
Laboratory of Photonics
Faculty of Natural Sciences
Tampere University of Technology
Finland

John M. Dudley
Institut FEMTO-ST
Faculté des sciences et techniques
Université de Bourgogne Franche-Comté
France

Pre-examiners: Tero Setälä, Prof.
Institute of Photonics
University of Eastern Finland, Joensuu
Finland

Daniele Faccio, Prof.
School of Physics and Astronomy
University of Glasgow
United Kingdom

Opponent: Miguel Alonso, Prof.
The Institute of Optics
University of Rochester
United States of America

ISBN 978-952-15-4273-2 (printed)
ISBN 978-952-15-4289-3 (PDF)
ISSN 1459-2045

ABSTRACT

The ability to detect substances or molecules with high sensitivity and to image objects with high resolution plays an important role in our every-day life as well as in advances in understanding fundamental phenomena. Optical techniques are generally highly beneficial for this purpose as they are intrinsically remote, non-invasive and exhibit superior sensitivity and resolution. It is thus not surprising that a wide range of sensing and imaging techniques have been developed in the past decades and are continuously the subject of intense research. The performance of these methods, on the other hand, depends dramatically on the type of light source that is used, and it is therefore essential to tailor the light source properties to the intended method of application.

A particular spectral range which has recently attracted a wide interest is the mid-infrared corresponding to the molecular fingerprint region and the atmospheric transparency window. This, in turn, has triggered renewed research effort into adapting existing technique to this particular range of the electromagnetic spectrum including the light sources and detection schemes. This thesis belongs to this trend and reports novel, proof-of-concept, broadband optical sensing and imaging techniques in the infrared using supercontinuum light, a class of light sources with unique properties. The techniques are experimentally demonstrated and their performances discussed.

Specifically, the thesis demonstrates incoherent broadband cavity enhanced absorption spectroscopy in the mid-infrared wavelength range from 3000 to 3450 nm. Multi-component gas detection with sub-ppm accuracy is achieved in this range, which constitutes the widest continuous detection range for this technique in the mid-infrared.

Cantilever-enhanced photoacoustic spectroscopy in the mid-infrared is also demonstrated for the first time in this thesis. The approach is broadband and allows for higher photoacoustic signal intensity and enhanced signal-to-noise ratio as compared to conventional systems that use black-body radiation sources. The results offer novel perspective for photoacoustic detection opening the door to sensitive broadband and compact analyzers in the mid-infrared spectral region.

Exploiting the shot-to-shot fluctuations of an incoherent supercontinuum and the recent progress in ultrafast real-time spectral measurement techniques, the thesis finally reports on a novel proof-of-concept correlation sensing and imaging method in the form of spectral-domain ghost imaging. The method is fast, scan-free, and offer new opportunities for remote sensing in scattering and absorbing media, or in spectral regions where sensitive detectors are lacking. Application of this technique to broadband spectroscopic measurements gases as well as for interferometric imaging of physical objects is demonstrated. One can legitimately anticipate that the work presented in this thesis will foster new ideas and developments for optical sensing and imaging.

RÉSUMÉ

La détection sensible de substances ou molécules et l'imagerie à haute résolution sont une composante essentielle de la vie quotidienne. Elles jouent également un rôle fondamental dans la compréhension de nouveaux phénomènes physiques. Les méthodes de mesure optiques sont très performantes avec une sensibilité et une résolution généralement supérieures aux autres techniques, et elles possèdent aussi l'avantage d'être sans contact et non invasives. Il n'est donc pas surprenant qu'un grand nombre de techniques optiques de détection et d'imagerie se soient développées au cours des dernières décennies et fassent continuellement l'objet de nombreuses recherches. Les performances de ces méthodes dépendant de manière significative du type de source de lumière utilisé, il est essentiel d'optimiser les propriétés de la source pour l'application envisagée.

L'infrarouge moyen correspond à la région spectrale des empreintes moléculaires ainsi qu'à la fenêtre de transparence atmosphérique. Elle a donc un fort potentiel pour de multiples applications dans des domaines variés allant des communications en espace libre jusqu'au domaine médicale ou la détection des gaz à effet de serre. La détection et l'imagerie dans cette région du spectre électromagnétique a ainsi récemment fait l'objet d'un large intérêt et d'efforts de recherche afin d'adapter les techniques de mesures existantes, y compris les sources de lumière et les méthodes de détection. Cette thèse introduit plusieurs nouvelles techniques de détection optique et d'imagerie basées sur l'utilisation de sources supercontinuum dans l'infrarouge. Les propriétés uniques de ce type de source lumineuse, en particulier leur large bande spectrale combinée à une cohérence spatiale parfaite, permettent d'obtenir des performances supérieures en terme de résolution ou de sensibilité. Les techniques proposées sont expérimentalement démontrées et leurs performances caractérisées.

Spécifiquement, la thèse démontre une technique de spectroscopie par absorption en cavité résonnante dans l'infrarouge moyen sur une plage spectrale allant de 3000 à 3450 nm. La détection simultanée de plusieurs gaz à l'état de trace avec une précision inférieure au ppm est obtenue, ce qui constitue la plus large plage de détection continue avec cette approche dans l'infrarouge moyen.

Une technique de spectroscopie par effet photo-acoustique est également démontrée, pour la première fois dans l'infrarouge moyen. L'approche est large bande et permet d'obtenir une plus grande intensité de signal photo-acoustique et un meilleur rapport signal à bruit par rapport aux systèmes conventionnels utilisant un corps noir. Ces résultats offrent une nouvelle perspective pour la détection photo-acoustique, ouvrant la porte aux analyseurs compacts, sensibles et sur une large plage spectrale large dans l'infrarouge moyen.

En s'appuyant sur les fluctuations spectrales d'une source supercontinuum et les récents progrès des mesures de spectre en temps réel, la thèse introduit un nouveau concept de détection et d'imagerie par corrélations, équivalent à l'imagerie fantôme mais dans le domaine spectral. La méthode est rapide, sans balayage et offre de nouvelles possibilités pour la détection à distance de matériaux diffusant et absorbant, ou bien à des longueurs d'onde où des détecteurs sensibles font défaut. L'application de cette technique à la spectroscopie par absorption ainsi qu'à la tomographie par cohérence optique d'objets physiques est démontrée. Les techniques proposées et étudiées dans cette thèse peuvent être encore perfectionnées et leurs performances améliorées, mais de manière plus générale les travaux présentés dans ce manuscrit ont vocation à susciter de nouvelles idées et de nouveaux développements en matière de détection et d'imagerie optiques.

PREFACE

This work was co-supervised and carried out between the laboratory of Photonics of Tampere University of Technology, the FEMTO-ST Institute and the Université de Bourgogne Franche-Comté. I would like to acknowledge financial support from the doctoral school of Tampere University of Technology.

I would like to thank deeply my main supervisor Prof. Goëry Genty for offering me the opportunity to join the former Optics laboratory for my master thesis and to continue my work as a co-supervised PhD. Thank you for the endless guidance, support and kindness. Thank you for your time and your incredible patience. It was a real pleasure to work with such a passionate researcher.

I would also like to thank my second supervisor Prof. John Dudley aka Dr House for our fruitful conversations and his focused guidance during my stays in Besançon.

I would like to express my gratitude to my co-authors for their help with the experimental setups, the simulations and all fruitful discussions. Specific mention to Prof. Ari Friberg for enlightening conversations on coherence and advance billiard techniques.

Special thanks to the leading trio of SK1, namely Martti, Goëry and Juha. You have been able to create a great place to work with friendly atmosphere. Your numerous laughs will be remembered in those corridors forever.

I would like to thank especially the other members of the UKO group, Piotr, Shanti, Zahra, Lauri, Roosa and the former members Jani, Mathilde and Han to cite only few. The endless discussions, the multiples movies and escape rooms, and the far too many chicken wings are memories that I will never forget.

I would like to thank my roommates, Jan and Tommi for their friendliness, nice conversations and above all, their little part of craziness that made The_Inky_Banana possible. Many thanks also to Léo, Kim, Sreekanth, Abba, my lunch buddies and the other members of the Photonics lab for the great working atmosphere and for all the nice conversations.

J'aimerais aussi remercier toutes les personnes de FEMTO-ST et de la fac de sciences que j'ai eu le plaisir de rencontrer, mes enseignants qui ont créé mon envie de poursuivre mes études en optique et mes compères de l'Aqua et d'ailleurs qui m'ont prouvé qu'il n'y avait pas que la recherche dans la vie, mais aussi la coinche! Merci à Sandrine et son grain de folie. Merci à la fine équipe d'OPTO pour les nombreuses conversations et cafés partagés. Merci également à Francis pour les bons moments, les séances de révisions de partiels au labo E et à la BU n'étaient que le début d'une grande histoire.

J'aimerais remercier infiniment ma famille, Papi, Mamie, Vano, Miloche et Claudius, pour leur soutien sans faille, pour les conversations téléphoniques qui n'en finissaient pas, pour les colis qui rendaient mes compagnons de bureau envieux et les nombreux fous-rires qui resteront à jamais gravés dans ma mémoire. Merci d'avoir été là tout au long de cette épreuve. Enfin, merci à mon partenaire de coeur d'avoir toujours cru en moi, d'avoir supporté mes humeurs dans les moments difficiles et d'avoir été ma lumière dans ce long et sombre tunnel. Une pensée émue pour ceux qui ne sont plus mais qui resteront toujours à mes cotés quoi qu'il arrive.

Tampere 31.10.2018

Caroline

CONTENTS

LIST OF SYMBOLS AND ABBREVIATIONS

Nomenclature

a_k	low-order polynomial coefficients
B	spectral radiance density
BW	bandwidth
c	speed of light in vacuum
corr	correlation function
D	dispersion
d	distance
f	frequency
g	spectrometer response function
h	Planck constant
I	intensity
k	Boltzmann constant
L	length
N	number density
n_{ref}	refractive index
P	power
R	reflectivity
S	acoustic signal
t/T	time/re-scaled time
T	temperature
T_0	temporal period of the interferogram
v	speed of scanning mirror
z	distance

α	absorption coefficient
β_2	group velocity dispersion
Γ	autocorrelation/coherence function
δ	Kronecker symbol
δd	optical path difference
$\delta\lambda$	spectral resolution
δz	axial resolution

λ	wavelength
ν	frequency
ρ	transmission
σ	absorption cross-section
τ_{rd}	cavity ring-down time
ω	angular frequency

Acronyms

BS	Beam splitter
CCD	Charge-coupled device
CEAS	Cavity-enhanced absorption spectroscopy
CE-PAS	Cantilever-enhanced photoacoustic spectroscopy
CRDS	Cavity ring-down spectroscopy
DOAS	Differential optical absorption spectroscopy
DCM	Dispersion compensation module
DFT	Dispersive Fourier transform
DGI	Differential ghost imaging
DSF	Dispersion-shifted fiber
FF	Fast frame
FT-IR	Fourier transform infrared
FWM	Four-wave mixing
GI	Ghost imaging
LED	Light emitting diode
LPF	Long-pass filter
NBF	Narrow-band filter
OCT	Optical coherence tomography

OPA	Optical parametric amplifier
OPO	Optical parametric oscillator
OSA	Optical spectrum analyzer
PA	Photoacoustic
PAS	Photoacoustic spectroscopy
SC	Supercontinuum
SLED	Superluminescent LED
SMF	Single-mode fiber
SNR	Signal-to-noise ratio
SPM	Self-phase modulation
TDLAS	Tunable direct laser absorption spectrometry
ZBLAN	ZrF_4-BaF_2-LaF_3-AlF_3-NaF
ZDW	Zero-dispersion-wavelength
ZPD	Zero-path difference

LIST OF PUBLICATIONS

I Caroline Amiot, Antti Aalto, Piotr Ryczkowski, Juha Toivonen and Goëry Genty "Cavity enhanced absorption spectroscopy in the mid-infrared using a supercontinuum source," Applied Physics Letters, vol 111, no. 061103, 2017.

II Tommi Mikkonen, Caroline Amiot, Antti Aalto, Kim Patokoski, Goëry Genty and Juha Toivonen "Broadband cantilever-enhanced photoacoustic spectroscopy in the mid-IR using supercontinuum," Optics Letters, vol 43, no. 20, pp. 5094-5097, 2018.

III Caroline Amiot, Piotr Ryczkowski, Ari T. Friberg, John M. Dudley and Goëry Genty, "Supercontinuum spectral-domain ghost imaging," Optics Letters, vol 43, no. 20, pp. 5025-5028, 2018.

IV Caroline Amiot, Piotr Ryczkowski, Ari T. Friberg, John M. Dudley and Goëry Genty, "Ghost optical coherence tomography," Submitted to Optics Letters.

AUTHOR'S CONTRIBUTION

The thesis consist of four publications related to the development of novel sensing and imaging technique in the infrared. A short description of the publications and the author's contribution is given below.

Publication I. The author developed the supercontinuum source and detection setup to perform the experiment in the mid-infrared. The author conducted the experiments with the help of Dr Piotr Ryczkowski. The author contributed to the data analysis and prepared the manuscript.

Publication II. The author developed the supercontinuum source and contributed to the data analysis. The experiments were mostly performed by Tommi Mikkonen. The author contributed to the preparation of the manuscript along with the co-authors.

Publication III. The author developed and built the experimental setup with the help of Dr Piotr Ryczkowski. The author performed all the measurements, data analysis and contributed to the manuscript preparation along with the co-authors.

Publication IV. The author developed and built the experimental setup with the help of Dr Piotr Ryczkowski. The author conducted all the measurements, data analysis and contributed to the manuscript preparation along with the co-authors.

1. INTRODUCTION

Optics and photonics play a central role in the development of new technologies which revolutionize our everyday life. From lighting to internet, communication, or smartphones, many of the modern technologies operate on physical principles first observed, studied and developed in optics and photonics research laboratories. Equally important to the emergence of new technologies, optics and photonics have often set the standards when it comes to measuring or characterizing physical phenomena, matter or dynamic processes with precision, providing robust, non-invasive and extremely sensitive techniques. For example in medicine, the ability to perform 3D non-destructive imaging of biological samples without contrast agents and with high resolution is essential and methods such as optical coherence tomography are nowadays routinely used in hospitals [1–4]. Detecting very small mount of specific gases emitted by cancerous cells in the breath has been proven to be an effective approach for early detection of lungs and breast cancers [5–7]. More generally, optical imaging and sensing techniques are not only paramount in the medical field, but also in a wide range of application domains including environmental monitoring to follow the concentration of greenhouse gases in the atmosphere or control the level of emissions of pollutants from industry and cars, industrial manufacturing and quality control.

Light sources are central to optical imaging and sensing measurements. Not only the illumination pattern and wavelength must be uniquely considered, but optimum performances often require light sources with specific characteristics in terms of intensity, spectrum, temporal behavior or coherence. Most of optical imaging and sensing methods are generally very sensitive in bright light levels, but their performances may be degraded in low or diffuse light conditions. In the mid-infrared, the lack of suitable bright and broadband light sources on one hand, and the lack of fast and sensitive detectors on the other hand, has slowed down the development of high-speed, high-resolution imaging and sensitive detection solutions. Yet, this spectral region is of tremendous interest, containing the characteristic vibrational transitions of many important molecules and measurement techniques that can capture their spectral signature are key to measure their concentrations or to identify the various chemical components in a mixture. In fact, applications of mid-infrared sensing and imaging go far beyond the detection of specific molecules with potential for remote detection of materials, identification of suspect counterfeit samples, chemical structural confirmation, imaging through skins, or label-free molecular analysis and recognition of important biochemical markers just to name a few [8–11]. It should then be clear that any research effort to develop methods that can potentially allow for progress in sensitivity, resolution, or speed is worth pursuing and there are indeed truly revolutionary applications that will emerge if we can perform remote detection and imaging in the mid-infrared with accuracy similar to what can be achieved in the visible.

For many optical sensing and imaging techniques, light sources that can combine a high brightness with a broad emission spectrum represent a significant advantage, allowing for improved resolution and sensitivity, extended operation wavelength range and thereby wider application scope. However, for many decades, high brightness and large bandwidth were incompatible characteristics. One generally had to choose between bright coherent laser sources, emitting light over a very narrow range of wavelengths but that can be collimated over extended distances, or thermal incoherent emitters with very broad emission spectra but lower spectral density and limited collimation distance. Recently, the emergence of a novel class of light source in the form of optical fiber-based supercontinuum generation with ultra broad spectrum, high brightness and near perfect spatial coherence has revolutionized many of the existing optical measurement techniques, allowing to improve their performance to unprecedented levels [12]. It is thus not surprising that research into sensing and imaging has started taking advantage of the unique properties of supercontinuum light sources. This thesis falls into this framework and presents studies of novel broadband sensing and imaging techniques in the near and mid-infrared using supercontinuum sources, reporting important advances with significant potential for further development and future use.

1.1 Research objectives and scope of the thesis

The overall motivation behind this thesis is to design and perform experiments to demonstrate that supercontinuum sources are an ideal choice for broadband sensing and imaging in the infrared spectral region. Two of the demonstrated approaches are well-established yet combining them with a new specifically tailored light source leads to new capabilities. Two other techniques are completely new and the use of a supercontinuum source was central to their proof-of-concept demonstration. The thesis work is thus mostly of experimental nature, and the reported results are compared with theoretical models or validated using other methods.

Specific individual objectives of this thesis are summarized as follows:

- Development of a supercontinuum source that extends to the mid-infrared range for trace gas detection
- Demonstration for the first time of broadband cavity-enhanced absorption spectroscopy in the mid-infrared for multi-species trace gas detection
- First demonstration of background-free photoacoustic spectroscopy in the mid-infrared with supercontinuum for gas detection
- First proof-of-concept demonstration of ghost imaging in the spectral domain using a supercontinuum source as a random spectral pattern generator
- Application of spectral-domain ghost imaging to broadband spectroscopy and optical coherence tomography.

All these goals have been attained and while the reached performances are perfectible, the studies conducted and obtained results are very promising, and certainly refinements can be expected in the very near future. In fact, extension of the work reported in this thesis is already carried out as these lines were written.

1.2 Structure of the dissertation

This thesis consists of six chapters, starting with an introduction on absorption spectroscopy and the different associated methods. Light sources that are commonly employed are briefly surveyed with special attention being paid to supercontinuum generation, a spectacular spectral broadening process that plays a central role in the work reported in this thesis. This chapter serves as the general background to understand the framework of the experiments reported in the following chapters.

Chapter 3 discusses in detail the technique of cavity-enhanced absorption spectroscopy. After a section dedicated to the general operation principle of the technique, specific application in the mid-infrared using a supercontinuum source is described, starting from the light source and experimental setup to the detection scheme and data post-processing. Measurements of acetylene and methane are analyzed with results reported in Publication I.

Chapter 4 focuses on photoacoustic spectroscopy. After an introduction to the operation principle, key elements of the experimental setup including Fourier transform infrared spectrometer and cantilever detection system are discussed separately. This is followed by the presentation of absorption spectra of water vapor and methane measured in the mid-infrared with a supercontinuum source. The results are put into perspective using comparison with measurements from a conventional black body radiator. This work is reported in Publication II.

Chapter 5 reports a new approach to sensing and imaging in the form of spectral-domain ghost imaging. After a general introduction to the technique of spatial ghost imaging, its transposition to the spectral domain is discussed along the specific requirements for the light source. Particular attention is paid to the dispersive Fourier transform, the method used to measure the spectral fluctuations in real time. A detailed description for the experimental setup, data acquisition and various post-processing steps is provided. Application of the technique to both sensing and imaging in the form of absorption spectroscopy and optical coherence tomography, respectively, is then reported with results appearing in Publications III and IV.

Finally, Chapter 6 summarizes the results obtained in the thesis and share suggestions on future developments.

2. ABSORPTION SPECTROSCOPY

2.1 Introduction

Spectroscopy is the study of interaction between matter and electromagnetic radiation. It is crucial for identifying specific signatures of molecules or compounds and measuring precisely their concentration. The first spectroscopic experiments were performed in the 19th century [13,14]. In these first experiments, the emission spectrum of salt compounds was measured by using a prism to disperse the spectrum of a flame where the salts where burnt and comparing it with the spectrum of the flame in the absence of burning salts. The specific emission pattern of the salts was then used to determine their exact atomic composition.

Another spectroscopic method that was subsequently developed is based on the absorption of electromagnetic radiation rather than emission [15]. Specifically, the light emitted by a broadband source and propagating in a low-density gas is absorbed by the gas at some specific wavelengths which represent the spectral signature of the gas composition. Dispersing the spectrum of the broadband light after interaction with the gas using e.g. a prism just as in emission spectroscopy allows to identify the unique spectral absorption patterns associated with a specific gas and retrieve both its composition and concentration. Gas lamps were originally used to calibrate spectroscopic measurement systems due to their inherent narrow emission lines which allowed them to be used as a wavelength ruler.

Emission and absorption spectroscopy have been extensively used to study gas samples as well as the atmosphere and stars composition [16,17]. Nowadays, absorption spectroscopy is routinely used in many applications including atmospheric measurements, breath analysis, chemical kinetics or industrial process monitoring [18–24].

In this chapter, the different methods commonly utilized for absorption spectroscopy are briefly reviewed and the different types of light sources that can be employed to perform spectroscopic measurements using these methods are described. This sets the framework for the work reported in the subsequent chapters.

2.2 Measurement techniques

Absorption spectroscopy techniques may be divided coarsely into two different categories: direct techniques and cavity-enhanced methods. Direct techniques include Fourier transform infrared (FT-IR) spectroscopy [25, 26], tunable direct laser absorption spectrometry (TDLAS) [27], and its extension to wavelength or frequency modulated spectroscopy (WMS and FMS) [28, 29]. Cavity-enhanced methods on the other hand use an optical cavity to increase light-matter interaction and are generally more sensitive. These include cavity ring down spectroscopy (CRDS) [30], cavity enhanced spectroscopy (CEAS) (also sometimes referred to as integrated cavity output spectroscopy) [31], and noise immune cavity enhanced-optical heterodyne molecular spectroscopy (NICE-OHMS) [32]. All the techniques essentially measure the intensity of light transmitted through a given sample to evaluate its absorption by comparison with the initial light intensity (i.e. before interaction with the sample). Photoacoustic spectroscopy (PAS), on the other hand, is a direct technique which, unlike other methods, detects the amount of light absorbed rather than that transmitted through the sample.

2.2.1 Direct methods

The most basic method for absorption spectroscopy is the so-called differential optical absorption spectroscopy (DOAS). In DOAS, one compares the spectrum $I_0(\lambda)$ of a light source after light passes through an empty cell or a cell filled with inert gas such as N_2, with the spectrum $I(\lambda)$ measured after the cell has been filled with the gas of interest. When light propagates through the cell filled with the gas sample, specific spectral components are absorbed by the gas transitions. The magnitude and linewidth of the absorption lines depend on the gas composition, concentration, pressure, temperature but also on the optical interaction path. The absorption of light by the gas follows the exponential Beer-Lambert law [33] and can be simply retrieved from the ratio $I_0(\lambda)/I(\lambda)$. The sensitivity of the DOAS method can be improved by increasing the interaction path between light and the gas sample, which effectively leads to stronger absorption lines.

The most basic and simplest methods for absorption spectroscopy is so-called direct absorption spectroscopy (DAS). This technique consists in sending light from a laser source through a cell containing a sample and measuring the intensity at the cell output. When a sample is present in the cell, the intensity transmitted through the cell will decrease in proportion to the absorbance of the sample at the laser wavelength (and thus to the sample concentration). Specifically, if $I_0(\lambda)$ is the incident intensity, the intensity transmitted through the cell $I(\lambda)$ is given by the Beer-Lambert law:

$$I(\lambda) = I_0(\lambda)e^{-\alpha(\lambda)d}, \tag{2.1}$$

where $\alpha(\lambda)$ represents the (wavelength-dependent) absorption coefficient of the sample and is related to the number density of absorbers N as $\alpha(\lambda) = \sigma(\lambda)N$ with $\sigma(\lambda)$ the wavelength-dependent absorption cross-section of the absorbers. The wavelength-dependence of the sample absorption can be measured using a tunable laser diode that can scan across a wide wavelength range (so called TDLAS method). Although extremely simple, this technique is usually not very sensitive due to the small variations that needs to be detected in the intensity when the sample concentration is low, which makes the measurement highly susceptible to technical noise. The sensitivity may be increased by increasing the interaction path between light and the sample (up to several tens of meters) using a multi-pass cell with mirrors at both ends of the cells allows for folding the interaction path [34]. Multi-pass cells typically posses a hole in one of the mirrors to couple light in and out (at different angles).

On the other hand, FT-IR spectroscopy relies on the interference of a broabdand light source with a delayed replica of itself. Specifically, broadband light is sent through an interferometer with variable optical path difference. As the path difference is scanned continuously, different spectral components interfere resulting in an interferogram as a function of the optical path difference. The Fourier transform of the recorded interferogram corresponds to the optical spectrum of the transmitted light. Comparison of the spectrum measured with and without the sample present at the input of the interferometer yields the absorption spectrum of the sample. [25,26]

Another way to increase the sensitivity of direct absorption spectroscopy is to modulate the wavelength (or frequency) of the probe laser [28,29]. The idea is to modulate periodically the laser central wavelength with a RF signal and detect the transmitted intensity at a harmonic frequency. This approach allows for reducing significantly the susceptibility of DAS to technical noise and can be readily implemented via direct current modulation of laser diodes (visible) or with external electro-optic modulators (near-infrared).

2.2.2 Cavity-enhanced methods

Cavity ring down spectroscopy

Cavity ring-down spectroscopy (CRDS) performs time-based measurements rather than intensity-based measurements. More specifically, CRDS consists in measuring the change in the photon lifetime inside a high-finesse cavity resulting from the absorption by a sample placed inside this cavity [30,35–37]. Light is sent through the high finesse cavity containing e.g. a gas sample and, when the light source is turned off, the intensity of the light trapped inside the cavity exponentially decays with time. The decay rate is directly linked with the absorption inside the cavity and therefore the gas concentration. One can also use short pulses of light which sequentially exit the cavity with a reduced amplitude following an exponential decay. The temporal variation of the intensity $I(t)$ measured by a detector at the cavity output is given by:

$$I(t) = I_0 e^{-t/\tau_{rd}}, \tag{2.2}$$

where I_0 is the intensity of light injected into the cavity and τ_{rd} is the cavity ring down time related to the mirrors reflectivity R, the cavity length d and the sample absorption $\alpha(\lambda)$ as:

$$\frac{1}{\tau_{rd}} = \frac{(1-R)c}{d} + \alpha(\lambda)c, \tag{2.3}$$

with c being the speed of light. CRDS was originally performed using narrowband lasers which limited the detection to a specific absorption line of one gas specie. Broadband CRDS that utilizes light sources with a broad emission spectrum has also been developed, coupling multiple lasers into a high-finesse cavity and detecting the intensity decay rate using a Fourier transform infrared (FT-IR). Another approach to broadband CRDS relies on separating the different spectral components at the cavity output using a diffraction grating and send them onto a 2D CCD camera to simultaneously measure the decay rate of the different spectral components. The sensitivity of CRDS depends on the light source wavelength stability and the measurement accuracy of the transmitted intensity. Active matching and stabilization of the laser wavelength with the modes of the optical cavity is also required [38]. This is because a long measurable ring-down time is only obtained for laser wavelengths in resonance with a cavity mode. An advantage of the CRDS scheme is that it is not susceptible to intensity variations of the light source.

Cavity-enhanced absorption spectroscopy

Cavity-enhanced absorption spectroscopy (CEAS) (also referred to as integrated cavity output spectroscopy) is a variation of the CRDS method [38]. In this technique, instead of measuring the time-resolved transmitted intensity at the cavity output, one measures the total (i.e. time-integrated) intensity transmitted through the optical cavity while the laser wavelength is tuned over the absorption features of the sample under test. However, just as CRDS, this approach is highly sensitive to the mode structure of the optical cavity as the transmission strongly depends on whether the laser wavelength is on or off-resonance with a cavity mode. There are different approaches to obtain a stable transmission as the laser wavelength is scanned. One may lock the laser wavelength to the cavity modes such that the laser wavelength constantly matches with one of the cavity modes (so-called mode-matching). This approach allows for extremely long interaction lengths but it is also very susceptible to external perturbations and possible saturation effects. An alternative is to modulate rapidly the cavity length (via e.g. a piezoelectric actuator attached to one of the mirrors) to prevent mode matching (so called anti-mode-matching) between the laser wavelength and the cavity [39]. The interaction length is effectively reduced but the transmission is quasi-constant over time and independent of the laser wavelength. The main advantage of CEAS is that it can be combined with a broadband incoherent light source in order to cover a large wavelength span and detect multiple species simultaneously [39,40, Publication I]. Yet, it is essential that the intensity of the light source is constant over the integration time of the cavity output intensity. Furthermore, when using mirrors with high reflectivity to increase the method sensitivity, the transmission of the cavity is low, such that one generally needs a light source with high brightness and highly sensitive system to measure the transmitted spectrum. A reliable calibration procedure is also necessary to determine with precision the wavelength-dependent background optical losses of the system using e.g. known concentrations of specific sample in the cavity. This method is described in more details in Chapter 3 and was used in the work reported in Publication I.

Noise-immune cavity-enhanced optical-heterodyne molecular spectroscopy

Noise-immune cavity-enhanced optical-heterodyne molecular spectroscopy (NICE-OHMS) combines CEAS with the laser frequency modulation approach described above in order to reduce the susceptibility of CEAS to technical noise [32]. When the laser is modulated and locked at a frequency equal to the free-spectral range of the cavity, the central frequency as well as the frequency components of the modulation are perfectly transmitted through the cavity. A direct consequence is that the scheme does not convert potential laser (frequency) noise into amplitude noise, which is why this technique is called noise-immune. The technique therefore combines both the advantage of CEAS with long interaction lengths and that of the frequency modulation scheme which limits the electrical signal to a narrow frequency band, thus largely reducing the electrical noise.

2.2.3 Other methods

Photoacoustic spectroscopy

Photoacoustic spectroscopy (PAS) is based on the photoacoustic effect [41–43]. Light absorbed by a sample induces an energy transition to a higher energy state, followed by relaxation to the initial low energy state caused by spontaneous emission or non-radiative decay. The energy released as a result of the non-radiative decay process gives rise to a temperature increase in the sample. Modulating the incident light at an acoustic frequency (e.g. using a mechanical chopper) therefore changes periodically the temperature of a sample placed in an acoustic cell, which in turn induces periodical variations in the pressure. These pressure changes translate into an acoustic wave which can be detected with e.g. a sensitive microphone. The absorbed intensity I_{abs} is given by:

$$I_{abs} = I_0 - I_0 e^{-\alpha(\lambda)d}, \tag{2.4}$$

where I_0 is the incident intensity and d is the length of the photoacoustic cell. For small absorption values, the absorbed intensity I_{abs} can be approximated as:

$$I_{abs} = I_0 - I_0 e^{-\alpha(\lambda)d} \sim I_0 \alpha(\lambda) d \tag{2.5}$$

and the acoustic energy produced by the absorption of the radiation is therefore directly proportional to the incident intensity I_0.

A significant advantage of PAS is therefore that, unlike the above-mentioned methods, it is a background-free technique with the amplitude of the detected acoustic signal directly proportional to the absorption in the sample, which makes it a particularly sensitive technique. The sensitivity can be further enhanced by using resonant acoustic cells or cantilever detection [44,45]. Broadband PAS can also be implemented using a broadband incoherent source where each wavelength is modulated at acoustic frequencies using a Fourier transform interferometer and measuring the corresponding acoustic signals at the cell output [46]. This method is described in more detail in Chapter 4 and was used in the work reported in Publication II.

Dispersive Fourier transform spectroscopy

When used with a broadband light source, all the methods described above typically use a scanning monochromator and a detector, or a grating spectrometer with a charge-coupled device (CCD) to disperse spatially and measure separately the different spectral components. This also means that the measurements are performed over a finite integration time such that ultra-fast changes in the sample composition or concentration can not generally be probed. Recently, a new technique that disperses in time the different spectral components of a broadband light source interacting with a given sample has been developed, allowing to probe changes in the composition or concentration on ultra-fast time scales. The technique consists in using a dispersive medium such as a highly dispersive optical fiber or a fiber Bragg-grating placed after the sample to separate in time the spectral components of a pulsed source [47,48]. The dispersive medium effectively acts as a Fourier transform such that the temporal trace measured with a fast photodiode and real-time oscilloscope corresponds to the spectrum of the light source absorbed by the gas. Such a dispersive Fourier transform (DFT) technique is simple to implement and extremely fast with the possibility to measure single-shot spectra up to the GHz rate (sub ns). The resolution of the technique is determined by the total amount of dispersion of the fiber (or grating) and sub-pm resolution has been demonstrated using this technique [48–50]. The dispersive Fourier transform approach is discussed in more details in Chapter 5 where its principle is partly exploited in the work reported in Publications III and IV.

Spectral ghost imaging

In contrast with the direct measurement methods described above, correlation imaging measures the correlation function between the intensity emitted by a light source and the total (integrated) intensity transmitted (or reflected) by an object, such that the image can be constructed without the object to be actually seen [51–53]. The essential nature of such ghost imaging lies in the mutual spatial correlation of the two beams, and the image can be simply obtained by summing all of the probing patterns, each weighted by the integrated signal from the detector. By adapting and transposing this technique originally developed to generate images of real physical objects into the spectral domain, once can perform indirect absorption spectroscopic measurements as demonstrated in Publication III. In this case, a pulsed incoherent light source is used as the origin of spectral fluctuations and light is split between two arms: the reference and the test arms. In the reference arm, the spectral fluctuations are measured in real (using e.g. the DFT technique). In the test arm, light propagates through a gas sample to be analyzed and the total intensity integrated over the entire wavelength range is measured by a slow photodiode. Thousands of single-shot spectra are recorded with a fast oscilloscope simultaneously to the integrated intensity signal from the slow detector. By correlating the single-shot spectra from the reference arm which have not interacted with the gas and the total signal from the test arm one can reconstruct the absorption spectrum of a given sample. The advantage of the correlation approach is that it only detects the total integrated signal after the object and thus can be in principle very sensitive even in low light conditions or in spectral regions where no fast detector exists. It is also inherently insensitive to any perturbation occurring between the object and the detector. The resolution of the technique is determined by the resolution with which the spectral fluctuations are measured in real time in the reference arm. Such a spectral domain ghost imaging approach can be extended to perform imaging of real physical objects using the principles of optical coherence tomography and this is demonstrated in Publication IV.

2.3 Light sources

When considering a light source for spectroscopic (or imaging) applications, there are several parameters that should be considered including intensity or power, bandwidth, coherence (spatial and temporal), temporal behavior (continuous wave or pulsed source), noise characteristics, and possible tunability. And indeed the performances of the spectroscopy techniques presented in the previous section depend significantly on the type of light source that is used. For example, higher brightness yields enhanced sensitivity while larger spectral bandwidth allows for detection of multiple species. Figure 2.1 shows a summary of the different types of available light sources and their emission characteristics (wavelength span and intensity) in relation to the absorption properties of common trace gases.

2.3.1 Continuous-wave lasers

Continuous-wave laser sources are quasi-monochromatic, narrow band, with high temporal and spatial coherence and usually compact and cheap. These make them ideal light sources for multiple applications. However in spectroscopy, their fixed emission wavelength and narrow linewidth restrict their use to the detection of a specific gas or liquid. Tunable lasers such as external cavity lasers, on the other hand, offer a narrow linewidth with the possibility of scanning the emission wavelength across an extended range of wavelengths [54, 55]. The tunability may reach up to some hundred nanometers but this is generally at the expense of the brightness, which is not as high as that of fixed wavelength laser sources. Furthermore, their operating wavelength range is typically restricted to the near-infrared and the limited scanning speed can increase significantly the measurement time.

2.3.2 Broadband sources

Light sources with broadband emission characteristics can be advantageous to perform absorption spectroscopy experiments as they allow, at least in principle, to detect multiple species. Commonly employed broadband light sources include black-body radiators or thermal sources and Light emitting diodes (LEDs). A black-body source is an idealized physical body that absorbs and emits electromagnetic radiation at all frequencies (and for all angles) [56] according to Planck's law:

$$\mathrm{B}(\lambda, \mathrm{T}) = \frac{2\mathrm{hc}}{\lambda^3} \cdot \frac{1}{\mathrm{e}^{\frac{\mathrm{hc}}{\lambda \mathrm{kT}}} - 1}, \tag{2.6}$$

where $\mathrm{B}(\lambda, \mathrm{T})$ represents the spectral radiance density (power per unit of solid angle and per unit of area) at thermal equilibrium for temperature T, h is the Planck constant and k the Boltzmann constant. The central emission wavelength of the electromagnetic radiation depends on the temperature and is typically located in the near and mid-infrared wavelengths for practical temperature that can be applied (see e.g. Globar source in Fig. 2.1). Black-body sources are temporally and spatially incoherent. Gas-discharge lamps are also broadband, generated by sending an electric discharge through an ionized noble gas (argon, neon, krypton, and xenon or a mixture of them) [57,58]. Their emission wavelength is mostly confined to the ultraviolet-visible range and similarly to black-body sources they are incoherent. This means that only a tiny fraction of the total emitted power can be used in practice and their collimation into a non-diverging beam is difficult, which results in limited sensitivity and resolution when used for absorption spectroscopy experiments.

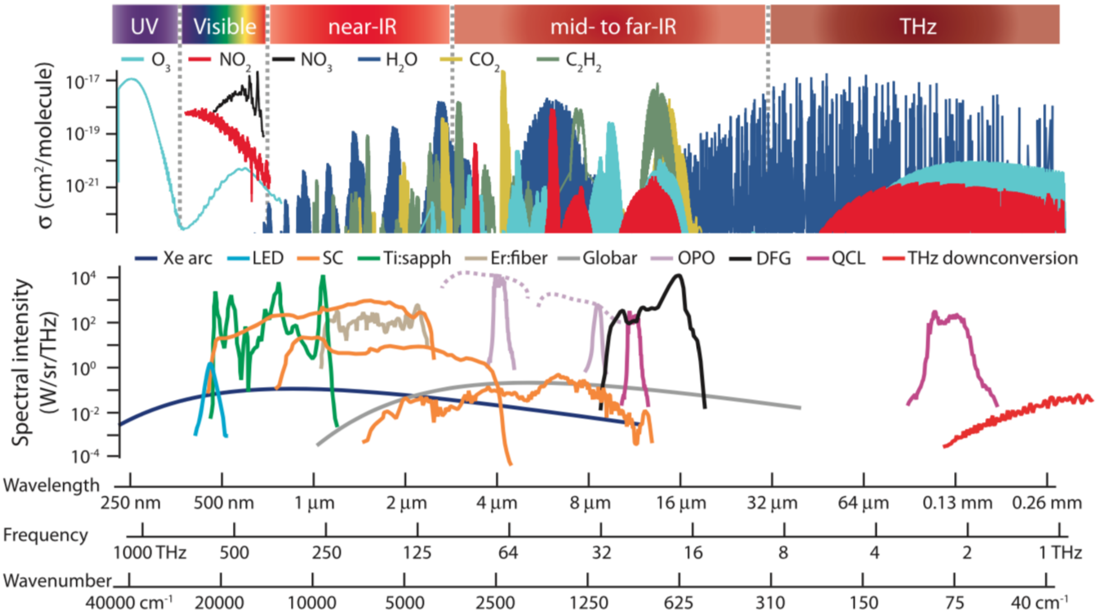

Figure 2.1 Absorption cross-section of common gas molecules (top) in relation to the spectral intensity of available light sources (bottom). Figure reproduced from [59].

LEDs are compact and cost-effective broadband light sources emitting in the visible with low power consumption, which makes them highly attractive as light source for lighting [60]. They have a relatively high brightness, however, their bandwidth is significantly reduced when compared to black-body or gas-discharge lamps. Superluminescent LEDs (SLEDs), on the other hand, exhibit even higher brightness with (limited) broadband emission in the near-infrared and are thus more adapted for broadband spectroscopy [39] as their spectrum is broader than that of a continuous wave laser and they are much brighter than a thermal source. Fiber-coupled superluminescent LEDs are available resulting in improved spatial coherence which facilitates collimation [61].

2.3.3 Optical parametric oscillators and amplifiers

Optical parametric oscillators (OPOs) and optical parametric amplifiers (OPAs) [62, 63] combine the advantage of a monochromatic laser (i.e. high brightness, narrow linewidth and high spatial coherence) with a broad wavelength operation range that can not be reached by direct laser emission. OPAs and OPOs rely on nonlinear frequency conversion in a crystal using difference-frequency generation process [64]. Specifically, when a strong pump beam co-propagates with a weaker signal beam at a different frequency in a nonlinear crystal, an idler beam is generated with a frequency equal to the frequency difference between the pump and signal beams. The signal does not need to be injected as a separate beam and may be generated from initial spontaneous parametric down-conversion (or sum-frequency generation). The process allows to reach wavelengths in spectral regions where direct laser emission is not available, including the ultraviolet or the mid-infrared. One significant advantage of OPA/OPO systems is that they are inherently tunable over extended wavelengths ranges, yet to be efficient the process requires very large pump intensities as well phase-matching between the pump and signal. Depending on the targeted spectral coverage, different types of nonlinear crystals are used where phase-matching can be achieved (via temperature or angle tuning) [65–69]. The main drawback of OPOs and OPAs is that they are expensive and bulky systems (pump, cooling system, complex optical cavities), making their use outside laboratories unpractical. OPOs/OPAs can also operate in pulsed mode where they emit radiation over a much broader bandwidth than in continuous-wave mode. This can allow removing the need for wavelength scanning in spectroscopy applications.

2.3.4 Frequency combs

A frequency comb is a coherent (i.e. phase-stable) broadband laser source whose spectrum consists of a serie of discrete and equally spaced lines [70]. There is a wide range of methods to generate frequency combs, including external modulation (amplitude and/or phase) of quasi-monochromatic lasers, nonlinear frequency mixing in nonlinear crystals or nonlinear waveguides (fibers, micro-resonators etc...) or intra-cavity mode-locking [71–74]. All these methods produce a steady train of short pulses in the time domain and, correspondingly in the frequency domain, a spectrum with equally spaced lines inversely proportional to the pulse train temporal periodicity. Originally developed to be used as frequency counters in optical frequency metrology [75], frequency combs are now widely employed in spectroscopic applications [19, 76, 77]. As a matter of fact, their characteristics in terms of accuracy, spectral purity, and broad spectral coverage make them an ideal tool for probing the spectral signatures of various materials and media. And indeed, multiple frequency-comb based techniques have been developed including, direct comb absorption spectroscopy where the large number of frequency comb lines provide a massive set of parallel detection channels, dual-comb spectroscopy that converts optical frequencies to radio frequencies allowing for amplitude and phase changes caused by absorption to be detected, or cavity-enhanced comb spectroscopy in which every comb line is coupled into a high finesse cavity mode allowing for ultra-sensitive detection with multiple parallel spectral channels [77,78]. However, frequency combs are currently not available in all spectral regions, in particular in the mid-infrared range, and their bandwidth or brightness may be limited.

2.3.5 Supercontinuum sources

Supercontinuum (SC) generation refers to the massive spectral broadening experienced by an optical field with narrow bandwidth during propagation into a nonlinear medium [79, 80]. SC generation was first observed in the 1970s when intense and short optical pulses where focused into a bulk piece of glass [81,82]. The term supercontinuum first appeared in the literature in 1980 [83] to emphasize the fact that a large and continuous range of frequency is generated during the nonlinear propagation. SC generation is mostly observed in materials with a third-order nonlinear susceptibility where most of nonlinear dynamics arise from the optical Kerr-effect associated with the intensity-dependence of the material refractive index in which an intense optical field propagates. The physics of SC generation is generally complex and depends on multiple parameters including the characteristics of the injected optical field (power, temporal profile, wavelength) and that of the nonlinear medium (dispersion and nonlinearity). Because of obvious advantages such as low-footprint and portability, broadband SC generated in an optical fiber or waveguide are highly attractive from an application viewpoint and in what follows we therefore restrict the discussion to fiber-based supercontinuum light sources.

The potential of optical fibers for SC generation has been rapidly realized, allowing to maintain high intensities over much longer propagation distances and therefore enhanced nonlinear interactions as compared to bulk geometries where diffraction can be a severe limitation. Yet, although the first observation of SC generation in the near infrared using an optical fiber dates back from the mid 1970's [84], it was nott until the very end of the 1990's that it became the subject of intense research and development. And it is only very recently that applications taking advantages of the unique properties of such light sources have started emerging. In this context, the end of the 1990's represent a significant milestone in the development of SC sources. This is due to the combination of two factors: on one hand the development of ultrafast Ti:Sapphire laser sources capable of producing pulses of light with femtosecond duration [85,86] and, on the other hand, the emergence of a new class of optical fibers known as of photonic crystal fibers with widely tailorable dispersion and nonlinear characteristics [87]. And indeed by launching low energy 100 fs pump pulses from a Ti:Sapphire laser into a single-mode photonic crystal fiber, Ranka et al. observed for the first time the generation of a true white light supercontinuum extending over more than one frequency octave from the UV to the near-IR [88]. Besides the remarkably large spectral bandwidth, what makes fiber-based supercontinuum sources so attractive from an application perspective is that their spatial extent can be confined to a single mode such that the SC generation process preserves perfectly the high spatial coherence properties of the incident laser beam. A practical consequence is that SC beams can be collimated over long distances which is a significant advantage over gas lamps or black body light sources. This also means that the brightness of SC sources is very high. A fiber-based supercontinuum thus combines the brightness and focusing properties of a laser beam with the spectral bandwidth of thermal emitters, yielding a unique source of light [89].

	Short pulse duration	Long pulse duration
Anomalous dispersion	Soliton Dispersive waves	Modulation instability Solitons dynamics
Normal dispersion	Self-phase modulation Four-wave mixing	Raman scattering Four-wave mixing

Table 2.1 Summary of nonlinear SC generation dynamics depending on the duration of the pump pulse and dispersion regime.

Detailed understanding of the physics of SC generation in optical fibers has rapidly opened up new perspectives in e.g. frequency metrology, optical imaging or remote sensing, with the possibility of tailoring the SC source properties to the targeted application. The ultra-broad bandwidth of SC sources is naturally central to any given application but the spectral and temporal coherence properties are also of high significance, as we shall see in the following chapters. The spectral and temporal characteristics of a fiber-based SC depend dramatically on the properties of the pump pulses (duration, peak power, polarization) and the parameters of the fiber (dispersion, nonlinearity) [66,90–92]. In the following we briefly introduce the different nonlinear mechanisms that underpin SC generation in optical fibers. The nonlinear dynamics that lead to the generation of a broadband SC can be coarsely divided into four distinct regimes depending on the duration of the pump pulses injected into the optical fiber and their wavelengths relative to the zero-dispersion wavelength of the fiber, as summarized in Table 2.1. The dynamics in the normal dispersion regimes are dominated by self-phase modulation (SPM) and four-wave mixing (FWM) for pulses with initial duration up to few picoseconds. These lead to SC spectra with a relatively symmetrical spectrum [80,90]. For longer durations, the SC generation process is essentially triggered by cascaded stimulated Raman scattering leading to a strong spectral asymmetry towards the long wavelengths [93,94].

In the anomalous dispersion regime on the other hand, SC generation arises from soliton dynamics. For pulses of duration below few hundred of femtosecond, the dynamics are self-seeded and initiated by higher-order soliton compression and subsequent fission into multiple fundamental solitons [90]. If the wavelength of the pump pulses is not too far detuned from the zero-dispersion of the fiber, the spectrum of the solitons extends into the normal dispersion regime which triggers the nonlinear emission of resonant dispersive waves on the short wavelengths side. The solitons also experience a frequency downshift due to (self-seeded) simulated Raman scattering, which extends the SC spectrum towards the long wavelengths side. For longer pump pulses, the initial spectral broadening arises from noise amplification via modulation instability, resulting in the formation of a train of solitons with random characteristics (duration and amplitude) [95]. These solitons subsequently undergo similar dynamics as in the case of short pump pulses. A particular feature associated with the long pump pulse regime is that the nonlinear dynamics are initially seeded by the noise present on the pump pulses. And this, irrespective of the dispersion regime. This leads to temporally (or spectrally) incoherent SC with significant temporal and spectral intensity fluctuations between consecutive SC pulses at the fiber output, a characteristics which is central to all the work described in the following chapters. Note that, in the short pump pulse regime, on the other hand, the supercontinuum can be highly stable with a constant complex amplitude from pulse to pulse, resulting in a perfect frequency comb.

2.4 Conclusion

There is a wide range of available methods to perform optical spectroscopic measurements and they all have advantages and drawbacks. Depending on the key criteria (cost-effective, footprint, sensitivity, selectivity etc...), one or the other may be selected. For each of the techniques, there is typically a wide availability of light sources and the particular choice of light source will affect the detection performances. Among those, fiber-based supercontinuum sources are very promising candidates to deliver optimum performances, combining the high brightness and spatial coherence properties of lasers with the spectral bandwidth of thermal incoherent sources. It is these unique properties that have been exploited and advantageously used in this thesis, to either enhance the performances of some of the spectroscopic techniques introduced above, or to derive new approaches to spectroscopy and imaging. Specifically, in the next chapters we demonstrate how supercontinuum sources can be used to perform broadband cavity-enhanced absorption spectroscopy and broadband photoacoustic spectroscopy in the mid-infrared spectral region. We further exploit the large pulse-to-pulse fluctuations of spectrally incoherent SC sources generated from long pump pulses and recent developments in dispersive Fourier transform to demonstrate new indirect approaches to spectroscopy and imaging in the form of spectral domain ghost imaging.

3. CAVITY-ENHANCED ABSORPTION SPECTROSCOPY

In this chapter, we first introduce the general principle behind cavity-enhanced absorption spectroscopy (CEAS) and then present, for the first time, its application to the the mid-infrared detection of multiple gases using a tailored supercontinuum source. The results of this work are reported in Publication I.

3.1 Operation principle

CEAS uses a cavity to increase the effective optical interaction path [96–99], leading to increased absorption when a sample is placed in the cavity. The increased absorption in turn leads to enhanced sensitivity. Similarly to most spectroscopy techniques, advantages are often balanced by drawbacks. In the case of CEAS, because the cavity is generally formed by highly reflective mirrors to increase significantly the interaction length, the transmitted signal to be detected at the cavity output is correspondingly very weak. It is therefore essential to use a light source with high brightness and/or a highly sensitive detection system. Previous experiments have been implemented with various types of sources, mostly broadband in order to detect multiple species in the visible and near-infrared [98–100]. However, certain gas or molecules do not absorb strongly in these wavelengths range or not at all, and absorption spectroscopy in the mid-infrared where absorption lines can be much stronger may be beneficial [101–105]. The main difficulty however with the mid-infrared is to find spatially coherent bright sources of light which can remain collimated over long distances [106]. The purpose of the work reported in this chapter and whose results appear in Publication II is to tailor a mid-infrared fiber-based supercontinuum source to perform mid-infrared CEAS with high reflectivity mirrors and long effective interaction length.

3.2 Cavity-enhanced absorption spectroscopy with a broadband source

CEAS can be used with broadband sources allowing for detecting simultaneously multiple species. Similarly to the case of narrowband sources [31], the technique is relatively simple and robust consisting in sending a collimated light beam into a sealed optical cavity, generally formed by a tube and two highly reflective concave mirrors in both ends. Light trapped inside the cavity is reflected multiple times off the mirrors and interact over long effective distances with the sample which may be solid, liquid or gaseous. A confocal design is typically used for the cavity in order to increase the effective interaction distance, as this design preserves the beam size by refocusing the beam after each reflection [107]. Following the DOAS approach, the spectral intensity $I_D(\lambda)$ of the light measured at the cavity output with a high resolution spectrometer is then compared to the spectral intensity $I_D^{(0)}(\lambda)$ measured at the cavity output in the absence of sample in the cavity.

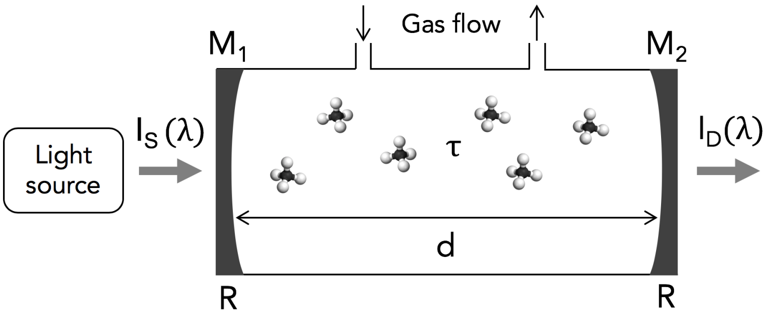

Figure 3.1 Schematic of CEAS method. $M_{1,2}$: mirrors, $I_S(\lambda)$: intensity of the light source injected into the cavity, $I_D(\lambda)$: intensity detected at the cavity output in the presence of gas molecules in the cavity, d: cavity length, R: reflectivity of the mirrors, τ: single-pass absorption of the gas. Adapted from [107].

The detected spectral intensity $I_D(\lambda)$ after the cavity can be modelled by considering the simple schematic shown in Fig. 3.1. The mirrors M_1 and M_2 are assumed to be identical and their transmission is taken to be $\rho = 1 - R$ where R is the (intensity) reflection coefficient of the mirror. For simplicity, we assume that the beam size is constant inside the cavity. The cavity length is d and the cavity is assumed to be filled with a gas of number density N and absorption cross-section σ. The spectral intensity at the cavity output after k round-trips inside the cavity can be readily calculated from the spectral intensity at the cavity output after $k-1$ round-trips as:

$$I_k(\lambda) = I_{k-1}(\lambda) R^2 (1-\tau)^2, \tag{3.1}$$

where $I_k(\lambda)$ and $I_{k-1}(\lambda)$ are the intensities at the cavity output after k and $k-1$ round-trips, respectively. Here, $\tau \simeq \alpha d$ represents the single-pass absorption induced by the presence of the gas in the cavity. After n round-trips, the intensity at the cavity output is thus given by:

$$I_n(\lambda) = I_s(\lambda)(1-R)^2R^{2n}(1-\tau)^{2n+1}, \tag{3.2}$$

where $I_s(\lambda)$ is the spectral intensity of the light source injected into the cavity. In the absence of absorbing gas in the cavity, $\tau = 0$ and denoting in this case $I_n^{(0)}(\lambda)$ the spectral intensity after n round-trips, we have:

$$I_n^{(0)}(\lambda) = I_s(\lambda)(1-R)^2R^{2n}. \tag{3.3}$$

The spectral intensity at the cavity output is integrated over multiple round-trips when measured with a photodetector with long integration time such that the detected intensities with and without a gas present in the cavity are:

$$I_D(\lambda) = \sum_{n=0}^{\infty} I_n(\lambda) \tag{3.4}$$

and

$$I_D^{(0)}(\lambda) = \sum_{n=0}^{\infty} I_n^{(0)}(\lambda). \tag{3.5}$$

The two equations above simply represent geometrical series such that the summation can be performed exactly to give:

$$I_D(\lambda) = I_s(\lambda)\frac{(1-R)^2(1-\tau)}{1-R^2(1-\tau)^2} \tag{3.6}$$

and

$$I_D^{(0)}(\lambda) = I_s(\lambda)\frac{(1-R)^2}{1-R^2}. \tag{3.7}$$

Substituting $R = 1-\rho$ and assuming that $\rho, \tau << 1$, the intensities at the cavity output can be rewritten, in the presence and absence of absorbing molecules, as (using a Taylor-series expansion to the first-order):

$$I_D(\lambda) = I_s(\lambda)\frac{\rho^2}{2(\rho+\tau)} \tag{3.8}$$

and

$$I_D^{(0)}(\lambda) = I_s(\lambda)\frac{\rho}{2}. \tag{3.9}$$

The optical density measured by differential optical absorption spectroscopy (DOAS) is therefore given by:

$$D(\lambda) = -\log\left(\frac{I_D^{(0)}(\lambda)}{I_D(\lambda)}\right) = -\log\left(\frac{\rho(\lambda)}{\rho(\lambda) + \tau(\lambda)}\right), \tag{3.10}$$

where log represents the natural logarithm to base 10, and we have now also included the possible wavelength-dependence of both the molecules absorption $\tau(\lambda)$ and mirrors transmission $\rho(\lambda)$.

The small single-pass absorption τ induced by the presence of the gas in the cavity is given by the linear approximation of the Beer-Lambert law and is directly proportional to the gas absorption cross-section $\sigma(\lambda)$ and number density N (and hence to the gas concentration):

$$\tau(\lambda) = 1 - e^{-\alpha(\lambda)d} = 1 - e^{-\sigma(\lambda)Nd} \simeq \sigma(\lambda)Nd. \tag{3.11}$$

In the case of multiple gas species simultaneously present in the cavity, Eq. (3.11) above can be modified to include the contribution of all gas species to the total absorption:

$$\tau(\lambda) = \sum_j \sigma(\lambda)_j N_j d, \tag{3.12}$$

where $\sigma(\lambda)_j$ and N_j are the cross-section and number density of gas species j.

Equations (3.10),(3.11) and (3.12) model the optical density of the gas when the DOAS approach is used to perform cavity enhanced spectroscopy. The enhancement provided by the cavity is apparent from Eq. (3.10) where the effective absorption is increased by a factor inversely proportional to the mirrors transmission or equivalently by the finesse of the cavity.

In a practical experiment one also needs to account for the spectral response of the spectrometer that measures the spectral intensity at the cavity output, as well as for potential smoothly varying absorbers, or drift in the input intensity due to fluctuations in the source [39]. These latter contributions may be modelled as a low-order (wavelength-dependent) polynomial correction [39]. The measured optical density in this case is then given by:

$$D(\lambda) = -\log\left(\frac{\rho(\lambda)}{\rho(\lambda)+\sum_j \sigma_j(\lambda)N_j d} * g(\lambda)\right) + \sum_k a_k\lambda^k, \tag{3.13}$$

where $g(\lambda)$ represents the spectrometer response function and a_k are the low-order polynomial coefficients accounting for smoothly varying absorbers and potential drift in the light source intensity. Note that the absorption cross-section $\sigma(\lambda)$ can be modelled precisely using the HITRAN2012 database [108] which accounts for multiple parameters such as gas concentration, temperature and pressure.

Previous demonstration of broadband incoherent CEAS have used black body, LEDs or SLEDs as a light source [98, 99, 107, 109]. Although the detection limit reached was at the part-per-trillion level, the brightness of these sources is still relatively low compared to fiber-based supercontinuum sources which are fully spatially coherent (if generated in single-mode fibers) and much brighter, allowing in principle for lower detection limits. Because of the lack of suitable broadband light sources in other wavelength regions and, in particular the mid-infrared, all of broadband CEAS applications have been restricted to the near-infrared. Furthermore, the fact that detectors are generally much less sensitive in the mid-infrared, the use of a high brightness light source is paramount for the application of broadband CEAS in this wavelength range. With intense research efforts into the development of supercontinuum sources in the past two decades, supercontinuum sources reaching the mid-infrared spectral region have started emerging [94, 110, 111] and appear as a strong candidate for broadband CEAS in the molecular fingerprint region. In what follows, we describe the development of a supercontinuum source extending up to 3.7 µm. The source is then employed to perform the first demonstration of multi-species broadband CEAS beyond 3 µm where methane and acetylene exhibit strong absorption lines.

3.3 Mid-infrared supercontinuum source

The main objective was to develop a compact, all-fiber supercontinuum (SC) source that reaches the mid-IR wavelengths using only off-the-shelf, cost-effective optical components. The SC source was constructed from a gain-switched fiber laser (pump laser) emitting 0.6 ns pulses at 1547 nm with tunable repetition rate from 50 kHz to 1 MHz. At a repetition rate of 100 kHz, the average power is 600 mW corresponding to a pulse peak power of around 10 kW. Spectral broadening of the pump pulses into a broadband continuum is achieved in two steps. Pulses from the pump laser are first injected into the anomalous dispersion regime of a 4 m-long dispersion-shifted fiber (DSF) made of silica, with a zero-dispersion-wavelength (ZDW) at around 1510 nm. Anomalous dispersion pumping near the ZDW has been indeed shown to be the most effective approach to broadband supercontinuum generation [90]. For long pump pulses the spectral broadening dynamics are initially seeded by the noise present on the pump pulses which, as a result of exponential amplification by modulation instability, breaks the initial sub-ns pulses into ultra-short solitons of sub-100 fs duration. Soliton dynamics including dispersive wave generation on the short wavelength side and Raman self-frequency shift towards the long wavelengths further extend the supercontinuum spectrum from c.a. 800 nm to 2400 nm which corresponds to the long wavelength edge of the silica transparency window. The SC spectrum at the DSF output is shown in Fig. 3.2.

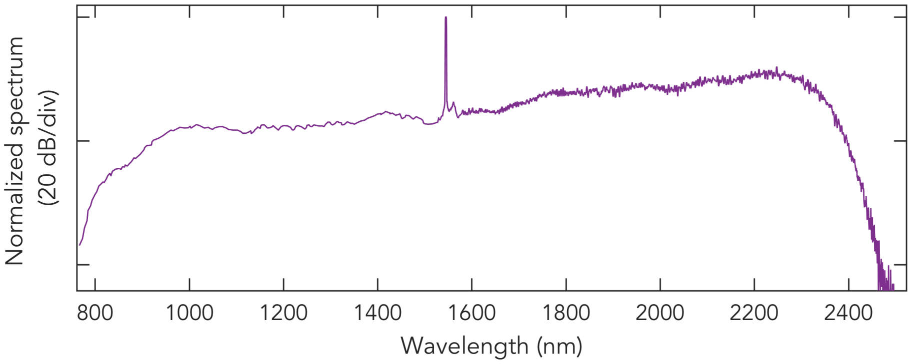

Figure 3.2 Spectrum of the SC at the output of the 4 m long DSF.

In order to extend the SC spectrum further and reach out to the mid-infrared range, the pulses are subsequently propagated in a 7 m-long fluoride [ZrF_4-BaF_2-LaF_3-AlF_3-NaF (ZBLAN)] fiber whose transparency window extends up to 4000 nm [112]. The ZDW of the ZBLAN fiber is at 1620 nm such that a significant part of the spectrum already lies in the anomalous regime, allowing for additional solitons dynamics and further extension towards the mid-infrared. The result is a SC spectrum stretching from 800 nm to 3750 nm as shown in Fig. 3.3. The spectrum was recorded using an optical spectrum analyzer (OSA) for the wavelengths shorter than 1700 nm and a monochromator calibrated with a black body heated at 700 K for the longer wavelengths. The average power at the output of the ZBLAN fiber was measured to be 160 mW. This represents a 27% conversion efficiency from the pump laser. Albeit rather small, the core diameter mismatch between the pump laser fiber output and the DSF on one hand, and the DSF and ZBLAN fibers on the other hand is mostly responsible for the loss of power in the SC generation process. Attenuation along the DSF and ZBLAN can also contribute.

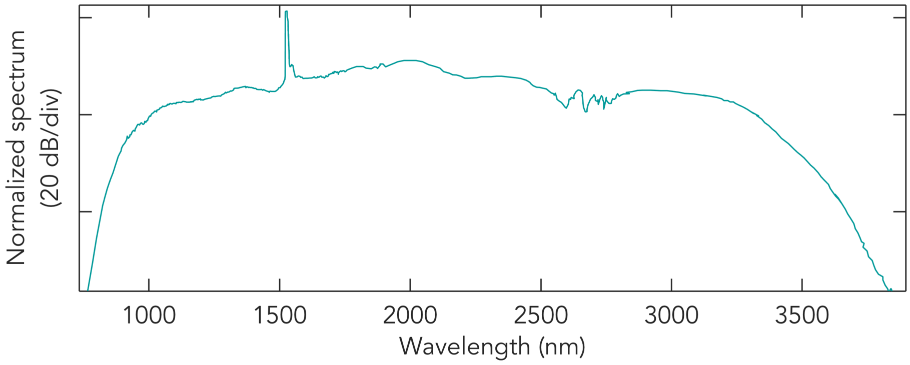

Figure 3.3 Spectrum of the SC at the output of the DSF and ZBLAN fibers combination.

The output of the SC is collimated into a 5 mm beam with an aspheric lens of 4 mm focal length with anti-reflection coating for wavelengths from 3 to 5 µm. The beam is spectrally filtered with two long-pass filters with cut-on wavelengths of 2337 and 2989 nm, respectively to select the part of the spectrum beyond 3 µm that will be used for the demonstration of broadband CEAS in the mid-infrared. This spectral filtering step is implemented due to possible interference between the first and second diffraction order of the grating in the monochromator which may occur for wavelengths above 1500 nm, leading to distortion in the measured spectral intensity at the cavity output. After spectral filtering the average power is around 5 mW.

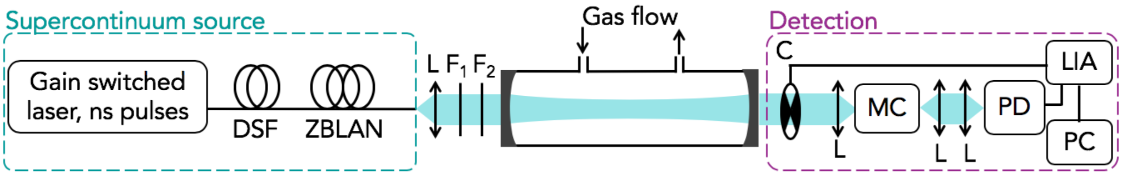

Figure 3.4 Experimental setup. L: lens, $F_{1/2}$: spectral filters, C: chopper, MC: monochromator, PD: photodiode, LIA: lock-in amplifier, PC: computer. Adapted from Publication I.

The spectrally filtered beam is directed to a confocal cavity as shown in Fig. 3.4. The custom-made cavity was built from an aluminum tube sealed by two highly reflective mirrors with a manufacturer-specified reflectivity over 99.7% for wavelengths between 3000 and 3450 nm. Two nozzles were added in both ends (on top) of the cavity allowing for gases to circulate inside the cavity where the flow is controlled with mass flow controllers. Because of the high finesse of the cavity, the intensity of the light beam drops from 5 mW to less than 10 µW at the cavity output corresponding to a power spectral density of 20 nW/nm over the 3000-3450 nm wavelength range. This makes the spectral detection challenging due to poor sensitivity of common detectors in this region.

3.4 Detection & Calibration of the system

The beam from the cavity output is focused to the entrance slit of the monochromator using a MgF_2 lens of 50 mm focal length. Inside the monochromator, the different spectral components are spatially dispersed with a 300 grooves/mm grating to the exit slit that selects a specific wavelength whose intensity is measured with a liquid nitrogen-cooled InAs photodetector. The grating is rotated to scan through all wavelengths to retrieve the spectrum of the light transmitted through the cavity. The spectral resolution of the measurement is determined by the number of grooves in the grating and the size of the slits. In the experiments reported below, spectra were measured with a resolution of 1 nm.

In order to increase the sensitivity of the detection, we use additional lock-in detection after the monochromator. Lock-in detection uses heterodyne mixing of its input with an external (modulating) reference to offset the signal frequency [113]. Subsequent electrical low-pass filtering allows for selective determination of the amplitude (and phase) of the signal in the narrow frequency band around the offset frequency set by the reference oscillator. Other frequencies where noise is mostly present are rejected, which increases significantly the signal-to-noise ratio of the detection system. The input signal to the lock-in amplifier is that from the photodetector at the monochromator output and the external oscillator is a mechanical chopper placed before the monochromator that modulates the SC light at a frequency of 245 Hz. The signal to the lock-in amplifier is integrated over 1 s and collected with a computer through a data acquisition card. The computer also controls and records simultaneously the grating position in the monochromator. Both data collection and monochromator wavelength scan are integrated in the same (LabVIEW) program that then produces the spectrum measured at the cavity output with the lock-in/monochromator combination. Note, that the 1 s-delay resulting from the lock-in integration time is accounted for by the program to ensure that the grating position stays still during the measurement by the lock-in amplifier.

In order to retrieve the concentration of gas(es) flowing through the cavity, we use the DOAS approach described above in Section 3.2. However, because the spectral-dependence of the experimental setup is not precisely known (e.g. the mirrors reflectivity or the lenses transmission may slightly vary from that provided by the manufacturers) or the monochromator instrument response may vary from the 1 nm nominal resolution, the spectral measurements are calibrated so as to determine the values of the fitting parameters used in Eq. (3.13). The calibration step consists in performing DOAS measurements of a gas sample of known concentration and fit the measured optical density using a least-square method [114]. The theoretical gas absorption cross-section as taken from the HITRAN 2012 database, the spectral-dependence of the mirror reflectivity, the resolution function, and system drift polynomial are used as fitting parameters. Once the spectral response of the system has been calibrated and the fitting parameters determined, unknown gas concentration can be determined with sub-part-per-million accuracy as shown in the next section.

3.5 Results and limitations

The measurements reported were achieved with the experimental setup described above. In principle, the reference spectrum $\mathrm{I}_\mathrm{D}^{(0)}(\lambda)$ should correspond to the spectrum measured at the output of the cavity in the complete absence of gas. However, vacuum is not easily achieved in the cavity and the seals can not withstand the very high pressure required to reach full vacuum. Instead, the reference measurement is taken from pure nitrogen (N_2) flowing in the cavity and which does not exhibit any absorption features in the spectral range of interest. This also removes all potential trace of residual water in the cavity (and naturally present in air). The cavity is then filled with a specific gas and the spectrum $\mathrm{I}_\mathrm{D}(\lambda)$ at the cavity output is measured again. The optical density is then calculated from the ratio of the reference to the gas measurement $-\log[\mathrm{I}_\mathrm{D}^{(0)}(\lambda)/\mathrm{I}_\mathrm{D}(\lambda)]$ and it is fitted with the same least square method used to determine the value of the apparatus parameters with now the concentration as the only free-running parameter.

Two different gases (acetylene and methane) were selected with strong absorption lines in the 3000-3450 nm wavelength region. The gases were diluted with pure nitrogen using mass-flow controllers in order to control their concentrations. Figure 3.5 shows the result of the fit for (a) acetylene with 5 ppm concentration and (b) methane with a 4 ppm concentration. The blue lines correspond the measured

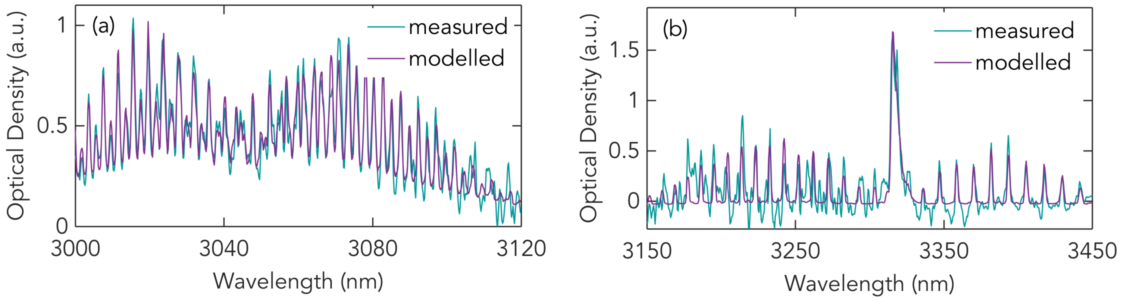

Figure 3.5 Optical density of (a) acetylene with 5 ppm concentration and (b) methane with 4 ppm concentration. The blue line corresponds to experimental measurements and the purple line to a least-square fit model using Eq. (3.13). Adapted from Publication I.

optical density while the purple lines are the result of the least-square fit using the theoretical acetylene and methane cross-sections from the HITRAN 2012 database. The negative value of the optical density is due to the detection noise. The least-square fit of Eq. (3.13) is in very good qualitative agreement with the experimental optical density in both cases. Note that a significant advantage of the broadband method here is that the fit is performed over a large wavelength range and thus a large number of distinct absorption lines, which decreases the error in the retrieved concentration even in the case of a relatively low signal-to-noise ratio.

The calibrated values of the mirrors losses and measurement resolution were then used to determine the sensitivity of the method by repeating the measurement for decreasing nominal gas concentrations but using the gas concentration as the only free-running parameter in the fit. The method sensitivity may then be determined by comparing the concentration retrieved from the fit with the nominal concentration. The results are shown in Fig. 3.6 both for acetylene with nominal concentrations varied from 0.5 to 10 ppm [Fig. 3.6(a)] and for methane [Fig. 3.6(b)] with nominal concentrations from 0.25 to 8 ppm.

One can see how the correspondence is excellent between the nominal and retrieved concentrations (the one-to-one correspondence is marked as the blue line) down to values of 0.5 ppm [Fig. 3.6(a)] and 0.25 ppm [Fig. 3.6(b)] for acetylene and methane, respectively. These values represent the detection limit of the technique for the developed system.

In order to fully exploit the potential of broadband CEAS using a SC light source, we then moved on to demonstrate that one can perform measurements over an extremely large spectral bandwidth to detect multiple gas species simultaneously.

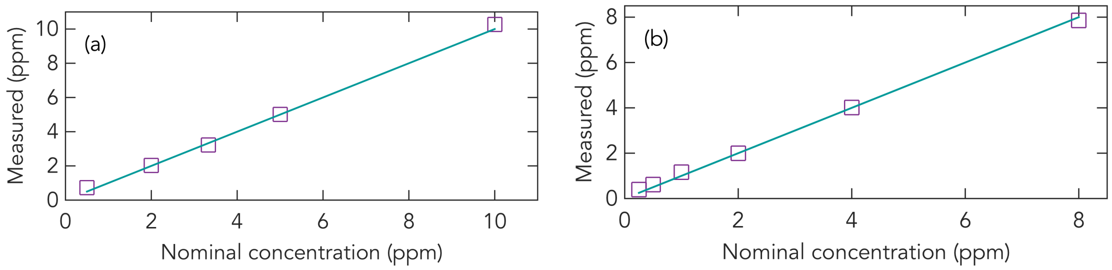

Figure 3.6 Comparison between nominal and retrieved concentrations for (a) acetylene and (b) methane. Adapted from Publication I.

Specifically, we exploited the full 450 nm wavelength range over which the mirrors exhibit high reflectivity and performed DOAS measurement of a mixture of acetylene and methane with 5 ppm and 2 ppm nominal concentrations, respectively. The experimentally measured optical density as well the result of the least square fit using the acetylene and methane concentrations as the free-running parameters are presented in Fig. 3.7 (plus a small-order polynomial to account for possible system drift during the relatively long total measurement time). The solid blue line represents the measured optical density while the solid purple line is the theoretical fit using Eq. (3.13) and the acetylene/methane cross-sections taken from HITRAN 2012 database. The retrieved concentrations from the least-square fit are 5.03 ppm and 1.98 ppm for the acetylene and methane, in excellent agreement with the nominal concentrations.

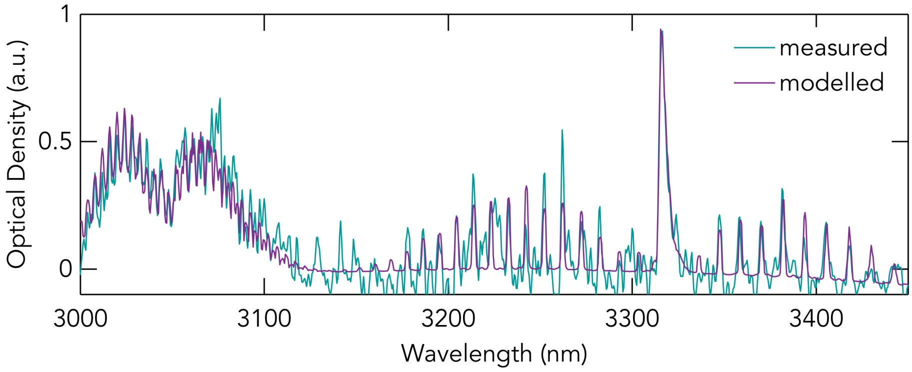

Figure 3.7 Simultaneous detection of 5 ppm of acetylene and 2 ppm of methane. The blue and purple lines correspond to the measured and modelled optical intensity respectively. Adapted from Publication I

3.6 Conclusions

Incoherent broadband CEAS has been demonstrated in the mid-IR range using a supercontinuum source and the retrieved concentration for a single gas or a mixture of two gases is in very good agreement with the nominal concentration of the sample flowing inside the cavity. The mid-IR range is an ideal window for gas measurements that do not generally exhibit strong absorption features in the visible or near-IR range. The use of a supercontinuum source here is a significant advantage due to its high brightness, wide bandwidth and perfect spatial coherence allowing to propagate over a long effective path in the cavity. While the achieved detection limits may not appear to be overly impressive as compared to those achieved using single-wavelength laser sources, one should bear in mind the rather remarkable 500 nm span of the detection. Current detection limits are better than what could be achieved with a conventional black body source in this wavelength range and we anticipate that much lower detection limits can be reached in the future if the SC power and/or detector sensitivity are increased.

4. BROADBAND PHOTOACOUSTIC SPECTROSCOPY

In this chapter, we first introduce the general principle behind photoacoustic spectroscopy (PAS) and in particular the link between absorption of radiation by a sample and the generation of an acoustic wave. We move on to describe how a Fourier transform infrared spectrometer that modulates the light source can be conveniently used to translate optical frequencies into acoustic frequencies. We then report an experimental comparison of photoacoustic gas measurements between a black body source and a supercontinuum source in the mid-infrared spectral region using a cantilever that optically reads out the signal from the acoustic cell. This work reported in Publication II represents the first demonstration of photoacoustic spectroscopy in the mid-infrared using a supercontinuum source.

4.1 Principle of photoacoustic spectroscopy

The concept behind PAS was initially discovered in 1880 by Alexander Graham Bell who observed that a beam of light modulated at an acoustic frequency and focused onto an absorbing sample could lead to the generation of a perfectly audible sound [115]. And the stronger the absorption in the sample, the louder was the emitted sound [116]. Such photoacoustic effect can be understood by considering the energy exchange occurring when light is absorbed by a given molecule placed in a sealed chamber. Specifically, the energy absorbed from the light source leads to increased molecule vibrations, which in turn increases its temperature. Assuming that the volume of the chamber where the molecules are placed is constant, an increase in the temperature leads correspondingly to an increase in the pressure. If the light is periodically modulated, the pressure in the chamber is then also periodically modulated creating acoustic waves that can be measured with a microphone, which converts the acoustic signal into an electrical signal [117]. The photoacoustic effect can be efficiently exploited to perform broadband sensitive absorption spectroscopy as mentioned in the introductory chapter of this thesis. The general principle is described in more details below.

Consider a quasi-monochromatic source of light at frequency ν_0 with intensity modulated in time at a frequency f_0:

$$I(t) = \frac{I_0(\nu_0)}{2}\left[1 + \cos(2\pi f_0 t)\right], \tag{4.1}$$

where $I_0(\nu_0)$ is the unmodulated light source intensity, and assume that the modulated intensity is sent through a chamber where molecules absorbing light at frequency ν_0 are present. The AC component of the acoustic signal $S(t)$ generated by the absorbing molecules and measured with a microphone at the output of the chamber is then proportional to:

$$S(t) = \frac{I_0(\nu_0)}{2}\left[1 - e^{-\alpha(\nu_0)d}\right]\cos(2\pi f_0 t), \tag{4.2}$$

where $\alpha(\nu_0)$ is the absorption coefficient of the molecules at frequency (ν_0) and d the length of the chamber. The Fourier transform $\tilde{S}(f)$ of the acoustic signal $S(t)$ is then directly proportional to the molecules absorption:

$$\tilde{S}(f) = \frac{I_0(\nu_0)}{2}\alpha(\nu_0)d\delta(f - f_0), \tag{4.3}$$

where δ is the Kronecker symbol and we have assumed that the absorption is small such that $1 - e^{-\alpha(\nu_0)d} \approx \alpha(\nu_0)d$. Note that in writing Eq. (4.3) we have only considered the positive frequency parts of the spectrum, the negative part being redundant. The Fourier spectrum of the recorded acoustic signal is a delta-function centered at the frequency f_0 with amplitude proportional to the absorption coefficient $\alpha(\nu_0)$. The advantage of the technique compared to other differential absorption spectroscopy technique becomes apparent. PAS is a background-free technique which does not require to measure the initial spectrum of the light source as the detected signal is directly proportional to the absorption and it is this feature inherent to the PAS technique that makes it particularly sensitive. The approach can be extended to the case of a broadband light source to probe simultaneously the molecules absorption over a wide frequency (or wavelength) range [118]. In this case, the different spectral components of the broadband light source are each modulated individually and the Fourier transform of the interferogram measured by the microphone (commonly referred to as the PAS signal) provides a direct measurement of the frequency-dependent absorption spectrum of the molecules [119]:

$$\tilde{S}(\nu) = \frac{I_0(\nu)}{2}\alpha(\nu)d. \tag{4.4}$$

4.1.1 Resonant vs. non-resonant detection

Photoacoustic cells can be operated in resonant or non-resonant mode. In the case of the non-resonant mode, the dimensions of the cell need to be smaller than the modulation period of the pressure wave, otherwise pressure waves inside the cell may form standing wave patterns which adds noise to the photoacoustic signal as the average pressure in the cavity oscillates with the modulation frequency of the cell [120]. In the case of resonant mode operation, light is modulated at the resonant frequency of the cell resulting in amplification of the acoustic signal by the quality factor of the cell [121]. Cells based on quartz tuning forks can reach quality factors over 10^4 and allow in principle for significantly enhanced sensitivity [122]. However, the cell design is usually complex, the background noise is also amplified by the resonant cell and the resonance frequency of the cell needs to be perfectly adjusted to the modulation frequency such as any drift of the resonance frequency can degrade or even suppress the resonant enhancement [123]. This also implies that one can not use a broadband light source with a resonant PAS cell as in this case the individual spectral components of the light source are modulated at different frequencies (see next sub-section) while the cell can only be resonant for a single frequency. In the work reported below, a non-resonant cell was used.

4.1.2 FT-IR spectrometer as a scanning interferometer

A Fourier transform infrared (FT-IR) spectrometer is a device that traditionally measures a broadband spectrum [116]. Unlike a conventional grating-based spectrometer that disperses spatially the spectral components and measures their intensity separately, FT-IR spectrometers collect all the spectral components simultaneously and can thus be seen as a multiplexed instrument. Most FT-IR spectrometers are based on Michelson interferometers as shown in Fig. 4.1. In a Michelson interferometer, light from the source is divided between two arms with a 50/50 beam splitter and reflected from each arm by highly reflective mirrors. The two light waves reflected from each arm are then recombined at the beam splitter where they

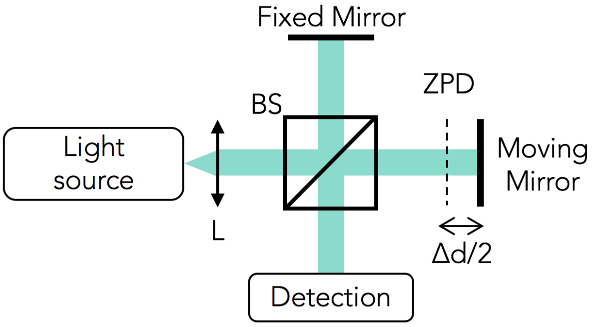

Figure 4.1 FT-IR spectrometer schematic. L: lens, BS: beam splitter, ZPD: zero-path difference, Δd: total optical path difference between the two arms of the Michelson interferometer.

interfere. The resulting interference pattern is detected with a detector positioned at the interferometer output. The interference pattern depends on the optical path difference Δd between the two arms, which can be conveniently used to measure the optical spectrum of the light source. Indeed, when the optical path difference between the two arms is null, all the spectral components are in-phase and a large signal is measured by the detector. As the optical path difference is increased, the different spectral components walk-off and are not in-phase anymore such that the signal at the detector follows complex oscillatory variations with decreasing amplitude. When the optical difference exceeds the coherence length of the source, the detected signal is essentially constant and independent of the path difference. The detected signal as a function of the optical path difference, thus produces an interferogram and this interferogram is directly linked to the spectrum of the light source by Fourier transform [116]. The spectral resolution $\delta\lambda$ of FT-IR spectrometers is inversely proportional to the maximum total optical path difference Δd_{max} that is scanned by the measurement:

$$\frac{\delta\lambda}{\lambda_0^2} = \frac{1}{\Delta d_{max}}, \tag{4.5}$$

where λ_0 is the central wavelength of the light source. Note that the resolution is reduced (i.e. gets worse) if the beam is not collimated and diverges [124]. The use of perfectly spatially coherent light sources is thus preferable.

Most FT-IR spectrometers operates as rapid-scan interferometers where one of the mirrors is continuously moved between two reference positions at a constant velocity v as shown in Fig. 4.2 [116]. Collimated monochromatic light propagating through the Fourier transform infrared spectrometer produces a perfectly sinusoidal

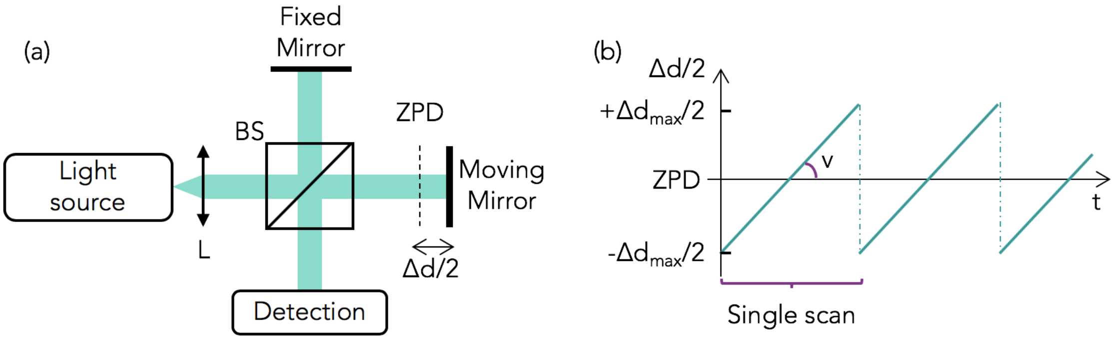

Figure 4.2 (a) Rapid-scan FT-IR spectrometer schematic. L: lens, BS: beam splitter, ZPD: zero-path difference. (b) Change in the path difference Δd as a function of time t. Δd_{max} represents the total range of the mirror total displacement and v represents the velocity of the moving mirror.

interferogram as a function time. The period of the interferogram corresponds to a difference in position of the mirror exactly equal to the wavelength of the incoming light. This relation can then be used to determine the wavelength of the light source:

$$\lambda_0 = 2vT_0, \tag{4.6}$$

where v is the speed of the scanning mirror and T_0 is the period of the recorded interferogram. Of course, this relation assumes that the scanning mirror velocity is constant at all times and known with a high degree of accuracy. Residual fluctuations in the velocity can be detrimental and results in distortion of the interferogram from a pure sine wave, causing spectral artifacts. In order to correct for any change in the velocity of the moving mirror, a reference is integrated with the Fourier transform infrared spectrometer, generally in form of a HeNe laser whose emitting wavelength λ_R is accurately known (λ_R = 632.8 nm). The reference beam travels in parallel through the interferometer with the light source whose spectrum is to be characterized, generating its own interferogram measured with a separate detector. The HeNe reference provides a very accurate calibration of the optical path difference and the unknown wavelength of a co-propagating quasi-monochromatic light can be measured from the relation:

$$\lambda_0 = \lambda_R \frac{T_0}{T_R}, \tag{4.7}$$

where T_R is the period of the interferogram corresponding to the reference wavelength λ_R. In the case of a broadband source, each spectral components produces its own sinusoidal interferogram whose period can be retrieved by Fourier transform of the signal measured at the detector and which then corresponds to the light source spectrum. The center wavelength of the Fourier transform is calibrated from the reference laser measurement using:

$$\lambda = \lambda_R \frac{T}{T_R}, \tag{4.8}$$

where the T is the period of the measured interferogram. In the case of PAS, the FT-IR spectrometer is not used directly for spectral measurements but rather to modulate each wavelength of the light source at a new specific (acoustic) frequency. Indeed, assuming that the scanning mirror moves at a constant velocity v, the light intensity at the FT-IR spectrometer output for a single wavelength varies as a function of time according to Eq. (4.1) as:

$$I(t) = \frac{I_0(\nu)}{2}\left[1 + \cos\left(\frac{2\pi\nu}{c}2vt\right)\right] \tag{4.9}$$

and the acoustic signal generated from absorption by a sample placed in the chamber or cell is given by:

$$S(T) = \frac{I_0(\nu)}{2}\alpha(\nu)d\cos(2\pi\nu T), \tag{4.10}$$

where $T = 2vt/c$ is a re-scaled time. When a broadband source is used, the corresponding acoustic signal $S_B(T)$ is obtained by integrating over all spectral components:

$$S_B(T) = \int_0^\infty \frac{I_0(\nu)}{2}\alpha(\nu)d\cos(2\pi\nu T)d\nu. \tag{4.11}$$

The Fourier transform of the acoustic signal therefore produces the absorption spectrum of the sample:

$$\tilde{S_B}(\nu) = \frac{I_0(\nu)}{2}\alpha(\nu)d. \tag{4.12}$$

4.1.3 Cantilever-enhanced photoacoustic spectroscopy

While microphones have been traditionally used to detect the acoustic signal resulting from light absorption by a sample, they typically have a limited dynamic range, exhibit a nonlinear response for large pressure waves, are temperature sensitive and can also suffer from damping or breathing effect of the membrane during wide movements [120, 125]. These limitations can reduce the overall sensitivity of the system. One possible alternative to improve the system sensitivity is to use the displacement of a cantilever to capture the generated pressure waves [125–129]. A cantilever is a thin beam generally made of silicon attached to a vertical surface at one end which allows large bending range of the unattached end [45]. When hit by a pressure wave, the cantilever is displaced like a flexible door and its displacement is directly proportional to the applied pressure and thus to the absorption in the sample. The changes in the cantilever position can be accurately measured using an interferometric readout system where the cantilever is utilized as the moving mirror [44]. A cantilever used as pressure sensor can be more than two order of magnitudes more sensitive compared to a membrane microphone [125]. Note that when using a cantilever to detect the acoustic signal, it must be placed in the chamber or cell along with the sample which can not flow, as otherwise it would induce some additional movement producing erroneous measurements.

4.2 Experimental setup

Broadband, supercontinuum-based cantilever-enhanced photoacoustic spectroscopy was demonstrated using the experimental setup presented in Fig. 4.3. The supercontinuum source is similar to that used in the demonstration of mid-IR cavity-enhanced spectroscopy reported in Chapter 3 except for a different repetition rate of the pump laser. The fact that we now use a different repetition rate changes the injected peak power into the DSF fiber and thus affects the generated SC spectral bandwidth. Specifically, two different repetition rates were used (400 kHz and 70 kHz) depending on the gas sample (water vapor or methane) whose absorption was measured so as to optimize the SC spectrum and spectral intensity with respect to the gas absorption band. For a repetition of 400 kHz, the SC spectrum spans from c.a. 1300 to around 2400 nm as shown in Fig. 4.4 while a repetition rate of 70 kHz leads to a SC spectrum extending from 900 nm up to 3700 nm. Note that in this latter case the SC spectrum is long-pass filtered above 2330 nm to remove the excess noise of the supercontinuum in the 1900 nm band occurring. For comparison the figure also shows the spectrum of the black body source that was used as a comparison reference for our measurements. We can see how the SC spectral density is much higher than that of the black body source. Combined with a high spatial coherence, this leads to improved photoacoustic detection sensitivity as discussed in the next section.

The SC is collimated into a 2 mm diameter beam with a reflective collimator and passed through a scanning FT-IR interferometer with a scanning speed $v/\Delta d$ of 1.6 kHz. Each wavelength of the light source is modulated by the interferometer according to Eq. (4.9). The SC light is then focused into a 10 cm non-resonant

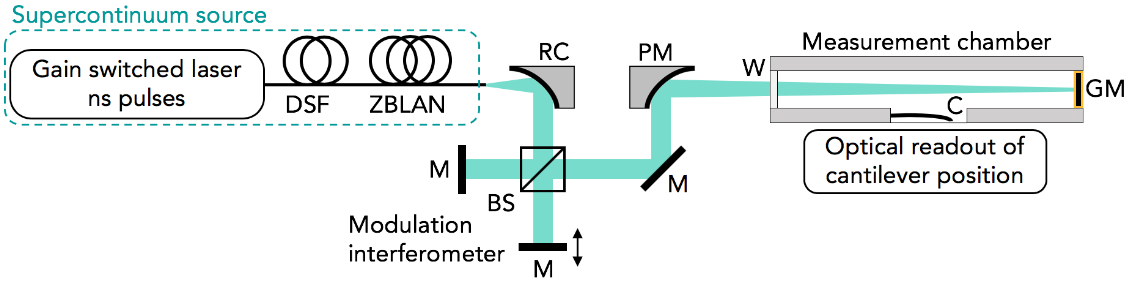

Figure 4.3 Experimental setup for broadband PAS. PM: parabolic mirror, M: mirror, BS: beam splitter, W: window, C: cantilever, GM: gold mirror. Adapted from Publication II.

cantilever-enhanced photoacoustic cell with a 76 mm focal length off-axis parabolic mirror. A gold mirror is placed at the opposite end of the cell to extend the interaction path by a factor of two. The temperature and pressure of the cell are set to 50°C and 1 bar, respectively. The cantilever is gold-coated of dimensions 6 mm x 1.5 mm x 10 µm and bends with the pressure changes in the sample and those movements are recorded with sub-pm accuracy by a laser based read-out interferometer. The cantilever sensor and the readout interferometer form an optical microphone that has demonstrated over hundred times better sensitivity compared to conventional microphone applied to photoacoustic gas detection [118]. The absorption features of the sample are retrieved by applying a Fourier transform to the recorded interferogram signal.

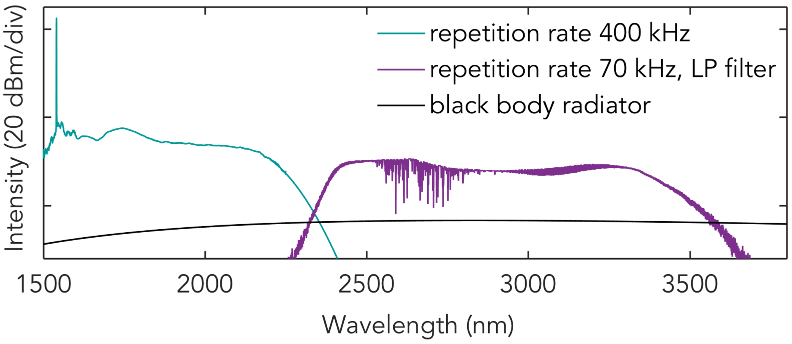

Figure 4.4 SC spectra used to perform PAS of water vapor (blue, 400 kHz repetition rate) and methane (purple, 70 kHz repetition rate, long-pass filtered). The spectrum of the black body source used for comparison is shown in black. Adapted from Publication II.

4.3 Results

The experimental setup described in the previous section was used to perform cantilever-enhanced photoacoustic detection in two different wavelength range: 1900 nm where water vapor has strong absorption lines and the 3000 nm ro-vibrational absorption band of methane which is also highly absorbing. Figure 4.5 plots the photoacoustic signal obtained from water vapor present in normal room air (20 °C and 30% humidity) corresponding to a concentration of around 7000 ppm in the PAS cell. The figure compares the absorption spectrum measured with the 400 kHz repetition rate supercontinuum source (solid blue line) with that obtained when using the black body source (solid black line). As is common in PAS measurements, both absorption spectra are the results of an average computed over 10 different FT-IR spectrometer scans in order to improve the signal-to-noise ratio (SNR). In order to decrease the measurement time of a single scan, the maximum optical path difference was set to 0.25 cm (from the 1 cm nominal possibility) resulting in a spectral resolution of 1.4 nm at 1900 nm. For completeness, the absorption spectrum modelled from the HITRAN 2012 database [108] is also shown in the figure (solid grey line).

Note that for convenient visualization, the photoacoustic signal from the black body source is magnified 10 times in the figure and in fact the photoacoustic signal obtained with the black body source is 70 times weaker than that obtained from the SC source. This significant increase in the photoacoustic signal arises from the much larger power spectral density of the SC as compared to the black body source, and which according to Eq. (4.4) leads to a corresponding large increase in the intensity of the detected photoacoustic signal. One can also see clearly that the measured absorption spectrum is in excellent agreement with the theoretical absorption spectrum predicted from the HITRAN database. The signal-to-noise is also significantly increased by a factor of 13 when using the SC source as compared to the black body source, representing more than an order of magnitude.

The absorption spectrum of the ro-vibrational band of methane in the mid-infrared measured with the 70 kHz supercontinuum source is shown in Fig. 4.6. The methane is sampled from a flow of premixed 400 ppm methane in nitrogen carrier gas. The solid purple line represents the photoacoustic signal obtained with the SC source, the black line shows the black body results and the gray line is the theoretical absorption spectrum from the HITRAN 2012 database. The resolution used to

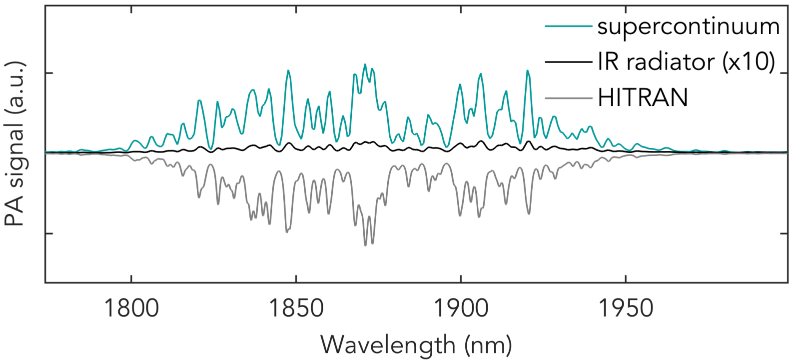

Figure 4.5 Comparison of the water vapor absorption lines measured at around 1900 nm with the 400 kHz SC source (blue) and black-body source (black). The theoretical absorption computed from the HITRAN 2012 database in also shown (gray). All the measurements presented were averaged over 10 scans in order to reduce the noise level. Adapted from Publication II.

perform both measurements was set to 4 nm for the methane and 1.4 nm for the water vapor. Again for convenient visualization, the photoacoustic signal measured from the black body source was magnified but by a factor of 5 in this case. There is a very good agreement between the theoretical lines modelled from the HITRAN 2012 database and the photoacoustic signal measured with the SC source. The black body also allows to retrieve the main absorption feature, however the weaker features from the side bands are not well resolved. The 19 times increase in the photoacoustic signal from the SC source as compared to the black body source is lower by a factor of four than for the water vapor measurements at 1900 nm and this is due to the fact that the power spectral density of the 70 kHz SC source at 3000 nm is about a factor of four lower than that of the 400 kHz SC source at 1900 nm. The noise due to the large shot-to-shot spectral intensity fluctuations of the SC (see also discussion in the light sources section of Chapter 2) is increased when the SC repetition rate is reduced from 400 kHz to 70 kHz as the number of SC pulses per FT-IR spectrometer scan is significantly reduced. The improvement in the signal-to-noise ratio as compared to the black body measurement (whose power spectral density and noise are, unlike that of the SC sources, similar at 1900 and 3000 nm) is then only a factor c.a. two.

4.3.1 Resolution of the system

The 1 cm maximum optical path difference in the FT-IR spectrometer determines the maximum resolution of the spectral measurements as given by Eq. (4.5). At a

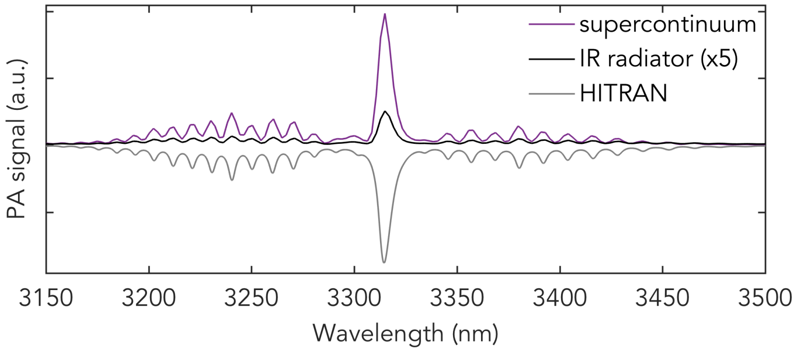

Figure 4.6 Comparison of the mid-infrared ro-vibrational methane absorption lines measured with the 400 kHz SC source (purple) and black-body source (black). The theoretical absorption computed from the HITRAN 2012 database in also shown (gray). All the measurements presented were averaged over 10 scans in order to reduce the noise level. Adapted from Publication II.

central wavelength of 3 µm, the corresponding maximum resolution is then 1 nm while for a 2 µm wavelength it is 0.5 nm. Figure 4.7 shows the impact of the resolution on the photoacoustic signal for methane. The blue line represents results obtained from a 1 nm resolution (i.e. using the full 1 cm moving range of the FT-IR spectrometer mirror) and the purple line shows results obtained for 4 nm resolution corresponding to a limited FT-IR spectrometer moving range of 0.25 cm. The absorption features are clearly broader and much weaker when using the 4 nm resolution, which can limit the sensitivity of the technique. It is therefore important to perform measurements at a suitable resolution (i.e. a resolution of the order of the linewidth of the absorption lines) in order to retrieve accurately the concentration of the gas. Of course, increasing the resolution of the measurements leads to an increase in the overall measurement time and it may be preferable in some cases to find a compromise between the resolution and measurement time. For example, in the measurements reported in this work, one scan takes 20 s at maximum resolution such that if multiple scans are used to improve the SNR as was done with the results presented in Figs. 4.5 and 4.6, the total measurement time can easily reach few minutes.

4.3.2 SNR - detection limit

As seen above, the measurement performances depend critically on the light source intensity. Indeed a higher intensity leads to larger pressure changes in the gas cell, thus wider movement range of the cantilever and a stronger photoacoustic

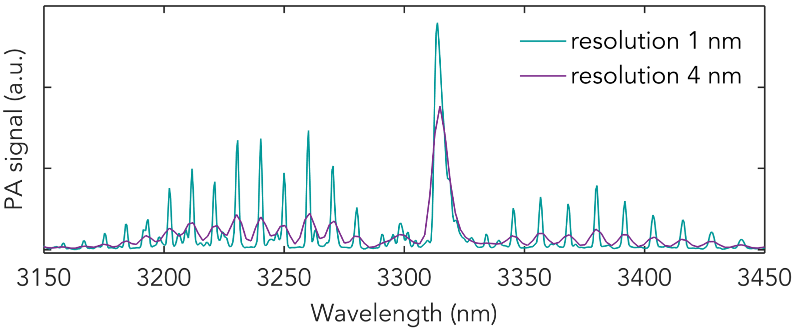

Figure 4.7 Impact of FT-IR spectrometer resolution on the measured absorption features. Adapted from Publication II.

signal. This is where the choice of a supercontinuum as the probing broadband light source is particularly beneficial, at least in principle. Fiber-based SC sources can be extremely bright and they are spatially coherent which allows to make full use of the theoretical resolution limit of the FT-IR spectrometer, unlike e.g. spatially incoherent black-body or thermal sources whose beam tends to diverge over long distances, which can reduce the effective FT-IR spectrometer resolution [116]. This is particularly significant at high resolutions when the using a FT-IR spectrometer with a moving mirror, whose travelling distance may be several tens of cm.

The detection limit can be estimated from the spectral region where light is not absorbed by the gas present in the cell. The SNR can be evaluated by dividing the highest photoacoustic signal intensity value recorded by the noise standard deviation (at 3σ). The detection limit can then be obtained by dividing the concentration by the SNR, such that the limit corresponds to the concentration that would yield a SNR of 1. The detection limit of the system for methane estimated using this approach is 2.6 ppm for the black body source and 1.4 ppm for the SC source. The limited improvement in terms of sensitivity when using the SC source is due to the increased intensity noise of the light source resulting from a lower repetition rate.

4.4 Conclusion

Supercontinuum sources are very promising candidates for broadband photoacoustic spectroscopy and indeed the work reported in this chapter demonstrates the potential of the approach by measuring the absorption spectrum of water vapor and methane in the near- and mid-infrared spectral regions. Because supercontinuum sources are bright and spatially coherent, they may allow for significant improvement in terms of sensitivity and resolution as compared to the use of a conventional black body radiation source. The current detection limit is determined by the spectral power density and intensity noise of the SC source. Improvements in the sensitivity can then be achieved by increasing the power spectral density of the supercontinuum source and limiting the noise influence. The former may be reached by employing a pump laser with larger peak power, while the latter can be realized using a high repetition rate SC source, which effectively averages out the noise contribution. Another possibility to reduce the intensity noise of the supercontinuum source is to use pump pulses of shorter duration [90]. The measurement time on the other hand is limited by the cantilever frequency response which requires the use of a low scanning speed FT-IR spectrometer. Yet, using a shot-to-shot stable SC source would allow for single scan measurements and improve significantly the measurement speed. The perfect spatial coherence of SC source further allows for using FT-IR spectrometers with a long scanning distance if higher spectral resolution is needed.

5. SPECTRAL GHOST IMAGING

In this chapter, we first introduce the general principle of ghost imaging and its conceptual application to the spatial domain. We then move on to transpose the concept of ghost imaging to the spectral domain and demonstrate two concrete applications to sensing and imaging in the form of broadband spectroscopy and optical coherence tomography, respectively. These results represent the first experimental demonstration of ghost imaging in the spectral domain and they are reported in Publications III and IV.

5.1 Principle of ghost imaging

Ghost imaging (GI) is an imaging technique originally associated with quantum optics and the generation of entangled photon pairs [130–133]. Specifically, photon pairs remain intrinsically "correlated" when split between two different paths, such that, by placing an object in the path of one of the photons, the other also "sees" the object although it does not physically interact with it. This allows to reconstruct an image of the object from the correlation calculated over multiple photon pairs, when the position of the detector in the object path is scanned. At first, ghost imaging was thought to be a technique inherently associated with the peculiar properties of entangled photons. However, it soon appeared that ghost imaging can also be perfectly realized using classical sources of light [51]. Because the work conducted in the framework of this thesis is fully associated with classical correlations, we focus our attention to the description of ghost imaging using classical light sources [134, 135].

Classical GI is based on measuring the intensity correlations between a reference path where probing intensity patterns are measured with a high degree of accuracy, and a test path where the object is placed and from which only the integrated intensity is measured [136, 137]. From an experimental point of view, light from a source producing random intensity fluctuations is divided between the reference and test arms. The fluctuations are measured with a high degree of accuracy in the reference arm while only a (slow) integrating detector measures the total light intensity from the test arm after interaction with the object. The signal from both arms are measured simultaneously and multiple measurements are correlated to retrieve the object. Significantly, neither beams carries meaningful information, but it is their correlation that produces a replica of the object. The intensity fluctuations may be completely random [136–138] or pre-programmed (so called computational version) [139, 140]. In the former case, the image reconstruction of the object typically requires thousands of distinct measurements to generate an image with a relatively high signal-to-noise ratio [134]. In the latter case, the number of distinct measurements can be minimized if the pre-programmed fluctuations form a complete basis in the mathematical sense, similarly to the strategies employed in compressive sensing [141]. Finally, although originally developed to image physical objects in the spatial domain, we point out that ghost imaging is a general technique that can be applied a priori to any other domain (time, spectrum, polarization etc...) provided the light source exhibits intensity fluctuations in this particular domain and the object to be characterized also modifies the fluctuations in this domain. And indeed, ghost imaging experiments have been recently reported in the time [142, 143] and polarization domains [144].

5.1.1 Spatial ghost imaging

In the spatial domain, one can use probing illumination patterns in the form of random binary masks generated by white and black pixels as shown in Fig. 5.1, random speckle patterns generated by a rotating diffuser [136, 145], or pre-programmed Hadamard masks using digital micro-mirrors [52, 138, 146, 147].

Figure 5.1 (a) and (b) Random binary patterns used for spatial GI. (c) Example of pre-programmed Hadamard pattern for GI.

In the case of random illuminating patterns, light is split between the reference and test arms with a beam splitter as shown in Fig. 5.2 that illustrates the typical layout of a ghost imaging experimental setup with random illumination. The random patterns are measured with high spatial resolution in the reference arm using e.g. a CCD camera. On the other hand, light in the test arm is directed through the object and the total transmitted (or reflected) signal is measured using a single-pixel detector with no spatial resolution. Both the spatially-resolved intensity profile from the reference arm and the integrated intensity from the test arm are recorded simultaneously. The process is repeated over a large number of different spatial intensity profiles (or patterns). The correlation between the probing patterns $\mathrm{I_{ref}(x)}$ with random fluctuations along the spatial coordinate x and the integrated signal after a target object $\mathrm{I_{test}}$ then produces a "ghost" replica of the object:

$$\mathrm{G(x) = corr(I_{test}, I_{ref}(x)) = \frac{\langle \Delta I_{ref}(x).\Delta I_{test}\rangle_N}{\sqrt{\langle [\Delta I_{ref}(x)]^2\rangle_N . \langle [\Delta I_{test}]^2\rangle_N}}}, \tag{5.1}$$

where corr is the correlation function, $\langle ... \rangle_\mathrm{N}$ represents averaging over N realizations,

$$\mathrm{\Delta I_{ref}(x) = I_{ref}(x) - \langle I_{ref}(x)\rangle_N} \tag{5.2}$$

and

$$\mathrm{\Delta I_{test} = I_{test} - \langle I_{test}\rangle_N}. \tag{5.3}$$

Extension to 2D is easily performed by replacing in the equations above the spatial coordinate x with a matrix of spatial coordinates (x, y).

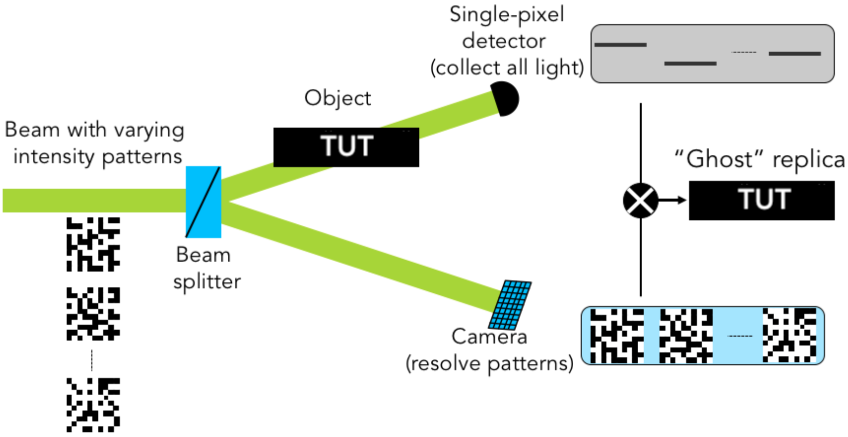

Figure 5.2 Schematic illustration of spatial ghost imaging.

An important requirement for ghost imaging with random illumination is that intensity fluctuations within each realization and from one realization to another are completely uncorrelated, allowing to "sweep" through all the patterns possibilities and preventing artifacts in the retrieved image. In the case when the illuminating patterns are pre-programmed, the need for a reference arm is removed and the number or independent measurements significantly reduced.

The spatial resolution of ghost imaging is given by the precision with which the random intensity patterns can be measured in the reference arm in the case of random illumination, or with which they can be pre-programmed in the case of a computational approach [139]. Furthermore, since the test arm only records an integrated intensity signal, any linear perturbation occurring after the object (e.g. wavefront distortions) will essentially have no effect on the reconstructed image as it is blind to the correlation calculation [145]. Of course, this only applies in the case the perturbations do not vary in the course of the measurements.

5.2 Ghost imaging in the spectral domain

In order to transpose ghost imaging to the spectral domain, one needs to swap the light source with random or pre-programmed spatial intensity fluctuations with a light source with spectral fluctuations. The spatial object on the other hand is replaced by an object with a wavelength or frequency-dependent transmission (or reflection). It is then the spectral transmission (or reflection) of the object that is effectively retrieved by the spectral ghost imaging scheme. This approach may be particularly useful to identify remotely e.g. the spectral signature of molecules or materials in spectral regions where no highly sensitive detector exist. If random spectral fluctuations are used as probing patterns, they need to be measured in real-time in a reference arm. This is the approach we report here. The resolution with which the spectral transmission (or reflection) of the target object is retrieved is determined by the resolution with which the random spectral fluctuations are measured in the reference arm.

5.2.1 Light source for ghost imaging in the spectral domain

Ghost imaging in the spectral domain requires a light source with random spectral fluctuations and these fluctuations should also vary over time such that one can perform multiple probing measurements to calculate the correlation image. An incoherent pulsed source is ideal for this purpose as the spectrum associated with a single pulse varies from pulse to pulse. Incoherent pulsed sources may be generated by taking advantage of noise-seeded nonlinear dynamics in optical fibers. For example, when a perfectly coherent pulse is injected into an optical fiber with sufficient power, the small noise fluctuations present on top of the input pulse (quantum noise, intensity noise, amplified spontaneous emission etc...) maybe be dramatically amplified by modulation instability [53, 148–150]. More specifically, if the duration of the initially coherent pulse is relatively long (typically few picoseconds), the spectral broadening caused by the fiber nonlinearity is seeded by the noise outside the input pulse spectral bandwidth. This is because the gain bandwidth of the modulation instability process exceeds the spectral bandwidth of the pulse. The random nature of the noise (amplitude and phase) then leads to random spectral fluctuations after propagation in the fiber. If the pulses are injected with sufficient peak power, the initial stage of modulation instability may be followed by solitons dynamics, resulting in the generation of a broadband incoherent supercontinuum with large shot-to-shot fluctuations as discussed in Chapter 2. It is this type of source that we use in our subsequent demonstration of ghost imaging in the spectral domain. A schematic illustration of the incoherent supercontinuum source is shown in 5.3.

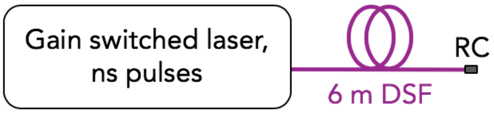

Figure 5.3 Schematic of the incoherent supercontinuum source, RC: reflective collimator.

The pump pulses to produce the incoherent SC are emitted by a gain-switched laser at 1547 nm with 0.5 ns duration and up to 4 kW peak power. The repetition rate of the pump laser is tunable but in these experiments it was set to around 120 kHz. The laser has an additional output port that can be used as an optical trigger for an oscilloscope. The pulses propagate into the anomalous dispersion regime of a 6 m long DSF with a ZDW at 1510 nm. The result is a broadband incoherent supercontinuum whose bandwidth can be tuned by changing the injected pulses peak power. Examples of single-shot spectra measured using the dispersive-Fourier transform technique (see next section) are plotted in Fig. 5.4 showing that there are indeed large variations between the spectrum of individual pulses.

The injected peak power affects the modulation instability gain bandwidth (the larger the peak power the larger the modulation instability gain bandwidth). This in turn affects the temporal duration of the emerging solitons and correspondingly

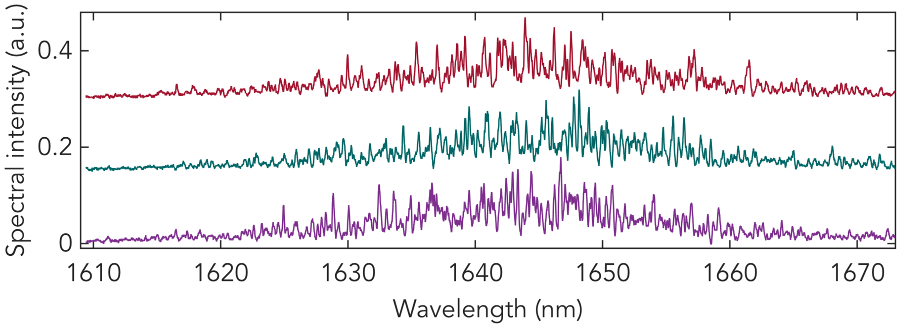

Figure 5.4 Examples of measured single-shot spectra of the supercontinuum. The spectra are plotted with an arbitrary vertical offset for better visualization

in the spectral domain the local bandwidth of the spectral fluctuations. As a rule of thumb, the bandwidth of the fluctuations decreases for larger injected peak powers. This will lead to better resolution for spectral ghost imaging, however if the power is too high the bandwidth of the fluctuations is too narrow and they can not be resolved in the reference arm measurements. In fact this situation can be detrimental as the real-time measurement will partially average out the spectral fluctuations over the resolution bandwidth of the measurement, which can lead to some partial spectral correlations inside each pulse. It is therefore important to optimize the injected peak power in order to have spectral fluctuations with a local bandwidth near the resolution of the reference arm measurement. This condition is met when we inject a peak power equal to c.a. 1 kW into the DSF, corresponding to an average power of 80 mW and a SC average spectrum extending from 1200 to over 1750 nm (limit of the OSA) as shown in Fig. 5.5.

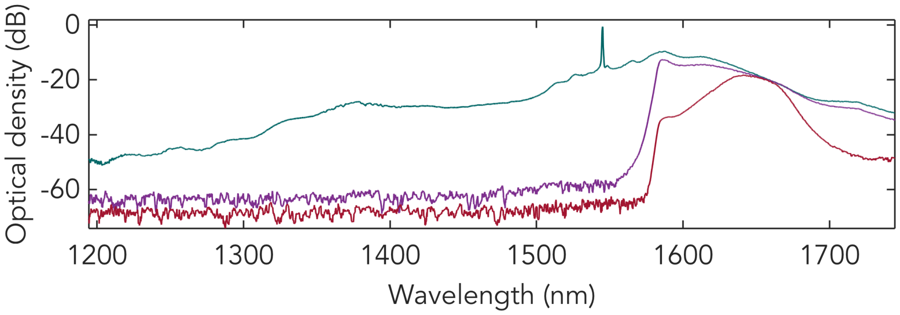

Figure 5.5 Average spectrum of the supercontinuum used for spectral-domain GI. Blue line: full spectrum. Purple line: after LPF and red line: after LPF and NBF.

The spectrum is filtered with a long-pass filter (LPF) and a narrow-band filter (NBF) to work in the low-attenuation range of the dispersion compensation module (DCM) used to perform the dispersive-Fourier transform.

5.2.2 Measuring spectral fluctuations in real-time

Real-time spectral fluctuations can be measured using the time-stretch or dispersive Fourier transform method [48]. The technique is the temporal analog of spatial diffraction. A schematic illustration of the technique is shown in Fig. 5.6.

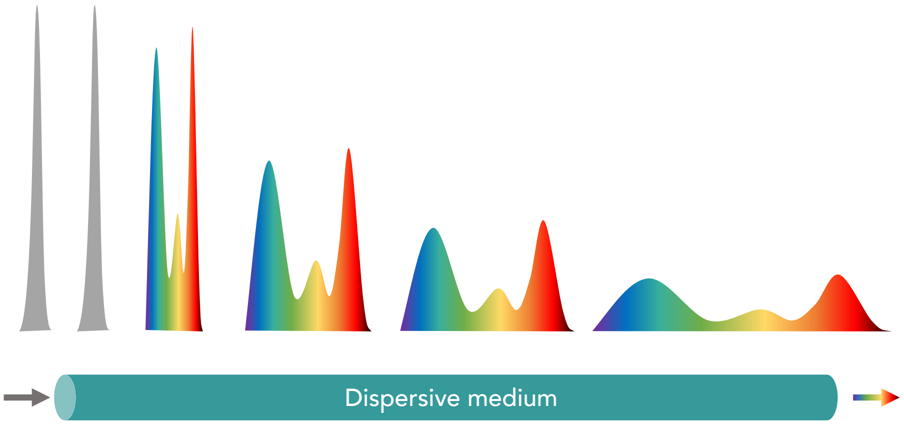

Figure 5.6 Schematic of dispersive-Fourier transform principle. Figure adapted from [48].

The different components of the single-shot spectrum associated with a given pulse can be separated in time when injected into a highly dispersive fiber. The temporal profile as measured by a fast photodiode and real-time oscilloscope at the dispersive fiber output is then a direct replica of the pulse spectrum. The spectral resolution of the technique $\delta\lambda$ [in nm] is determined by the total accumulated dispersion along the dispersive fiber and the bandwidth of the detection system:

$$\delta\lambda = \frac{1}{\mathrm{D} \times \mathrm{L} \times \mathrm{BW}}, \tag{5.4}$$

where D is the dispersion parameter of the fiber [in ps$\cdot$nm$^{-1}\cdot$m^{-1}], L is the fiber length [in m] and BW is the effective detection bandwidth of the photodiode + oscilloscope [in GHz]. A dispersion compensating module with total dispersion $\mathrm{D} \times \mathrm{L} = 3000$ ps$\cdot$nm^{-1} was used. Because the DCM only operates over the wavelength range 1600-1700 nm, a combination of long-pass and bandpass filters was used to select that part of the SC spectrum for which the spectral fluctuations can be measured in real-time. All the data from the oscilloscope are measured as a function of time and the time axis of the detection needs to be converted back to spectral domain. This conversion can be done easily if the total dispersion is accurately known. However, in our case the dispersion provided by the manufacturer is only approximate such that the wavelength axis calibration was performed by comparing the average spectrum of the SC as measured by the DFT with a direct measurement using an OSA.

The average spectrum after the LPF and NBF is shown in Fig. 5.5 and spans from c.a. 1610 to 1670 nm well within the operation range of the DCM. Examples of single shot spectra measured with the dispersive Fourier transform method are plotted in Fig. 5.4. One can see how the individual spectra associated with individual SC pulses are highly structured with large and seemingly random fluctuations.

The random nature of the fluctuations can be further quantified by evaluating the wavelength-to-wavelength and pulse-to-pulse intensity correlation maps (in the sense of linear Pearson correlations) and this is illustrated below in Fig. 5.7. The former gives information on intra-pulse spectral fluctuations correlations while the latter provides information on inter-pulses correlations. Note that for the pulse-to-pulse correlation map, the single-shot spectra are normalized to the average SC spectrum prior to the correlation calculation to truly isolate the correlations in the fluctuations superimposed on top of the spectral envelope of the filters combination. It is clear from the plots in Fig. 5.7, that there are essentially no inter- nor intra-pulse correlations in the SC light source and this is precisely what is needed to perform ghost imaging in the spectral domain with random fluctuations.

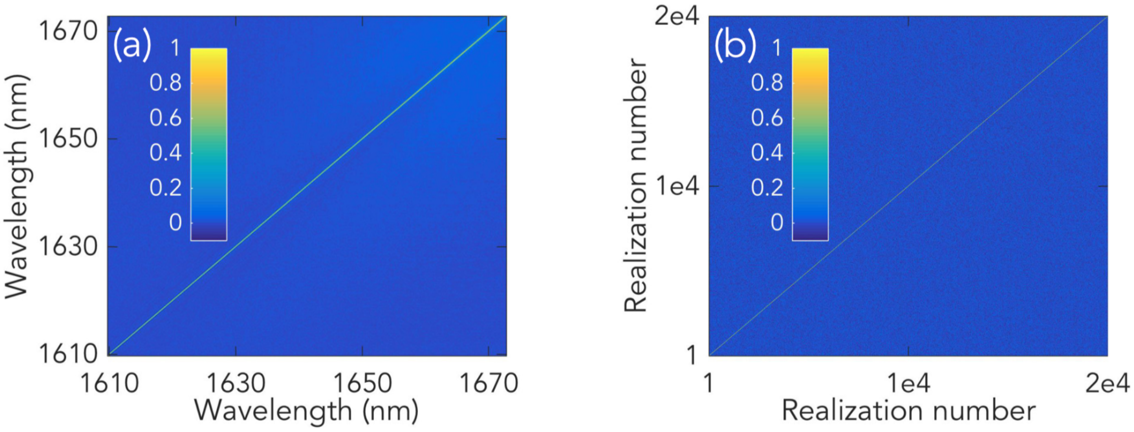

Figure 5.7 (a) Wavelength-to-wavelength correlation map of the SC. (b) Pulse-to-pulse correlation map of the SC. Reproduced from Publication III.

5.2.3 Experimental setup

The experimental setup for ghost imaging in the spectral domain is shown in Fig. 5.8. Light from the filtered supercontinuum is divided with a fiber beam splitter (BS) unequally (99% and 1%) between the reference and test arms. In the reference arm the shot-to-shot spectral fluctuations are measured in real-time using the DFT approach as described above. The 99/1 splitting ratio between the reference and test arms is specifically chosen to compensate for the $\approx$ 10 dB attenuation from the DCM in the reference arm. An object with a given wavelength-dependent transmission is placed in the test arm and the total (spectrally) integrated signal is measured with a slow detector after the object. Multiple synchronized measurements from the reference and test arms are recorded with the real-time oscilloscope using the output port of the SC pump laser as the trigger. The three signals (trigger, reference and test) are collected by the oscilloscope operating in fast frame (FF) mode with a resolution of 50 GS/s and a 20 GHz bandwidth. The resolution of the spectral fluctuations is limited by the 1.2 GHz detector used in the reference arm and it is estimated to be 0.3 nm from Eq. (5.4).

5.2.4 Measurement acquisitions

In FF mode, the oscilloscope captures the single-shot spectra and integrated signals from the reference and test arms, respectively, without the 8 μs dead time between consecutive SC pulses (corresponding to the 120 kHz of the SC repetition rate), which ensures efficient use of the record length memory. This is key here since a large number of independent measurements are required to evaluate the correlation image that will produce the ghost replica of the object spectral transmission. And indeed, the memory of the oscilloscope is the limiting factor for the maximum number of acquisitions that can be saved at once. As an example, if one uses a 200 ns recording time window (the duration of the single-shot SC spectra after temporal stretching in the DCM is $\Delta\tau = \mathrm{D} \times \mathrm{L} \times \Delta\lambda = 3000 \times 60 = 180$ ns; with $\Delta\lambda$ the SC bandwidth) with a 50 GS/s sampling rate, there are 10,000 sampling points in the measurement of a single-shot spectrum allowing for a maximum number of 2871 consecutive single-shot acquisitions after which the oscilloscope memory is full. Finally, it is important to bear in mind that the pulses propagating through the reference arm are delayed compared to the pulses from the test arm due to the long fiber length in the DCM (tens of km). The delay was measured to be 83 μs which corresponds to an effective shift of 10 acquisitions at a 120 kHz repetition rate (the repetition rate was in fact tuned to 120.52 kHz to corresponds exactly to a 10 acquisitions delay). This shift needs to be taken into account in the correlation calculation so as to correlate the corresponding reference and test arm signals.

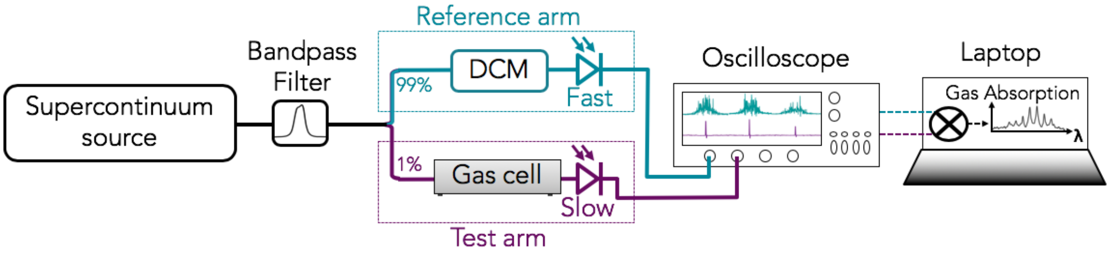

Figure 5.8 Experimental setup for spectral domain ghost imaging.

5.2.5 Data processing

The first step is to reshape the data recorded into two different matrices whose different lines correspond to the different single-shot spectra and to the spectrally-integrated signal after the object, respectively. The type of file format is also changed in order to reduce the size from 500 MB to 40 MB. A circular shift is subsequently applied to the matrix containing the measured probing spectral fluctuations in order to account for the long delay in arrival to the detector due to propagation in the DCM as compared to the spectrally integrated intensity measured from the test arm after the object. With a 120.52 kHz repetition rate, the delay directly translates into to 10 realizations and therefore a circular shift of 10 columns is applied to each column of the spectral fluctuations reference matrix. This also means that the last 10 measurements from the test arm have no correspondence and they are thus removed from the data sets.

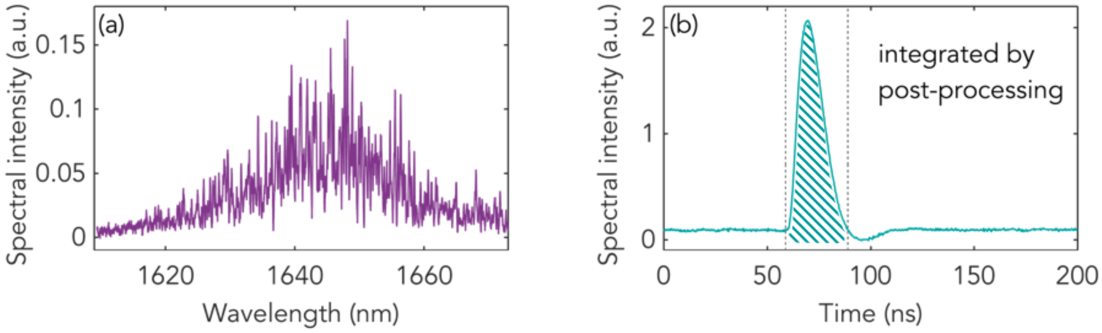

Figure 5.9 (a) Example of single-shot spectral intensity measured in the reference arm. (b) Corresponding integrated intensity recorded after the object in the test arm

Figure 5.9 shows a typical example of the integrated intensity signal measured after an object (right) and of the corresponding probing spectral fluctuations measured in the reference arm (left). One can see that, although the signal is spectrally integrated after the object, it still varies with time due to the detector finite response time (40 ns in this case) and the signal variation therefore simply corresponds to the integrated intensity after the object convolved with the impulse response of the detector (the duration of a SC pulse being two orders of magnitude shorter). We then numerically integrate this signal which produces a single value corresponding to the spectrally integrated transmission of the object. Note that, in order to reduce the noise, we only integrate over the impulse response of the detector and not the entire time window.

Differential ghost imaging for sparse objects

Ghost imaging of low contrast objects (e.g. objects which are mostly transparent) or sparse objects whose features dimensions are small compared to the beam area require a very large number of realizations to achieve sufficient SNR in the ghost replica [151]. This is because, in this case, changes in the integrated intensity recorded after the object are very small from one acquisition to another and it takes a large number of distinct measurements for the correlation to isolate the objects fine details from the transmitted background light. In order to significantly improve the SNR, an additional processing step referred to as differential ghost imaging [137] can be applied to the recorded test arm. The idea behind differential ghost imaging is to make the integrated correlation sensitive to small variations in the (integrated) intensity detected after the object in the test arm. This can be realized in practice by a simple post-processing step where the measured test arm intensity $\mathrm{I_{test}}$ is replaced by $\mathrm{I_{test}^{(DGI)}}$ defined as:

$$\mathrm{I_{test}^{(DGI)}} = \mathrm{I_{test}} - \frac{\langle \mathrm{I_{test}} \rangle_\mathrm{N}}{\langle \mathrm{I_{ref}^{(int)}} \rangle_\mathrm{N}} \mathrm{I_{ref}^{(int)}} \quad \text{with} \quad \mathrm{I_{ref}^{(int)}} = \int \mathrm{I_{ref}(X)dX}, \tag{5.5}$$

where $\mathrm{I_{ref}}$ is the intensity fluctuations measured in the reference arm, $\mathrm{I_{ref}^{(int)}}$ represent the integrated signal that would be measured by a slow detector placed *before* the object, and $\langle ... \rangle_\mathrm{N}$ represents the average over N realizations. Not that the variable X here represents the domain of the ghost imaging measurement. In the case of spectral-domain ghost imaging, X simply represents the wavelength variable λ. The ghost image G(λ) is obtained by calculating the correlation between $\mathrm{I_{ref}}(\lambda)$ and this newly defined test arm intensity $I_{test}^{(DGI)}$ as:

$$G(\lambda) = \mathrm{corr}(I_{test}^{(DGI)}, I_{ref}(\lambda)) = \frac{\langle \Delta I_{ref}(\lambda).\Delta I_{test}^{(DGI)} \rangle_N}{\sqrt{\langle [\Delta I_{ref}(\lambda)]^2 \rangle_N \cdot \langle [\Delta I_{test}^{(DGI)}]^2 \rangle_N}}, \tag{5.6}$$

where corr is the correlation function,

$$\Delta I_{ref}(\lambda) = I_{ref}(\lambda) - \langle I_{ref}(\lambda) \rangle_N \tag{5.7}$$

and

$$\Delta I_{test}^{(DGI)} = I_{test}^{(DGI)} - \langle I_{test}^{(DGI)} \rangle_N. \tag{5.8}$$

Distortion due to a non-uniform (wavelength-dependent) variance in the spectral fluctuations

If the variance of the probing random fluctuations is not uniform across the spectral measurement window, the ghost image will be distorted. The distortion maybe be eliminated by post-processing the ghost image with a low-pass filter in the Fourier space. Specifically, one can multiply the Fourier transform of the correlation function in Eq. (5.6) by a narrowband notch function centered over the zero-frequency. In this way, one can effectively suppress the distortion induced by the non-uniform variance across the spectral measurement window, which is typically slowly-varying and corresponds to the low frequency components of the Fourier transform while sharp object features correspond to high frequency components. Of course, one should be careful in applying such a post-processing step, as it may remove some of the object broad features.

5.2.6 Application of spectral-domain ghost imaging to broadband absorption spectroscopy

We now demonstrate the application of ghost imaging in the spectral domain to broadband absorption spectroscopy. The results are reported in Publication III.

The object inserted in the test arm is a fiber-based gas cell filled with methane CH_4. The 2v3 overtone absorption lines in the 1600 nm wavelength region play the role of the spectral object. An illustration of these lines as theoretically calculated from the HITRAN 2012 database is shown in Fig. 5.10. The objective is to retrieve a ghost image that corresponds to the absorption spectrum of these lines. We recorded multiple sequences of 2871 consecutive single-shot SC spectra over a time window of 200 ns and with a sampling rate of 50 GS/s. Note that the time window was intentionally slightly reduced as compared to the actual full time span of an individual SC spectrum than spans 250 ns, allowing to reduce the temporal window from 400 ns to 200 ns and thus increase by a factor of two the number of acquisitions recorded at once. Of course, it was carefully checked that the wavelength components that are effectively filtered lie outside the methane absorption spectrum.

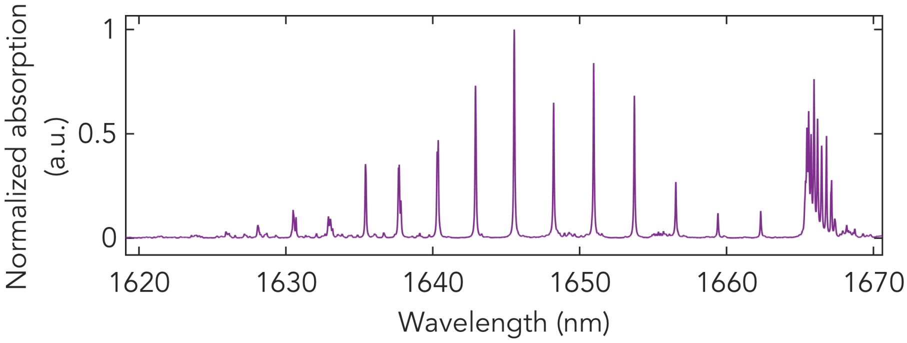

Figure 5.10 2v3 overtone absorption of methane modelled with HITRAN 2012 database.

The spectral object which is the absorption spectrum of methane is sparse due to the sub-nm linewidth of the lines compared to the several tens of nm broad spectral measurement window. This means that light is mostly transmitted independently of the probing random spectral fluctuations and therefore the integrated intensity measured in the test arm exhibit small variations from shot-to-shot. We then use the differential processing approach described earlier to increase the sensitivity of the correlation measurement. Furthermore, because the variance of the spectral fluctuations follows the Gaussian spectral envelope of the spectral filter placed after the SC, the ghost image is distorted by a similar Gaussian envelope and a low-pass filter is applied in the Fourier domain to remove the distortion as discussed in the previous subsection.

Figure 5.11 shows an illustrative result of the ghost image of the methane absorption lines obtained from 22,000 realizations. For comparison, a direct measurement performed with the same SC source and an OSA is also plotted in the figure. Note that the latter was also post-processed in the Fourier domain to remove the distortion rising from the spectral envelope of the SC spectrum. The spectral resolution of the OSA was set to 0.2 nm, close to the theoretical resolution of the ghost imaging

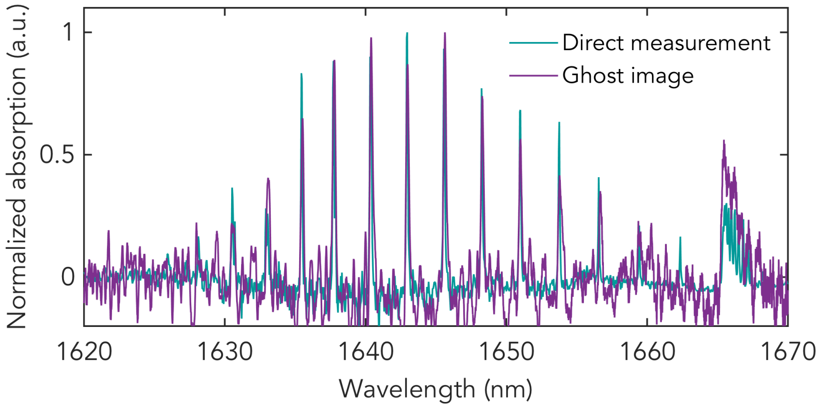

Figure 5.11 Absorption spectrum of methane retrieved with the spectral domain ghost imaging approach using 22,000 realizations (purple line) compared with a direct OSA measurement (blue line). Adapted from Publication III.

scheme. There is a very good agreement between the ghost imaging approach and the direct measurement but one can also notice that the SNR is higher in the direct measurement. This is mainly due to the fact the OSA is recording the spectrum with a highly sensitive detector as compared to the detectors used in the ghost imaging measurements.

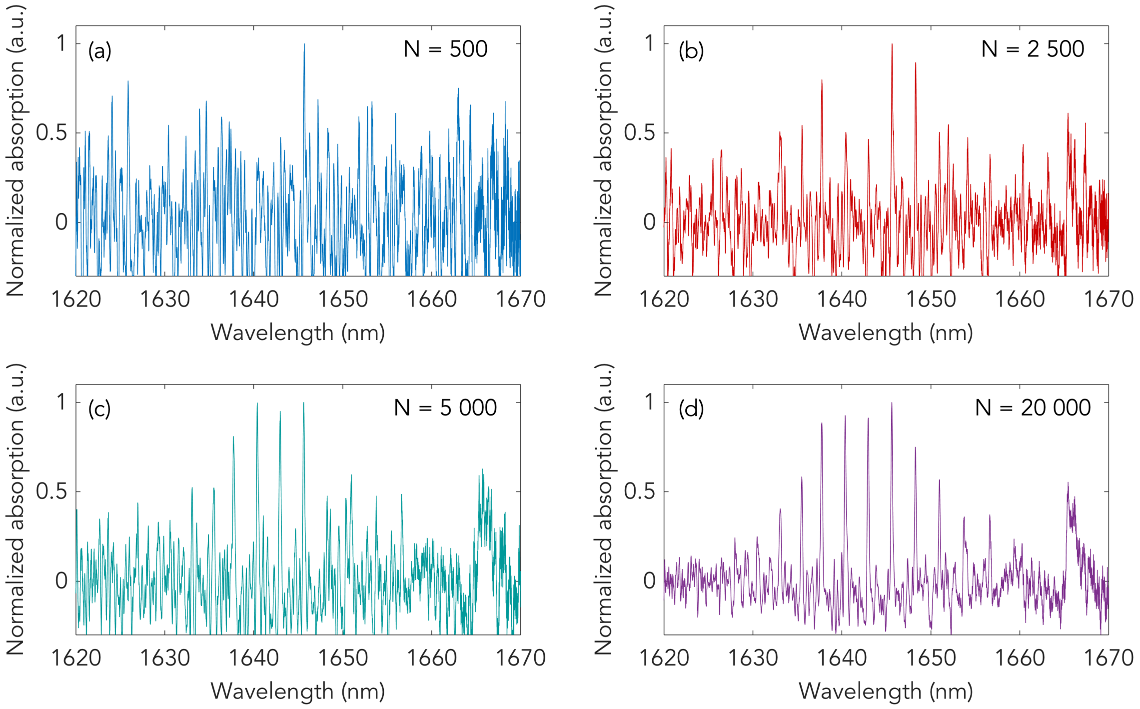

Figure 5.12 Impact of the number of realizations N on the ghost image SNR. All retrieved spectra have been normalized for convenient comparison. Adapted from Publication III.

The effect of the number of acquisitions on the retrieved ghost image is conveniently shown in Fig. 5.12 with the different sub-panels plotting the correlation function of Eq. (5.6) for an increasing number of acquisitions as indicated. One can indeed observe how the SNR improves with the number of acquisitions but also that absorption lines stand out from the noise with as little as 2,500 distinct realizations. In practice, it can be shown that the SNR increases as the square-root of the number of acquisitions [152].

The benefits of the differential ghost imaging method is illustrated in Fig. 5.13 where the left panel shows the ghost image obtained from the DGI method [Eq. (5.6)] while the right panel shows the ghost image retrieved from the conventional ghost image correlation function [Eq. (5.1) with $x = \lambda$].

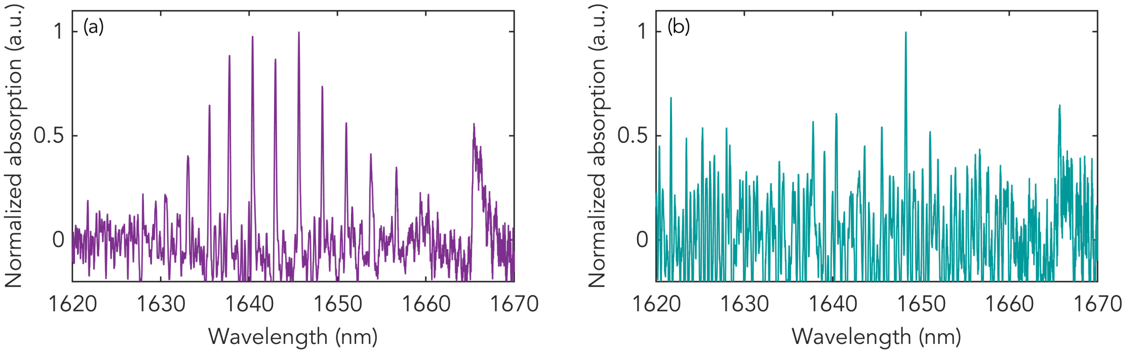

Figure 5.13 Ghost image with (left) and without DGI post-processing (right) generated from 22,000 realizations.

Both ghost images were generated from the same number of 22,000 acquisitions. It is evident that when the conventional approach is used, the ghost imaging scheme is only able to retrieve the broad absorption feature at around 1666 nm. As mentioned above, this is because the conventional approach is much less sensitive than the differential ghost imaging approach to small variations in the test arm signal induced by sparse features and corresponding to the absorption lines of narrow linewidth.

Finally, we also illustrate the distortion in the ghost image due to the non-uniform variance of the probing spectral fluctuations over the measurement window in Fig. 5.14. More specifically, Fig. 5.14(a) shows how, in absence of post-processing with a notch filter, there is a broad background component in the ghost image which essentially follows the spectral-dependence of the probing fluctuations variance. Figure 5.14(b) shows the ghost image of the absorption spectrum after post-filtering in the Fourier space using a notch-filter (inverted super-Gaussian of order eight). One can

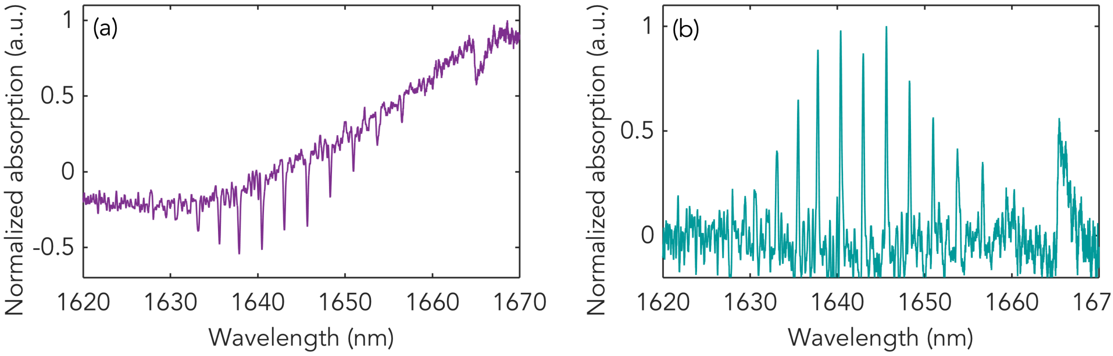

Figure 5.14 Ghost image obtained with 22,000 realizations without (a) and with (b) Fourier domain processing using a notch filter.

see how the Fourier filtering process is effective in suppressing the slowly-varying background component as compared to the rapidly-varying gas absorption features. Of course such post-filtering processing should be used with care as it may partially affect broad spectral absorption features that the object may include. A clear example in the case of the methane 2v3 overtone absorption spectrum characterized here is the broad absorption line at 1666 nm which may be altered if the parameters of the notch filter are poorly chosen.

5.3 Ghost optical coherence tomography

5.3.1 Optical coherence tomography in the spectral domain

Optical coherence tomography (OCT) is an interferometry technique allowing for the generation of cross-sectional images with high in-depth or axial resolution [1, 153]. OCT measures the interference pattern resulting from the superposition of light reflected or scattered off an object to be imaged with that from a reference arm. Interferences are only manifested if the optical path difference between the two arms in the interferometer is shorter than the coherence length of the light source. The interference pattern provides a direct measure of the time delay between the two interferometer arms induced by the presence of the object in one arm, enabling high resolution imaging. The resolution of OCT is determined by the coherence length of the light source, hence the need for broadband sources (the coherence length is inversely proportional to the spectral bandwidth). OCT is commonly used in medical applications due to its non-invasive character and ability to image biological samples without any contrast agents [153,154]. OCT is also routinely used in industrial applications for quality control of materials or components [155,156]. OCT was originally developed in the time-domain where the interference pattern and thus the optical path difference is measured as the position of the reference mirrors is mechanically scanned allowing to image at different depth inside the object [153,157]. OCT has been subsequently expanded into the spectral domain where light echoes are measured simultaneously from all time delays [158].

Unlike time-domain OCT, spectral-domain OCT does not require scanning along the sample direction resulting in very fast acquisition speeds. Spectral-domain OCT requires a broadband light source which may be in the form of an incoherent LED, a narrow band tunable source with very fast sweeping time (so-called swept-source) [159], or a supercontinuum [153, 160]. In what follows we focus our attention to spectral-domain OCT, which is nowadays the approach of choice for OCT imaging.

A typical layout of spectral-domain OCT is presented in Fig. 5.15(a). Light from a broadband source is divided equally between two paths with a beam splitter. Light reflected from the reference mirror interfere with light reflected from the sample and the interference pattern is measured in the spectral domain with a spectrometer [see Fig. 5.15(b)]. Each sub-interface composing the object induces a specific optical path difference resulting in a given period in the spectral interference pattern. The Fourier transform of the spectral interferogram provides a measure of the distance between each sub-interface and their relative reflection coefficient [see Fig. 5.15(c)]. More specifically, the spectral interference pattern is given by:

$$I(\omega) = I_S(\omega)\left\{1 + \sum_i r_i^2 + \sum_{i\neq j} r_i r_j \cos\left[2\omega(z_i - z_j)/c\right] + \sum_i r_i^2 \cos(2\omega z_i/c)\right\} \quad (5.9)$$

where $I_S(\omega)$ represents the spectral intensity from the source. r_i and z_i are the amplitude reflection coefficient and distance from the zero-path difference of each sub-interface along the surface normal, respectively. Note that here the distance is meant as an optical path such that the refractive index n_i of sub-interface i is included in z_i. Distance and intensity reflection of each sub-interface can then be retrieved from the interferogram by Fourier transform:

$$\tilde{I}(z) = \Gamma(z) \otimes \left\{ \left(1 + \sum_i r_i^2\right) \delta(0) + \sum_i r_i^2 \delta(z \pm 2z_i) + \sum_i r_i r_j \delta \left[z \pm 2(z_i - z_j)\right] \right\}, \tag{5.10}$$

where $\tilde{I}(z)$ is the Fourier transform of the spectral interferogram in the distance (Fourier) space z, Γ is the autocorrelation function (also known as the coherence function) of the source spectrum, and δ is the delta-function. The first term is a DC-term corresponding to the autocorrelation from the reference arm. The second term arises from interference between the reference and sample arms and carries the information on the sub-interface relative positions and reflectivities. The last term arises from interference between the multiple interfaces in the sample arm and is typically located near the DC term. From the equation above, it can be seen that the axial resolution along the z-axis is determined by the width of the autocorrelation function Γ. For a Gaussian spectral envelope, the autocorrelation function is also Gaussian, with a width inversely proportional to the bandwidth $\Delta\lambda$ of the spectral envelope. Specifically, the axial resolution δz is given by: [161]

$$\delta z = \frac{2 \ln 2}{\pi} \frac{\lambda_0^2}{\Delta\lambda}, \tag{5.11}$$

where λ_0 is the central wavelength of the light source. This means that the resolution is improved for light sources of shorter central wavelength and broader bandwidth. The total imaging depth on the other hand (i.e. the maximum axial distance over which the different sub-interfaces can be imaged) depends on the resolution of the spectrometer that is used to record the spectral interference pattern [161].

For the case of a single interface with reflectivity r and position z_0 (relative to the zero-path difference) Eq. (5.10) reduces to

$$\tilde{I}(z) = \Gamma(z) \otimes \left\{ \left(1 + r^2\right) \delta(0) + r^2 \delta(z \pm 2z_0) \right\}, \tag{5.12}$$

while for a dual interface with identical reflectivities r and positions z_1 and z_2 (relative to the zero-path difference) there is an additional term arising from self-interference between the two interfaces:

$$\tilde{I}(z) = \Gamma(z) \otimes \left\{ \left(1 + 2r^2\right) \delta(0) + r^2 \delta(z \pm 2z_1) + r^2 \delta(z \pm 2z_2) + 2r^2 \delta(z \pm 2(z_1 - z_2)) \right\}. \tag{5.13}$$

Note that in all cases, the Fourier transform of the interferogram has both positive and negative components in the Fourier space which carry redundant information such that discarding the negative distances in the Fourier space is common practice.

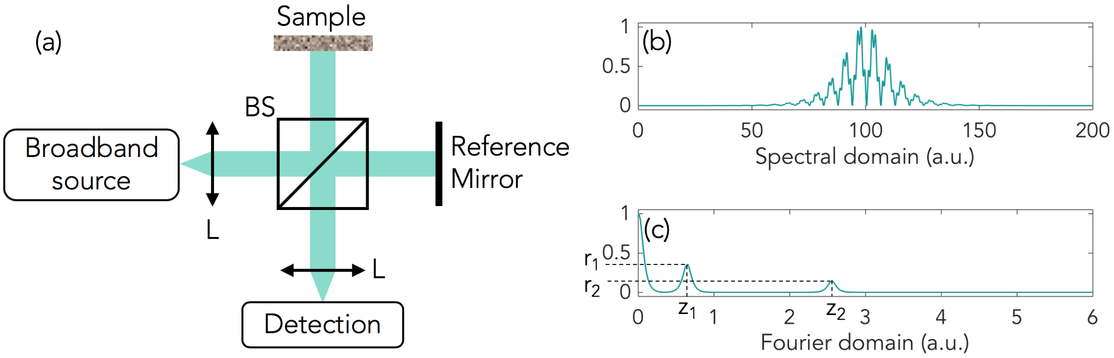

Figure 5.15 (a) Experimental setup of conventional spectral-domain OCT . BS: beam splitter, L: lens. (b) Normalized interference pattern measured in the spectral domain for a dual-interface sample. (c) Normalized Fourier transform of (b) illustrating the relative positions of the sample interfaces and their associated reflectivities.

5.3.2 Ghost OCT

We next apply the spectral-domain ghost imaging method to measure the spectral interference pattern generated by a spectral OCT interferometer in which a test sample has been inserted. In other words, the spectral interference arising from the sample in the interferometer here plays the role of the object in the spectral-domain ghost imaging setup. The Fourier transform of the ghost image then produces an axial scan of the sample. We stress that the spectral object in this case (the interference pattern) differs from the actual physical object that is eventually imaged via Fourier transform of the spectral object. In all what follows, we use the term spectral object in reference to the spectral interference pattern while we specify the physical object to be imaged when needed. Ghost OCT is thus an imaging technique performed in the spectral domain producing images of spatial objects and it can be seen as an alternative to conventional ghost imaging performed in the spatial domain, but with high depth-resolution [162]. The technique also possesses all the benefits of ghost imaging as described in the introduction to this chapter. The first demonstration of such a ghost OCT scheme is reported in Publication IV.

Experimental setup

The experimental setup for Ghost OCT is presented in Fig. 5.16. It is similar to the setup used to perform spectroscopy (Fig. 5.8) as described in Section 5.2 except that the gas cell is now replaced by a Michelson interferometer in which a physical object is placed. The broadband light source is a supercontinuum similar to that used in the demonstration of absorption spectroscopy. The SC is filtered by a combination of LPF and NBF. The beam is then injected into a single-mode fiber (SMF) divided with a 99/1 fiber beam splitter. The 99% arm is sent into the DCM that performs the dispersive Fourier transform to measure the spectral fluctuations of the SC in real-time. 1% of the intensity is directed to the test arm where the OCT Michelson interferometer is located. The beam is collimated at the entrance of the test arm into a 4 mm diameter beam with a reflective collimator. The beam is split equally into two paths using a free-space cubic beam splitter between a reference mirror and the sample under test. After reflection from the mirror and the sample, the beams are recombined and injected into a SMF whose output intensity is measured by a (slow) integrating detector with no spectral resolution. Measurement of the interferometer output alone thus does not carry any meaningful information and it is only the correlation with the real-time spectral fluctuations measured in the reference arm of the ghost OCT setup that allows to retrieve the spectral interferogram resulting from the presence of the sample in the OCT interferometer. The axial resolution is identical to that of conventional spectral-domain OCT and is inversely proportional to the source spectral bandwidth. The imaging depth of the system on the other hand is determined by the resolution with which the spectral intensity fluctuations are measured by the dispersive Fourier transform.

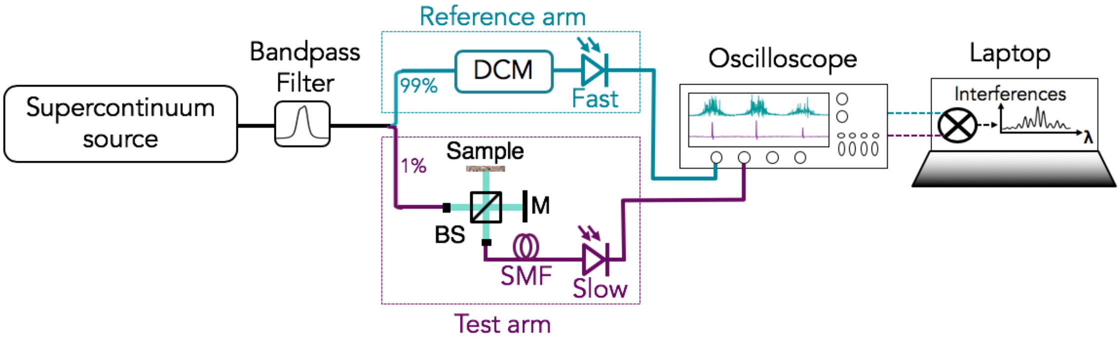

Figure 5.16 Experimental setup of ghost OCT. DCM: dispersion compensation module, BS: beam splitter, M: mirror, SMF: single-mode fiber.

Experimental considerations

Interferometry is in general highly sensitive to perturbations, including mechanical vibrations or temperature variations, thus it is important to minimize the overall measurement time required to record a large number of different acquisition corresponding to different spectral probing patterns. Note that this constraint is much more relaxed in the demonstration of spectroscopy reported in the previous section as it does not involve interference. In order to increase the number of acquisitions, the sampling rate of the oscilloscope was decreased to 6.25 GS/s allowing to record 10,000 acquisitions at once, after which the memory is full. Because of the reduced sampling rate we used, the local bandwidth of the SC spectral intensity fluctuations was increased by c.a. 1.5 times compared to the spectroscopic measurement case. In practice, this was achieved by decreasing by about 10% the peak power injected into the dispersion-shifted fiber to generate the SC. The resolution of the spectral fluctuations is again limited by the 1.2 GHz detector used in the reference arm and is 0.3 nm (unchanged compared to ghost imaging spectroscopy experiments) and the sampling rate of 6.25 GS/s is then sufficient to resolve the spectral interferogram generated from the correlation of the reference and test arms.

Calibration of the experimental setup

We first performed a test experiment where the object in the OCT interferometer is a highly reflective moving mirror. The mirror-object position corresponding to the interferometer zero-path difference was first identified using an OSA. For this particular position, no spectral interference appears in the spectrum measured by the OSA at the interferometer output. The OSA was subsequently replaced by the slow integrating detector with no spectral resolution and the mirror-object position was detuned from the interferometer zero-path difference in step of 100 µm and over a total distance of 11 mm.

For each mirror position, a series of 10,000 acquisitions was recorded simultaneously at the output of the reference arm of the ghost imaging setup and at the output of the test arm after the OCT interferometer. Because the object to be retrieved (the spectral interference at the OCT interferometer output) is not sparse, the correlation between the reference and test arm signals was evaluated directly without any differential scheme as used in the spectroscopic experiments. The correlation

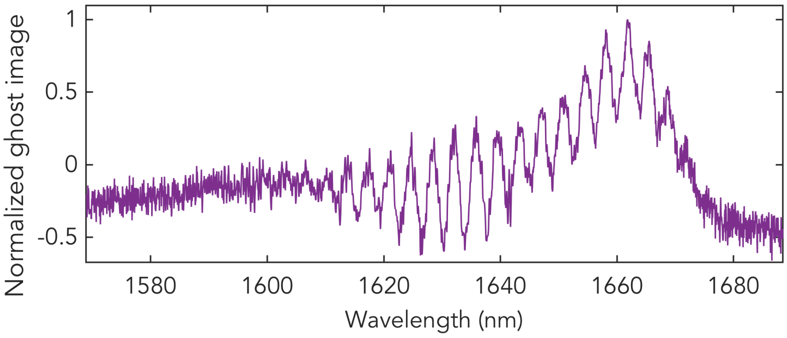

Figure 5.17 Ghost image of the interference pattern for Δd=0.6 mm.

computed over the 10,000 acquisition for a particular position of the mirror-object is shown in Fig. 5.17 and we can see how the spectral interference pattern is nicely revealed by the spectral-domain ghost imaging scheme. The Fourier transform of the retrieved ghost interferogram then provides a direct measurement of the mirror object position with respect to the zero-path difference. For comparison we also performed similar measurements using a conventional OCT approach, i.e. by measuring the output of the interferometer with an OSA.

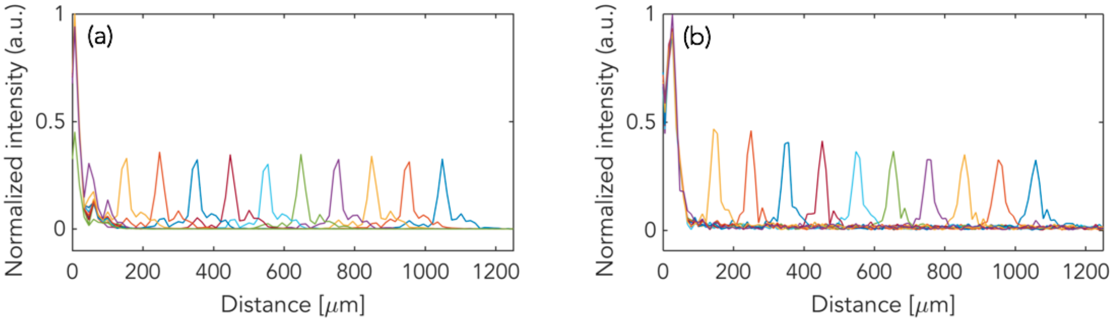

Figure 5.18 Calibration with a moving mirror as the object: (a) conventional OCT, (b) GOCT. The different colors correspond to different positions of the moving mirror in steps of 100 µm. Adapted from Publication IV.

Figure 5.18 compares the results obtained from the spectral-domain ghost OCT configuration with that from a conventional spectral-domain OCT approach. The two methods lead to similar results and the retrieved mirror-object position coincides very well with the value sets manually on the translation stage. Note that in the figure, the x-axis represents half of the optical path difference between both arms (0 being the zero-path difference) thus corresponding directly to the movement of the mirror mounted on the translation stage. Note also that, here, the optical path is equal to the geometric path as light propagates in air.

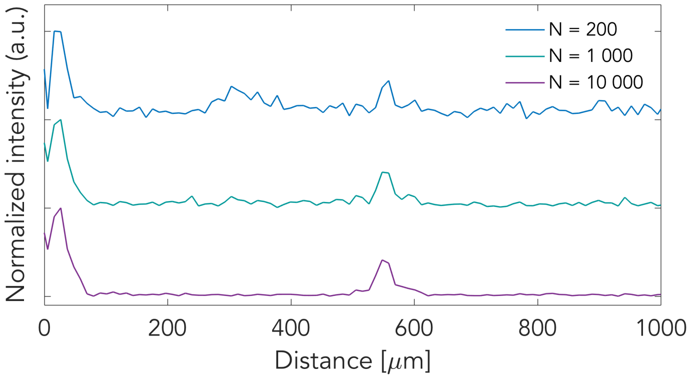

Figure 5.19 Fourier transform of the ghost image for an increasing number of realizations as indicated. For clarity, an arbitrary vertical offset was added for each case. Adapted from Publication IV.

Just as in the previous application to spectroscopy when using random probing fluctuations, the SNR of the spectral interferogram ghost replica depends on the number of acquisitions and this is illustrated in Fig. 5.19 showing the Fourier transform of the ghost interferogram (and thus the position of the mirror-object) for an increasing number of acquisitions from 200 to 10,000. However, here because the spectral object is an interference pattern, the object is not sparse but rather near an ideal binary object where bright and dark fringes correspond to 1 and 0. A direct consequence is that for a fixed number of acquisitions, the SNR is increased as compared to the case of a sparse spectral object (such as a gas absorption spectrum). This can be clearly seen in the figure where the peak in the Fourier domain corresponding to the mirror-object position is identified with as little as 200 realizations, while for 1,000 acquisitions it is well above the noise floor.

Measurement of a dual-interface

In a second series of experiments, we replaced the mirror-object with a dual air-glass interface in the form of a microscope cover slip. The cover slip is mounted on a kinematic mount for alignment purposes. In order to unambiguously discriminate the positions of the two air-glass interfaces in the Fourier domain, the reference mirror was detuned from the zero optical path difference by 1 mm so that their associated Fourier peaks do not overlap with the central autocorrelation peak. OCT measurements were performed indirectly with the ghost imaging method and compared with a direct measurement using the OSA placed at the output of the test arm. The ghost imaging results are shown in Fig. 5.20(a) and the OSA measurement in Fig. 5.20(b). The results are very similar except for a slightly broadened central peak corresponding to the autocorrelation of the reference path in the OCT interferometer. This may be eliminated by using an increased sampling rate in the measurement of the reference and test arms. The double peaks around 1000 μm mark the reflections from both interfaces of the microscope cover slip. Note that the peaks are centered around the optical path difference set in the OCT interferometer as mentioned above. One can see that the optical path length difference between the two peaks marking the positions of the two air-glass interfaces is 218 μm, corresponding to a physical thickness of c.a. 145 μm ($n_{ref} = 1.5$) for the cover slip. The measured thickness is in very good agreement with the nominal value of 150 μm provided by the manufacturer. The small peak at around 220 μm is due to self-interference between the two cover slips interfaces.

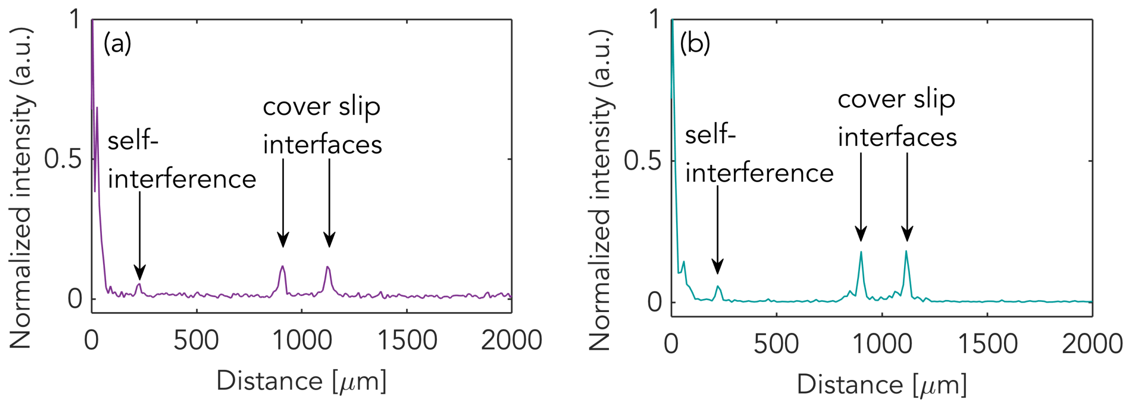

Figure 5.20 Fourier transform of the ghost image of a microscope slip as the object (a) retrieved with ghost OCT method and (b) with conventional OCT.

Finally, we compare in Fig. 5.21 the performance of the differential ghost imaging scheme [Eq. (5.6)] vs. that of the standard ghost imaging method [Eq. (5.1) with $x = \lambda$]. We remind that the difference between the two approaches lies only in the post-processing applied to the recorded data but the experimental setup are otherwise identical. In the case of ghost spectral-domain OCT, the object to be retrieved is an interference pattern which is not sparse. In fact, the bright and dark fringes of the interferogram correspond to full or zero transmission such that the spectral object to be retrieved here transmits 50% of the light on average. One would therefore expect in this case that the standard approach performs as well as the differential scheme. But in fact, it turns out that the DGI post-processing still has a better sensitivity in this case. Indeed, when comparing the Fourier transform of the retrieved interferogram, one can see how the DGI post-processing [Fig. 5.21(a)] captures the self-interference between the two air-glass interfaces while the standard GI does not [Fig. 5.21(b)]. We also note that the amplitude of the peaks corresponding to the air-glass interfaces is larger than when using the DGI approach.

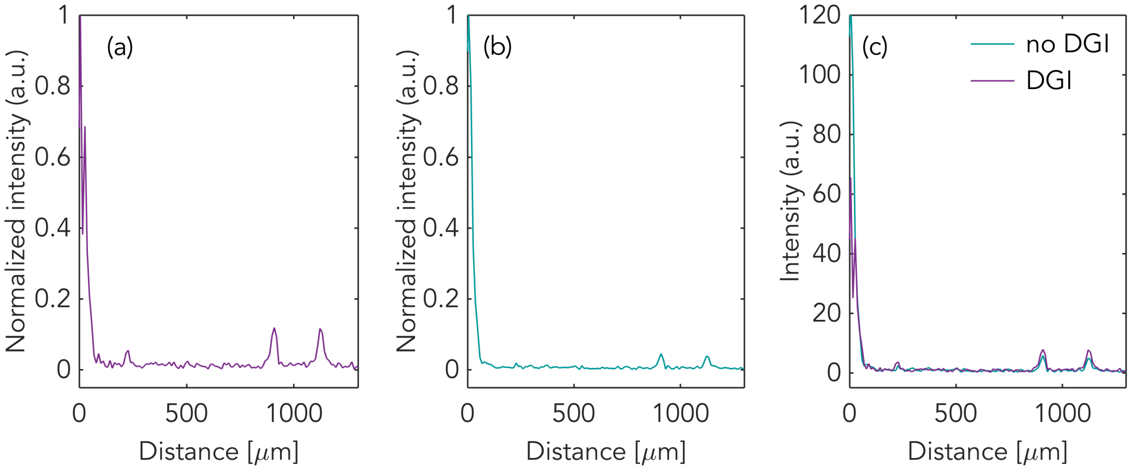

Figure 5.21 Normalized plots of the absolute value of the Fourier transform (a) with the DGI method and (b) without DGI. (c) shows both plots before normalization.

5.4 Conclusion

In this chapter, we have demonstrated new approaches to broadband sensing and imaging using the novel concept of ghost imaging in the spectral domain. We have also shown that an incoherent broadband supercontinuum source is ideal for this purpose as the randomness and the sharpness of its spectral fluctuations provide ideal features to perform ghost imaging. Spectral-domain ghost imaging allows detection of the object with an integrating slow detector providing an alternative when precise detectors are not available for a specific wavelength range or in cases where the object is highly absorbing, scattering or damaged when exposed to large intensities. It is also insensitive to (linear) perturbations after the object to be characterized. The demonstrated technique is a proof-of-principle concept which may be extended and improved in several aspects. For example, if random probing spectral fluctuations are used, they may be measured at a different wavelength range by using e.g. nonlinear up- or down-conversion in a crystal or waveguides as the nonlinear conversion process should conserve the correlation and indeed preliminary results not reported here show that this is the case. This can allow for characterizing a sample in a spectral region where fast and sensitive detectors do not exist, yet measuring in real-time the probing spectral fluctuations in a wavelength band where fast detectors are available. Another interesting extension would be to use a source with pre-programmable and controllable spectral fluctuations, removing the need to measure the reference arm since the probings patterns are known in this case. This method similar to compressive sensing strategies with (mathematically) orthogonal patterns would also reduce considerably the number of acquisitions needed to retrieve the object replica with high accuracy. Computational spectral-domain ghost imaging could be implemented e.g. using a broadband LED and a spatial light modulator where dispersed spectral components are individually modulated and subsequently recombined, or using frequency comb generated from two tunable continuous-wave lasers injected into a nonlinear fiber or waveguide and whose free-spectral range can be tuned.

6. SUMMARY AND PERSPECTIVES

Optical sensing and imaging techniques are essential to image distant objects, visualize objects on small scales, quantify or identify substances, monitor evolutive phenomena and even understand dynamical physical processes. Various techniques are already widespread and in use commercially while others are still under development in research laboratories. With the ever-increasing demand for better precision, enhanced sensitivity, and the exploitation of novel spectral windows, sensing and imaging techniques continue to be the subject of intense research efforts. These research efforts are equally spread among the different aspects of optical measurement techniques, from the development of sources of light with improved characteristics to detection schemes with enhanced sensitivity and increased speed, and of course new approaches for specific regimes. This thesis brings novel and original contributions to the field of sensing and imaging, both from the light source development viewpoint and from the detection scheme perspective. All the concepts described in this work are demonstrated and validated experimentally, providing alternative paths for future technologies.

In the first part of this work, we demonstrated that cavity enhanced absorption spectroscopy was possible in the mid-infrared domain, where molecules are highly absorbing, which can lead to lower detection limits. The supercontinuum source has a significant advantage arising from its high brightness, wide spectrum and high spatial coherence. These properties were key to demonstrate multiple-gas detection over a bandwidth as large as 500 nm, which today constitutes the largest continuous detection range in the mid-infrared spectral region. We have shown that the technique is reliable with excellent agreement between the nominal and retrieved concentrations. The current detection limit is at the sub-ppm level but we anticipate that with the new sources that are being currently developed in our or other laboratories, the detection limit could be lowered to the part-per-billion level.

We then demonstrated that supercontinuum sources are equally promising candidates for background-free, broadband, photoacoustic detection in the mid-infrared, showing clear improvements over the conventional approach that uses a black-body source. While the demonstrated part-per-million-level detection limit may not sound yet overly impressive, it is also clear that one can expect dramatic improvements when using supercontinuum sources with lower intensity noise. The method has also the potential to be miniaturized, which could be commercially exploited in the near future.

The last part of the work was devoted to the demonstration of a new proof-of-concept indirect approach for sensing and imaging, that could potentially be an alternative to other conventional techniques for samples which are highly absorbing, diffusing or with a low damage threshold, and in spectral regions where sensitive and fast detectors are not available. This concept is based on the transposition of ghost imaging into the spectral-domain and again a supercontinuum source is ideal for this purpose. The approach was applied to broadband spectroscopy allowing to retrieve absorption features of trace gas with sub-nanometer resolution. The application of the technique to remote atmospheric detection would prove to be a major development in the field of remote sensing. Spectral domain ghost imaging was subsequently combined with traditional optical coherence tomography to image physical objects. Such a ghost optical coherent tomography method can retrieve images with high in-depth resolution and could prove to have a significant advantage for imaging through highly scattering media. Spectral-domain ghost imaging may be further refined in the future using controlled and pre-programmed spectral fluctuations via e.g. frequency combs, allowing for much faster acquisition speeds and improved signal-to-noise ratio.

In conclusion, the work reported in this thesis offers novel sensing and imaging techniques that will certainly be useful for future developments and contribute seeding new ideas for future research in these fields.

REFERENCES

[1] D. Huang, E. Swanson, C. Lin, J. Schuman, W. Stinson, W. Chang, M. Hee, T. Flotte, K. Gregory, and C. Puliafito, “Optical coherence tomography,” Science, vol. 254, no. 5035, pp. 1178–1181, 1991.

[2] J. M. Schmitt, A. Knüttel, and R. F. Bonner, “Measurement of optical properties of biological tissues by low-coherence reflectometry,” Applied Optics, vol. 32, no. 30, pp. 6032–6042, 1993.

[3] J. M. Schmitt and A. Knüttel, “Model of optical coherence tomography of heterogeneous tissue,” Journal of the Optical Society of America A, vol. 14, no. 6, pp. 1231–1242, 1997.

[4] A. M. Sergeev, V. M. Gelikonov, G. V. Gelikonov, F. I. Feldchtein, R. V. Kuranov, N. D. Gladkova, N. M. Shakhova, L. B. Snopova, A. V. Shakhov, I. A. Kuznetzova, A. N. Denisenko, V. V. Pochinko, Y. P. Chumakov, and O. S. Streltzova, “In vivo endoscopic oct imaging of precancer and cancer states of human mucosa,” Optics Express, vol. 1, no. 13, pp. 432–440, 1997.

[5] G. Song, T. Qin, H. Liu, G.-B. Xu, Y.-Y. Pan, F.-X. Xiong, K.-S. Gu, G.-P. Sun, and Z.-D. Chen, “Quantitative breath analysis of volatile organic compounds of lung cancer patients,” Lung Cancer, vol. 67, no. 2, pp. 227–231, 2010.

[6] A. Bajtarevic, C. Ager, M. Pienz, M. Klieber, K. Schwarz, M. Ligor, T. Ligor, W. Filipiak, H. Denz, and M. Fiegl, “Noninvasive detection of lung cancer by analysis of exhaled breath,” BMC Cancer, vol. 9, no. 1, p. 348, 2009.

[7] W. Miekisch, J. K. Schubert, and G. F. Noeldge-Schomburg, “Diagnostic potential of breath analysis focus on volatile organic compounds,” Clinica Chimica Acta, vol. 347, no. 1, pp. 25 – 39, 2004.

[8] F. K. Tittel, D. Richter, and A. Fried, Mid-Infrared Laser Applications in Spectroscopy. Berlin, Heidelberg: Springer Berlin Heidelberg, 2003, pp. 458–529.

[9] M. Todd, R. Provencal, T. Owano, B. Paldus, A. Kachanov, K. Vodopyanov, M. Hunter, S. Coy, J. Steinfeld, and J. Arnold, "Application of mid-infrared cavity-ringdown spectroscopy to trace explosives vapor detection using a broadly tunable (6–8 µm) optical parametric oscillator," Applied Physics B, vol. 75, no. 2-3, pp. 367–376, 2002.

[10] R. K. Dukor and C. A. Marcott, "Method and system for diagnosing pathology in biological samples by detection of infrared spectral markers," Jan. 11 2005, US Patent 6,841,388.

[11] A. C. McIntyre, M. L. Bilyk, A. Nordon, G. Colquhoun, and D. Littlejohn, "Detection of counterfeit scotch whisky samples using mid-infrared spectrometry with an attenuated total reflectance probe incorporating polycrystalline silver halide fibres," Analytica Chimica Acta, vol. 690, no. 2, pp. 228–233, 2011.

[12] G. Genty, Supercontinuum generation in microstructured fibers and novel optical measurement techniques. Helsinki University of Technology, 2004.

[13] G. Kirchhoff and R. Bunsen, "Chemische analyse durch spectralbeobachtungen," Annalen der Physik, vol. 186, no. 6, pp. 161–189, 1860.

[14] S. Mason, "Lines of light-the sources of dispersive spectroscopy, 1800-1930, by jcd brand," Nature, vol. 381, no. 6582, pp. 488–488, 1996.

[15] V. Thomsen, "A timeline of atomic spectroscopy," Spectroscopy, vol. 21, no. 10, p. 32, 2006.

[16] A. Coustenis, A. Salama, B. Schulz, S. Ott, E. Lellouch, T. Encrenaz, D. Gautier, and H. Feuchtgruber, "Titan's atmosphere from iso mid-infrared spectroscopy," Icarus, vol. 161, no. 2, pp. 383–403, 2003.

[17] R. Meier, "Ultraviolet spectroscopy and remote sensing of the upper atmosphere," Space Science Reviews, vol. 58, no. 1, pp. 1–185, 1991.

[18] C. Wang and P. Sahay, "Breath analysis using laser spectroscopic techniques: breath biomarkers, spectral fingerprints, and detection limits," Sensors, vol. 9, no. 10, pp. 8230–8262, 2009.

[19] M. J. Thorpe, D. Balslev-Clausen, M. S. Kirchner, and J. Ye, "Cavity-enhanced optical frequency comb spectroscopy: application to human breath analysis," Optics Express, vol. 16, no. 4, pp. 2387–2397, 2008.

[20] H. Schiff, G. Mackay, and J. Bechara, "The use of tunable diode laser absorption spectroscopy for atmospheric measurements," Research on Chemical Intermediates, vol. 20, no. 3-5, pp. 525–556, 1994.

[21] C. N. Banwell and E. M. McCash, Fundamentals of molecular spectroscopy. McGraw-Hill New York, 1994, vol. 851.

[22] K. Nakanishi, Infrared absorption spectroscopy, practical. Holden-Day, 1962.

[23] J. Chou, Y. Han, and B. Jalali, "Time-wavelength spectroscopy for chemical sensing," IEEE Photonics Technology Letters, vol. 16, no. 4, pp. 1140–1142, 2004.

[24] U. Platt and J. Stutz, "Differential absorption spectroscopy," in Differential Optical Absorption Spectroscopy. Springer, 2008, pp. 135–174.

[25] R. White, Chromatography/Fourier transform infrared spectroscopy and its applications. CRC Press, 1989, vol. 10.

[26] B. C. Smith, Fundamentals of Fourier transform infrared spectroscopy. CRC press, 2011.

[27] K. MacAdam, A. Steinbach, and C. Wieman, "A narrow-band tunable diode laser system with grating feedback, and a saturated absorption spectrometer for cs and rb," American Journal of Physics, vol. 60, no. 12, pp. 1098–1111, 1992.

[28] G. C. Bjorklund, "Frequency-modulation spectroscopy: a new method for measuring weak absorptions and dispersions," Optics Letters, vol. 5, no. 1, pp. 15–17, 1980.

[29] L. C. Philippe and R. K. Hanson, "Laser diode wavelength-modulation spectroscopy for simultaneous measurement of temperature, pressure, and velocity in shock-heated oxygen flows," Applied Optics, vol. 32, no. 30, pp. 6090–6103, 1993.

[30] M. D. Wheeler, S. M. Newman, A. J. Orr-Ewing, and M. N. R. Ashfold, "Cavity ring-down spectroscopy," Journal of the Chemical Society, Faraday Trans., vol. 94, pp. 337–351, 1998.

[31] R. Engeln, G. Berden, R. Peeters, and G. Meijer, “Cavity enhanced absorption and cavity enhanced magnetic rotation spectroscopy,” Review of Scientific Instruments, vol. 69, no. 11, pp. 3763–3769, 1998.

[32] A. Foltynowicz, F. M. Schmidt, W. Ma, and O. Axner, “Noise-immune cavity-enhanced optical heterodyne molecular spectroscopy: Current status and future potential,” Applied Physics B, vol. 92, no. 3, p. 313, 2008.

[33] K. Fuwa and B. Valle, “The physical basis of analytical atomic absorption spectrometry. the pertinence of the beer-lambert law.” Analytical Chemistry, vol. 35, no. 8, pp. 942–946, 1963.

[34] D. Kaur, A. De Souza, J. Wanna, S. A. Hammad, L. Mercorelli, and D. S. Perry, “Multipass cell for molecular beam absorption spectroscopy,” Applied Optics, vol. 29, no. 1, pp. 119–124, 1990.

[35] D. Romanini, A. Kachanov, N. Sadeghi, and F. Stoeckel, “Cw cavity ring down spectroscopy,” Chemical Physics Letters, vol. 264, no. 3-4, pp. 316–322, 1997.

[36] P. Zalicki and R. N. Zare, “Cavity ring-down spectroscopy for quantitative absorption measurements,” The Journal of Chemical Physics, vol. 102, no. 7, pp. 2708–2717, 1995.

[37] G. Meijer, M. G. Boogaarts, R. T. Jongma, D. H. Parker, and A. M. Wodtke, “Coherent cavity ring down spectroscopy,” Chemical Physics Letters, vol. 217, no. 1-2, pp. 112–116, 1994.

[38] M. D. Wheeler, S. M. Newman, A. J. Orr-Ewing, and M. N. Ashfold, “Cavity ring-down spectroscopy,” Journal of the Chemical Society, Faraday Transactions, vol. 94, no. 3, pp. 337–351, 1998.

[39] A. Aalto, G. Genty, T. Laurila, and J. Toivonen, “Incoherent broadband cavity enhanced absorption spectroscopy using supercontinuum and superluminescent diode sources,” Optics Express, vol. 23, no. 19, pp. 25 225–25 234, 2015.

[40] I. Ventrillard-Courtillot, T. Gonthiez, C. Clerici, and D. Romanini, “Multispecies breath analysis faster than a single respiratory cycle by optical-feedback cavity-enhanced absorption spectroscopy,” Journal of Biomedical Optics, vol. 14, no. 6, p. 064026, 2009.

[41] A. Rosencwaig and A. Gersho, “Theory of the photoacoustic effect with solids,” Journal of Applied Physics, vol. 47, no. 1, pp. 64–69, 1976.

[42] F. A. McDonald and G. C. Wetsel Jr, “Generalized theory of the photoacoustic effect,” Journal of Applied Physics, vol. 49, no. 4, pp. 2313–2322, 1978.

[43] A. Rosencwaig, Photoacoustics and photoacoustic spectroscopy. Wiley, 1980.

[44] T. Laurila, H. Cattaneo, V. Koskinen, J. Kauppinen, and R. Hernberg, “Diode laser-based photoacoustic spectroscopy with interferometrically-enhanced cantilever detection,” Optics Express, vol. 13, no. 7, pp. 2453–2458, 2005.

[45] K. Wilcken and J. Kauppinen, “Optimization of a microphone for photoacoustic spectroscopy,” Applied spectroscopy, vol. 57, no. 9, pp. 1087–1092, 2003.

[46] P. Spencer, D. J. Trylovich, and C. M. Cobb, “Chemical characterization of lased root surfaces using fourier transform infrared photoacoustic spectroscopy,” Journal of periodontology, vol. 63, no. 7, pp. 633–636, 1992.

[47] J. R. Birch, “Dispersive fourier transform spectroscopy,” Microchimica Acta, vol. 93, no. 1-6, pp. 105–122, 1987.

[48] K. Goda and B. Jalali, “Dispersive fourier transformation for fast continuous single-shot measurements,” Nature Photonics, vol. 7, pp. 102 EP –, 2013.

[49] D. Solli, J. Chou, and B. Jalali, “Amplified wavelength–time transformation for real-time spectroscopy,” Nature Photonics, vol. 2, no. 1, p. 48, 2008.

[50] A. Mahjoubfar, D. V. Churkin, S. Barland, N. Broderick, S. K. Turitsyn, and B. Jalali, “Time stretch and its applications,” Nature Photonics, vol. 11, no. 6, p. 341, 2017.

[51] R. S. Bennink, S. J. Bentley, and R. W. Boyd, ““two-photon” coincidence imaging with a classical source,” Physical Review Letters, vol. 89, p. 113601, 2002.

[52] Y. Cai and S.-Y. Zhu, “Ghost imaging with incoherent and partially coherent light radiation,” Physical Review E, vol. 71, p. 056607, 2005.

[53] T. Shirai, T. Setälä, and A. T. Friberg, “Ghost imaging of phase objects with classical incoherent light,” Physical Review A, vol. 84, p. 041801, Oct 2011.

[54] M. Fleming and A. Mooradian, “Spectral characteristics of external-cavity controlled semiconductor lasers,” IEEE Journal of Quantum Electronics, vol. 17, no. 1, pp. 44–59, 1981.

[55] K. Harvey and C. Myatt, “External-cavity diode laser using a grazing-incidence diffraction grating,” Optics Letters, vol. 16, no. 12, pp. 910–912, 1991.

[56] M. Planck, The Theory of Heat Radiation, trans. Morton Masius (from the 2nd German ed), 1914.

[57] P. Miles, “Gas discharge lamp,” May 4 1948, US Patent 2,440,832.

[58] A. Bogaerts, E. Neyts, R. Gijbels, and J. van der Mullen, “Gas discharge plasmas and their applications,” Spectrochimica Acta Part B: Atomic Spectroscopy, vol. 57, no. 4, pp. 609–658, 2002.

[59] K. C. Cossel, E. M. Waxman, I. A. Finneran, G. A. Blake, J. Ye, and N. R. Newbury, “Gas-phase broadband spectroscopy using active sources: progress, status, and applications,” Journal of the Optical Society of America B, vol. 34, no. 1, pp. 104–129, 2017.

[60] C. Hamp and D. Mitchell, “Low power lighting system with led illumination,” Oct. 25 2001, US Patent App. 09/803,580.

[61] L. Goldberg and D. Mehuys, “High power superluminescent diode source,” Electronics Letters, vol. 30, no. 20, pp. 1682–1684, 1994.

[62] J. A. Giordmaine and R. C. Miller, “Tunable coherent parametric oscillation in linbo$_3$ at optical frequencies,” Physical Review Letters, vol. 14, pp. 973–976, 1965.

[63] S. Akhmanov, A. Kovrigin, A. Piskarskas, V. Fadeev, and R. Khokhlov, “Observation of parametric amplification in the optical range,” JETP Letters, vol. 2, no. 7, p. 191, 1965.

[64] Y. R. Shen, The principles of nonlinear optics. Wiley-Interscience, 1984.

[65] A. Fiore, V. Berger, E. Rosencher, P. Bravetti, and J. Nagle, “Phase matching using an isotropic nonlinear optical material,” Nature, vol. 391, no. 6666, p. 463, 1998.

[66] R. W. Boyd, Nonlinear Optics (third edition). Academic Press, 2008.

[67] C. Chen, Z. Xu, D. Deng, J. Zhang, G. K. Wong, B. Wu, N. Ye, and D. Tang, "The vacuum ultraviolet phase-matching characteristics of nonlinear optical $KBe_2BO_3F_2$ crystal," Applied physics letters, vol. 68, no. 21, pp. 2930–2932, 1996.

[68] C. Chen, Y. Wu, A. Jiang, B. Wu, G. You, R. Li, and S. Lin, "New nonlinear-optical crystal: LiB_3O_5," Journal of the Optical Society of America B, vol. 6, no. 4, pp. 616–621, 1989.

[69] G. Boyd, H. Kasper, and J. McFee, "Linear and nonlinear optical properties of $LiInS_2$," Journal of Applied Physics, vol. 44, no. 6, pp. 2809–2812, 1973.

[70] P. Del'Haye, A. Schliesser, O. Arcizet, T. Wilken, R. Holzwarth, and T. J. Kippenberg, "Optical frequency comb generation from a monolithic microresonator," Nature, vol. 450, no. 7173, p. 1214, 2007.

[71] R. Henriet, G. Lin, A. Coillet, M. Jacquot, L. Furfaro, L. Larger, and Y. K. Chembo, "Kerr optical frequency comb generation in strontium fluoride whispering-gallery mode resonators with billion quality factor," Optics Letters, vol. 40, no. 7, pp. 1567–1570, 2015.

[72] Y. K. Chembo and N. Yu, "Modal expansion approach to optical-frequency-comb generation with monolithic whispering-gallery-mode resonators," Physical Review A, vol. 82, no. 3, p. 033801, 2010.

[73] Y. Okawachi, K. Saha, J. S. Levy, Y. H. Wen, M. Lipson, and A. L. Gaeta, "Octave-spanning frequency comb generation in a silicon nitride chip," Optics Letters, vol. 36, no. 17, pp. 3398–3400, 2011.

[74] S. Gee, F. Quinlan, S. Ozharar, and P. Delfyett, "Simultaneous optical comb frequency stabilization and super-mode noise suppression of harmonically mode-locked semiconductor ring laser using an intracavity etalon," IEEE Photonics Technology Letters, vol. 17, no. 1, pp. 199–201, 2005.

[75] T. Udem, R. Holzwarth, and T. W. Hänsch, "Optical frequency metrology," Nature, vol. 416, no. 6877, p. 233, 2002.

[76] A. Cingöz, D. C. Yost, T. K. Allison, A. Ruehl, M. E. Fermann, I. Hartl, and J. Ye, "Direct frequency comb spectroscopy in the extreme ultraviolet," Nature, vol. 482, no. 7383, p. 68, 2012.

[77] B. Bernhardt, A. Ozawa, P. Jacquet, M. Jacquey, Y. Kobayashi, T. Udem, R. Holzwarth, G. Guelachvili, T. W. Hänsch, and N. Picqué, "Cavity-enhanced dual-comb spectroscopy," Nature Photonics, vol. 4, no. 1, p. 55, 2010.

[78] F. Adler, M. J. Thorpe, K. C. Cossel, and J. Ye, "Cavity-enhanced direct frequency comb spectroscopy: technology and applications," Annual Review of Analytical Chemistry, vol. 3, pp. 175–205, 2010.

[79] R. R. Alfano, The supercontinuum laser source. Springer, 1989.

[80] J. M. Dudley and J. R. Taylor, Supercontinuum generation in optical fibers. Cambridge University Press, 2010.

[81] R. R. Alfano and S. L. Shapiro, "Observation of self-phase modulation and small-scale filaments in crystals and glasses," Physical Review Letters, vol. 24, pp. 592–594, 1970.

[82] R. Alfano and S. Shapiro, "Emission in the region 4000 to 7000 å via four-photon coupling in glass," Physical Review Letters, vol. 24, no. 11, p. 584, 1970.

[83] J. I. Gersten, R. Alfano, and M. Belic, "Combined stimulated raman scattering and continuum self-phase modulations," Physical Review A, vol. 21, no. 4, p. 1222, 1980.

[84] C. Lin and R. Stolen, "New nanosecond continuum for excited-state spectroscopy," Applied Physics Letters, vol. 28, no. 4, pp. 216–218, 1976.

[85] D. E. Spence, P. N. Kean, and W. Sibbett, "60-fsec pulse generation from a self-mode-locked ti: sapphire laser," Optics Letters, vol. 16, no. 1, pp. 42–44, 1991.

[86] M. T. Asaki, C.-P. Huang, D. Garvey, J. Zhou, H. C. Kapteyn, and M. M. Murnane, "Generation of 11-fs pulses from a self-mode-locked ti: sapphire laser," Optics Letters, vol. 18, no. 12, pp. 977–979, 1993.

[87] J. C. Knight, T. A. Birks, P. S. J. Russell, and D. M. Atkin, "All-silica single-mode optical fiber with photonic crystal cladding," Optics Letters, vol. 21, no. 19, pp. 1547–1549, 1996.

[88] J. K. Ranka, R. S. Windeler, and A. J. Stentz, "Visible continuum generation in air–silica microstructure optical fibers with anomalous dispersion at 800 nm," Optics Letters, vol. 25, no. 1, pp. 25–27, 2000.

[89] J. M. Dudley and G. Genty, "Supercontinuum light," Physics today, vol. 66, pp. 29–34, 2013.

[90] J. M. Dudley, G. Genty, and S. Coen, "Supercontinuum generation in photonic crystal fiber," Reviews of Modern Physics, vol. 78, pp. 1135–1184, 2006.

[91] G. Genty, S. Coen, and J. M. Dudley, "Fiber supercontinuum sources (invited)," Journal of the Optical Society of America B, vol. 24, no. 8, pp. 1771–1785, 2007.

[92] G. P. Agrawal, Nonlinear fiber optics. Academic press, 2007.

[93] S. Coen, A. H. L. Chau, R. Leonhardt, J. D. Harvey, J. C. Knight, W. J. Wadsworth, and P. S. J. Russell, "Supercontinuum generation by stimulated raman scattering and parametric four-wave mixing in photonic crystal fibers," Journal of the Optical Society of America B, vol. 19, no. 4, pp. 753–764, 2002.

[94] C. Xia, M. Kumar, O. P. Kulkarni, M. N. Islam, F. L. Terry Jr, M. J. Freeman, M. Poulain, and G. Mazé, "Mid-infrared supercontinuum generation to 4.5 μm in ZBLAN fluoride fibers by nanosecond diode pumping," Optics Letters, vol. 31, no. 17, pp. 2553–2555, 2006.

[95] J. Herrmann, U. Griebner, N. Zhavoronkov, A. Husakou, D. Nickel, J. Knight, W. Wadsworth, P. S. J. Russell, and G. Korn, "Experimental evidence for supercontinuum generation by fission of higher-order solitons in photonic fibers," Physical Review Letters, vol. 88, no. 17, p. 173901, 2002.

[96] A. O'Keefe and D. A. Deacon, "Cavity ring-down optical spectrometer for absorption measurements using pulsed laser sources," Review of Scientific Instruments, vol. 59, no. 12, pp. 2544–2551, 1988.

[97] D. A. Long, A. J. Fleisher, Q. Liu, and J. T. Hodges, "Ultra-sensitive cavity ring-down spectroscopy in the mid-infrared spectral region," Optics Letters, vol. 41, no. 7, pp. 1612–1615, 2016.

[98] S. E. Fiedler, A. Hese, and A. A. Ruth, "Incoherent broad-band cavity-enhanced absorption spectroscopy," Chemical Physics letters, vol. 371, no. 3, pp. 284–294, 2003.

[99] S. M. Ball, J. M. Langridge, and R. L. Jones, “Broadband cavity enhanced absorption spectroscopy using light emitting diodes,” Chemical Physics Letters, vol. 398, no. 1–3, pp. 68–74, 2004.

[100] J. M. Langridge, T. Laurila, R. S. Watt, R. L. Jones, C. F. Kaminski, and J. Hult, “Cavity enhanced absorption spectroscopy of multiple trace gas species using a supercontinuum radiation source,” Optics Express, vol. 16, no. 14, pp. 10 178–10 188, 2008.

[101] W. Ye, C. Li, C. Zheng, N. P. Sanchez, A. K. Gluszek, A. J. Hudzikowski, L. Dong, R. J. Griffin, and F. K. Tittel, “Mid-infrared dual-gas sensor for simultaneous detection of methane and ethane using a single continuous-wave interband cascade laser,” Optics Express, vol. 24, no. 15, pp. 16 973–16 985, 2016.

[102] D. Richter, D. Lancaster, R. Curl, W. Neu, and F. Tittel, “Compact mid-infrared trace gas sensor based on difference-frequency generation of two diode lasers in periodically poled LiNbO3,” Applied Physics B, vol. 67, no. 3, pp. 347–350, 1998.

[103] I. Armstrong, W. Johnstone, K. Duffin, M. Lengden, A. L. Chakraborty, and K. Ruxton, “Detection of CH_4 in the mid-ir using difference frequency generation with tunable diode laser spectroscopy,” Journal of Lightwave Technology, vol. 28, no. 10, pp. 1435–1442, 2010.

[104] O. Mouawad, P. Béjot, F. Billard, P. Mathey, B. Kibler, F. Désévédavy, G. Gadret, J.-C. Jules, O. Faucher, and F. Smektala, “Filament-induced visible-to-mid-IR supercontinuum in a ZnSe crystal: Towards multi-octave supercontinuum absorption spectroscopy,” Optical Materials, vol. 60, pp. 355 – 358, 2016.

[105] W. Chen, G. Mouret, D. Boucher, and F. Tittel, “Mid-infrared trace gas detection using continuous-wave difference frequency generation in periodically poled $RbTiOAsO_4$,” Applied Physics B, vol. 72, no. 7, pp. 873–876, 2001.

[106] I. Kubat, C. S. Agger, P. M. Moselund, and O. Bang, “Mid-infrared supercontinuum generation to 4.5 µm in uniform and tapered ZBLAN step-index fibers by direct pumping at 1064 or 1550 nm,” Journal of the Optical Society of America B, vol. 30, no. 10, pp. 2743–2757, 2013.

[107] U. Platt, J. Meinen, D. Pöhler, and T. Leisner, "Broadband cavity enhanced differential optical absorption spectroscopy (CE-DOAS)–applicability and corrections," Atmospheric Measurement Techniques, vol. 2, no. 2, pp. 713–723, 2009.

[108] L. Rothman, I. Gordon, Y. Babikov, A. Barbe, D. Chris Benner, P. Bernath, M. Birk, L. Bizzocchi, V. Boudon, L. Brown, A. Campargue, K. Chance, E. Cohen, L. Coudert, V. Malathy Devi, B. Drouin, A. Fayt, J.-M. Flaud, R. Gamache, and G. Wagner, "The HITRAN2012 molecular spectroscopic database," Journal of Quantitative Spectroscopy and Radiative Transfer, vol. 130, pp. 4–50, 2013.

[109] D. Hoch, J. Buxmann, H. Sihler, D. Pöhler, C. Zetzsch, and U. Platt, "An instrument for measurements of bro with led-based cavity-enhanced differential optical absorption spectroscopy," Atmospheric Measurement Techniques, vol. 7, no. 1, pp. 199–214, 2014.

[110] X. Jiang, N. Y. Joly, M. A. Finger, F. Babic, G. K. Wong, J. C. Travers, and P. S. J. Russell, "Deep-ultraviolet to mid-infrared supercontinuum generated in solid-core ZBLAN photonic crystal fibre," Nature Photonics, vol. 9, no. 2, pp. 133–139, 2015.

[111] P. Domachuk, N. Wolchover, M. Cronin-Golomb, A. Wang, A. K. George, C. Cordeiro, J. C. Knight, and F. Omenetto, "Over 4000 nm bandwidth of mid-IR supercontinuum generation in sub-centimeter segments of highly nonlinear tellurite PCFs," Optics Express, vol. 16, no. 10, pp. 7161–7168, 2008.

[112] L. Wetenkamp, G. West, and H. Többen, "Optical properties of rare earth-doped zblan glasses," Journal of non-crystalline solids, vol. 140, pp. 35–40, 1992.

[113] P. A. Remillard and M. C. Amorelli, "Lock-in amplifier," May 11 1993, US Patent 5,210,484.

[114] E. W. Weisstein, Least squares fitting. Wolfram Research, Inc., 2002.

[115] A. G. Bell, "Art. xxxiv.–on the production and reproduction of sound by light," American Journal of Science (1880-1910), vol. 20, no. 118, p. 305, 1880.

[116] P. R. Griffiths and J. A. De Haseth, Fourier transform infrared spectrometry. John Wiley & Sons, 2007, vol. 171.

[117] A. Paritsky and A. Kots, "Fiber optic microphone as a realization of fiber optic positioning sensors," Proceedings SPIE, vol. 3110, pp. 3110 – 3110 – 7, 1997.

[118] V. Koskinen, J. Fonsen, J. Kauppinen, and I. Kauppinen, "Extremely sensitive trace gas analysis with modern photoacoustic spectroscopy," Vibrational Spectroscopy, vol. 42, no. 2, pp. 239–242, 2006.

[119] W. Demtröder, Laser Spectroscopy: Basic Concepts and Instrumentation, ser. Advanced Texts in Physics. Springer Berlin Heidelberg, 2002.

[120] C. B. Hirschmann, Cantilever-enhanced Photoacoustic Spectroscopy in the Analysis of Volatile Organic Compounds. VTT, 2013.

[121] A. A. Kosterev, Y. A. Bakhirkin, R. F. Curl, and F. K. Tittel, "Quartz-enhanced photoacoustic spectroscopy," Optics Letters, vol. 27, no. 21, pp. 1902–1904, 2002.

[122] A. Kosterev, Y. Bakhirkin, and F. Tittel, "Ultrasensitive gas detection by quartz-enhanced photoacoustic spectroscopy in the fundamental molecular absorption bands region," Applied Physics B, vol. 80, no. 1, pp. 133–138, 2005.

[123] A. A. Kosterev and F. K. Tittel, "Ammonia detection by use of quartz-enhanced photoacoustic spectroscopy with a near-ir telecommunication diode laser," Applied Optics, vol. 43, no. 33, pp. 6213–6217, 2004.

[124] J.-J. Greffet, R. Carminati, K. Joulain, J.-P. Mulet, S. Mainguy, and Y. Chen, "Coherent emission of light by thermal sources," Nature, vol. 416, no. 6876, p. 61, 2002.

[125] J. Kauppinen, K. Wilcken, I. Kauppinen, and V. Koskinen, "High sensitivity in gas analysis with photoacoustic detection," Microchemical Journal, vol. 76, no. 1-2, pp. 151–159, 2004.

[126] J. Peltola, M. Vainio, T. Hieta, J. Uotila, S. Sinisalo, M. Metsälä, M. Siltanen, and L. Halonen, "High sensitivity trace gas detection by cantilever-enhanced photoacoustic spectroscopy using a mid-infrared continuous-wave optical parametric oscillator," Optics Express, vol. 21, no. 8, pp. 10 240–10 250, 2013.

[127] C. B. Hirschmann, J. Lehtinen, J. Uotila, S. Ojala, and R. L. Keiski, "Sub-ppb detection of formaldehyde with cantilever enhanced photoacoustic spectroscopy using quantum cascade laser source," Applied Physics B, vol. 111, no. 4, pp. 603–610, 2013.

[128] T. Tomberg, M. Vainio, T. Hieta, and L. Halonen, “Sub-parts-per-trillion level sensitivity in trace gas detection by cantilever-enhanced photo-acoustic spectroscopy,” Scientific Reports, vol. 8, no. 1, p. 1848, 2018.

[129] T. Laurila, H. Cattaneo, V. Koskinen, J. Kauppinen, and R. Hernberg, “Diode laser-based photoacoustic spectroscopy with interferometrically-enhanced cantilever detection,” Optics Express, vol. 13, no. 7, pp. 2453–2458, 2005.

[130] T. Pittman, Y. Shih, D. Strekalov, and A. Sergienko, “Optical imaging by means of two-photon quantum entanglement,” Physical Review A, vol. 52, no. 5, p. R3429, 1995.

[131] D. Strekalov, A. Sergienko, D. Klyshko, and Y. Shih, “Observation of two-photon “ghost” interference and diffraction,” Physical Review Letters, vol. 74, no. 18, p. 3600, 1995.

[132] R. S. Bennink, S. J. Bentley, R. W. Boyd, and J. C. Howell, “Quantum and classical coincidence imaging,” Physical Review Letters, vol. 92, p. 033601, 2004.

[133] B. Sun, M. P. Edgar, R. Bowman, L. E. Vittert, S. Welsh, A. Bowman, and M. J. Padgett, “3D computational imaging with single-pixel detectors,” Science, vol. 340, no. 6134, pp. 844–847, 2013.

[134] B. I. Erkmen and J. H. Shapiro, “Ghost imaging: from quantum to classical to computational,” Advances in Optics and Photonics, vol. 2, no. 4, pp. 405–450, 2010.

[135] M. J. Padgett and R. W. Boyd, “An introduction to ghost imaging: quantum and classical,” Philosophical Transactions of the Royal Society A, vol. 375, no. 2099, p. 20160233, 2017.

[136] K. W. C. Chan, M. N. O’Sullivan, and R. W. Boyd, “Two-color ghost imaging,” Physical Review A, vol. 79, p. 033808, 2009.

[137] F. Ferri, D. Magatti, L. A. Lugiato, and A. Gatti, “Differential ghost imaging,” Physical Review Letters, vol. 104, p. 253603, 2010.

[138] Y. Bromberg, O. Katz, and Y. Silberberg, “Ghost imaging with a single detector,” Physical Review A, vol. 79, no. 5, p. 053840, 2009.

[139] J. H. Shapiro, “Computational ghost imaging,” Physical Review A, vol. 78, no. 6, p. 061802, 2008.

[140] P. Clemente, V. Durán, E. Tajahuerce, and J. Lancis, “Optical encryption based on computational ghost imaging,” Optics Letters, vol. 35, no. 14, pp. 2391–2393, 2010.

[141] O. Katz, Y. Bromberg, and Y. Silberberg, “Compressive ghost imaging,” Applied Physics Letters, vol. 95, no. 13, p. 131110, 2009.

[142] P. Ryczkowski, M. Barbier, A. T. Friberg, J. M. Dudley, and G. Genty, “Magnified time-domain ghost imaging,” Applied Physics Letters Photonics, vol. 2, no. 4, p. 046102, 2017.

[143] D. Faccio, “Optical communications: Temporal ghost imaging,” Nature Photonics, vol. 10, no. 3, p. 150, 2016.

[144] P. Janassek, S. Blumenstein, and W. Elsäßer, “Recovering a hidden polarization by ghost polarimetry,” Optics Letters, vol. 43, no. 4, pp. 883–886, 2018.

[145] R. E. Meyers, K. S. Deacon, and Y. Shih, “Turbulence-free ghost imaging,” Applied Physics Letters, vol. 98, no. 11, p. 111115, 2011.

[146] B. I. Erkmen, “Computational ghost imaging for remote sensing applications,” Interplanetary Network Progress Reports, vol. 42, no. 185, pp. 1–23, 2011.

[147] R. Meyers, K. S. Deacon, and Y. Shih, “Ghost-imaging experiment by measuring reflected photons,” Physical Review A, vol. 77, no. 4, p. 041801, 2008.

[148] Y. Cai and S.-Y. Zhu, “Ghost imaging with incoherent and partially coherent light radiation,” Physical Review E, vol. 71, no. 5, p. 056607, 2005.

[149] Y. Bai and S. Han, “Ghost imaging with thermal light by third-order correlation,” Physical Review A, vol. 76, no. 4, p. 043828, 2007.

[150] D. M. Nguyen, T. Godin, S. Toenger, Y. Combes, B. Wetzel, T. Sylvestre, J.-M. Merolla, L. Larger, G. Genty, and F. Dias, “Incoherent resonant seeding of modulation instability in optical fiber,” Optics Letters, vol. 38, no. 24, pp. 5338–5341, 2013.

[151] B. I. Erkmen and J. H. Shapiro, “Signal-to-noise ratio of gaussian-state ghost imaging,” Physical Review A, vol. 79, no. 2, p. 023833, 2009.

[152] H. E. Soper, “Truston the probable error of the correlation coefficient to a second approximation,” Biometrika, vol. 9, no. 1/2, pp. 91–115, 1913.

[153] J. M. Schmitt, “Optical coherence tomography (OCT): a review,” IEEE Journal of Selected Topics in Quantum Electronics, vol. 5, no. 4, pp. 1205–1215, July 1999.

[154] P. Ryczkowski, Novel interferometric and correlation optical imaging techniques. Tampere University of Technology, 2016.

[155] C. O’Mahony, M. Hill, M. Brunet, R. Duane, and A. Mathewson, “Characterization of micromechanical structures using white-light interferometry,” Measurement Science and Technology, vol. 14, no. 10, p. 1807, 2003.

[156] W. B. Ribbens, “Interferometric surface roughness measurement,” Applied Optics, vol. 8, no. 11, pp. 2173–2176, 1969.

[157] P. Ryczkowski, J. Turunen, A. T. Friberg, and G. Genty, “Experimental demonstration of spectral intensity optical coherence tomography,” Scientific Reports, vol. 6, p. 22126, 02 2016.

[158] R. Leitgeb, C. K. Hitzenberger, and A. F. Fercher, “Performance of fourier domain vs. time domain optical coherence tomography,” Optics Express, vol. 11, no. 8, pp. 889–894, 2003.

[159] M. A. Choma, M. V. Sarunic, C. Yang, and J. A. Izatt, “Sensitivity advantage of swept source and fourier domain optical coherence tomography,” Optics Express, vol. 11, no. 18, pp. 2183–2189, 2003.

[160] J. F. De Boer, B. Cense, B. H. Park, M. C. Pierce, G. J. Tearney, and B. E. Bouma, “Improved signal-to-noise ratio in spectral-domain compared with time-domain optical coherence tomography,” Optics Letters, vol. 28, no. 21, pp. 2067–2069, 2003.

[161] M. Adhi and J. S. Duker, “Optical coherence tomography–current and future applications,” Current opinion in ophthalmology, vol. 24, no. 3, p. 213, 2013.

[162] T. Shirai and A. T. Friberg, “Resolution improvement in spectral-domain optical coherence tomography based on classical intensity correlations,” Optics Letters, vol. 38, no. 2, pp. 115–117, 2013.

ORIGINAL PUBLICATIONS

I

CAVITY ENHANCED ABSORPTION SPECTROSCOPY IN THE MID-INFRARED USING A SUPERCONTINUUM SOURCE

by
Caroline Amiot, Antti Aalto, Piotr Ryczkowski, Juha Toivonen & Goëry Genty,
July 2017
Applied Physics Letters, vol 111, no. 6, p, 061103
Reproduced with kind of permission from AIP Publishing.

APPLIED PHYSICS LETTERS **111**, 061103 (2017)

Cavity enhanced absorption spectroscopy in the mid-infrared using a supercontinuum source

Caroline Amiot,[1,2,a)] Antti Aalto,[1] Piotr Ryczkowski,[1] Juha Toivonen,[1] and Goëry Genty[1]
[1]*Optics Laboratory, Physics Department, Tampere University of Technology, P.O. Box 692, FI-33101 Tampere, Finland*
[2]*Institut FEMTO-ST, UMR 6174 CNRS-Université Bourgogne Franche-Comté, 15B avenue des Montboucons, 25030 Besançon Cedex, France*

(Received 29 May 2017; accepted 23 July 2017; published online 8 August 2017)

We demonstrate incoherent broadband cavity enhanced absorption spectroscopy in the mid-infrared wavelength range from 3000 to 3450 nm using an all-fiber based supercontinuum source. Multi-component gas detection is performed, and the concentrations of acetylene and methane are retrieved with sub-ppm accuracy. A linear response to nominal gas concentrations is observed, demonstrating the feasibility of the method for sensing applications. *Published by AIP Publishing.* [http://dx.doi.org/10.1063/1.4985263]

Gas detection and accurate concentration measurements are important in many fields ranging from the industrial process to emission control and pollution monitoring. Different spectroscopic methods have been developed to retrieve gas concentrations with very high accuracy, including cavity ring down spectroscopy[1,2] and its broadband implementation,[3] integrated cavity output spectroscopy,[4] noise-immune cavity-enhanced optical-heterodyne molecular spectroscopy,[5] and cavity enhanced absorption spectroscopy (CEAS).[6,7] Each of these methods presents advantages and drawbacks in terms of sensitivity, selectivity, footprint, and cost.

Cavity enhanced absorption spectroscopy is conceptually relatively simple, and a robust experimental setup can be implemented from off-the-shelf components. In CEAS, one uses a highly reflective cavity to increase significantly the optical path and thus the interaction length between the light beam and gas molecules, which leads to enhanced sensitivity. However, because of the mirrors' highly reflectivity, the light intensity at the cavity output is dramatically reduced such that a detector with high sensitivity is generally required to measure the absorption. CEAS can be selective for a particular gas absorption line if a source with a narrow linewidth is used, or it can also perform multi-component detection when a light source with a broad spectrum is employed.

The recent development of light sources operating in the mid-infrared has recently allowed to extend precise spectroscopic measurements to the molecular fingerprint region where many gases possess strong absorption lines, and indeed, several studies have reported measurements from pure gas in the 3–5 μm region.[8–12] All these recent studies used optical parametric oscillators based on difference-frequency generation or a quantum cascade laser. While some of the recent demonstrations allow for extreme sensitivity, the light source is single species specific, which may limit the usability. The development of broadband supercontinuum sources[13] on the other hand has revolutionized many applications ranging from frequency metrology to imaging and spectroscopy. Recently, supercontinuum (SC) has been shown to be particularly adapted to perform broadband CEAS in the near infrared.[14,15]

Here, taking advantage of the high spatial coherence and high brightness of this type of source, we demonstrate multi-components gas detection in the mid-infrared over a bandwidth as large as 450 nm using incoherent broadband cavity enhanced absorption spectroscopy. These results are significant not only because they illustrate the potential of incoherent supercontinuum sources for spectroscopy in the mid-IR but also because they represent the largest continuous detection window for gas reported using the CEAS method.

An all-fiber supercontinuum source with a spectrum spanning from 900 to 3700 nm was developed using a 1547 nm gain-switched pump laser producing 10 kW peak power sub-nanosecond pulses at a repetition rate of 100 kHz. The pulses are first injected into the anomalous dispersion regime of a 4 m long step-index, silica non-zero dispersion shifted fiber (DSF) with 9 μm core-diameter. The zero dispersion wavelength (ZDW) of the fiber is at 1510 nm, allowing for efficient noise-seeded modulation instability dynamics which breaks up the long pump pulses into a large number of solitons with a short duration.[16] The solitons experience the Raman self-frequency shift which expands the spectrum towards the long wavelengths up to 2400 nm, which is the transparency window limit of silica. The output of the DSF is then directly connected to a 7-m step-index fluoride (ZBLAN) fiber with low attenuation (<0.1 dB/m) up to c.a. 4 μm. The core size of the ZBLAN fiber is comparable to that of the DSF, which minimizes the coupling losses. Because a significant fraction of the spectral intensity after the DSF is located in the anomalous dispersion regime of the ZBLAN ($\mathrm{ZDW}_{\mathrm{ZBLAN}} = 1620$ nm), the short solitons undergo additional Raman self-frequency shift extending the supercontinuum spectrum up to 3700 nm with an average output power of 160 mW. The resulting SC spectrum illustrated in Fig. 1 is essentially spectrally incoherent with large fluctuations from pulse to pulse. Yet, the average spectrum is highly stable, a pre-requisite in the context of spectroscopic measurements.

[a)] caroline.amiot@tut.fi

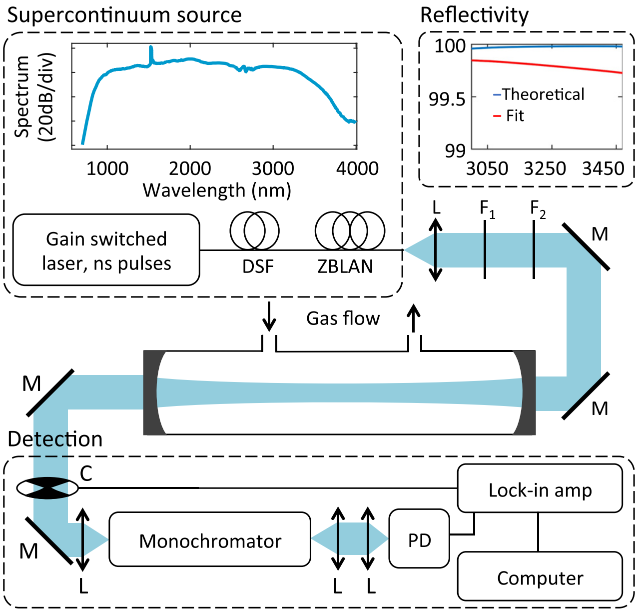

FIG. 1. Experimental setup. DSF: dispersion-shifted fiber, ZBLAN: fluoride fiber, L: lens, $F_{1/2}$: filter, M: mirror, C: mechanical chopper, and PD: photodetector. The top part of the figure shows the measured SC spectrum at the ZBLAN fiber output. The inset to the right compares the modelled mirrors reflectivity as provided by the manufacturer (blue line) with the fitted reflectivity from the experimental measurements (red line).

The all-fiber SC source was subsequently used to perform cavity-enhanced absorption spectroscopy measurements. The experimental setup is illustrated in Fig. 1. The SC beam is collimated to a 3 mm size using an aspheric lens coated for the 3–5 μm range. The beam propagates through a 1-m long confocal cavity constructed from an aluminium pipe and closed by two mirrors with 1 m radius of curvature and a high reflection coefficient ($R > 99.95$) between 3000 and 3450 nm. The SC power corresponding to the cavity spectral bandwidth is 4 mW. The high reflectivity of the mirrors results in a transmission of 2.5×10^{-4} and an effective path length of c.a. 300 m. In order to match the supercontinuum source spectrum with the spectral bandwidth of the cavity, the short wavelength components of the SC are filtered out using two long-pass filters F_1 and F_2 with cut-off wavelengths at 2333 nm and 2998 nm, respectively. The cavity has valves in both ends, allowing gas circulation with a constant flow during the measurements. Gas samples were diluted from 0.5 ppm of C_2H_2 and 0.25 ppm of CH_4 in nitrogen using mass flow controllers (5850S, Brooks Instrument). Using an uncoated MgF_2 lens with a focal length of 50 mm, the beam at the cavity output is focused onto the entrance slit of a computer-controlled monochromator (HR550 Horiba) with 300 grooves/mm grating, and the light intensity is detected with a liquid nitrogen-cooled InAs photodetector (Judson J10D). Wavelength scanning is performed in steps of 0.5 nm. Because only a small fraction of the 4 mW SC power is transmitted through the highly reflective cavity, we use lock-in detection (Lock-in amplifier + mechanical chopper at 245 kHz) and an integration time of 1 s to improve the signal-to-noise ratio.

We next perform measurements of different gases using the differential optical absorption spectroscopy (DOAS) method performed in sequential steps.[15] The spectral transmission of the cavity is first calibrated by a reference measurement with only N_2 flowing through the cavity such that no absorption is present. A second measurement is subsequently performed with the gas under study, and the spectral transmission from the cavity is then compared to that of the reference measurement

$$\frac{I(\lambda)}{I_0(\lambda)} = \frac{\rho(\lambda)}{\rho(\lambda)+\tau(\lambda)}, \tag{1}$$

where $I(\lambda)$ and $I_0(\lambda)$ correspond to the spectral intensities recorded for the gas under study and N_2 in the cavity, respectively. The parameter ρ represents the mirror spectral losses, and τ is the small single-pass absorption through the cavity of length d_0 and depends on the absorption cross section $\sigma(\lambda)_j$ and number density N_j of the gas species j present in the cavity as

$$\tau(\lambda) = \sum_j \sigma(\lambda)_j N_j d_0. \tag{2}$$

Retrieval of the gas species concentration is then achieved by fitting the experimentally measured ratio $I(\lambda)/I_0(\lambda)$ with Eqs. (1) and (2) using a least-square method. In the fitting procedure, we use the HITRAN 2012 database for absorption line strengths and apply the appropriate Voigt broadening of the lines at the measurement temperature and pressure. The model also accounts for the finite resolution of the monochromator and slit width, as well as for possible background drift caused, e.g., by light intensity or cavity coupling fluctuations during the measurement.[15]

One particular feature of broadband DOAS is its ability to retrieve accurately gas concentrations even when the signal-to-noise ratio is relatively low and the recorded absorption spectra are noisy. This arises from the fact that spectral fitting is performed over a large number of absorption lines, which effectively increases the integration time and thus reduces the noise.

The experimental setup is first calibrated by measuring the spectrum of a reference gas sample of known concentration, using only the monochromator resolution and mirror losses as free-running parameters. This allows us to determine precisely the spectral dependence of the mirrors' losses $\rho(\lambda)$, which slightly differs from the simulated data based on the mirrors' layer structure and provided by the manufacturer (see the inset in Fig. 1). Figure 2 shows the comparison between the fitted and measured absorption lines of acetylene [Fig. 2(a)] and methane [Fig. 2(b)] for nominal concentrations of 4 ppm and 5 ppm, respectively, and we can see excellent agreement between the DOAS measurement and the fit. The actual measurement resolution was found to be 1 nm, which is in agreement with the targeted resolution using the monochromator slits of 100 μm.

The calibrated instrument is then used to determine the response of the method by repeating the measurement for different gas concentrations and using the concentration as a free-running parameter in the fitting procedure. Figure 3 shows the results of the fit against the nominal gas concentrations set using the mass flow controllers. Linear responses

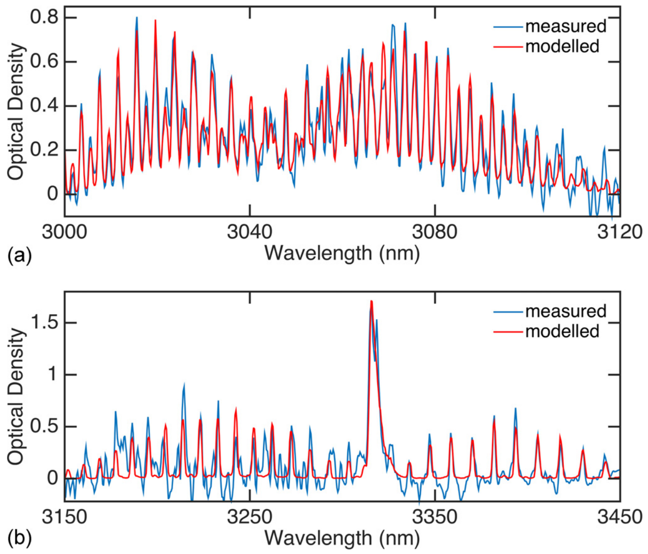

FIG. 2. Comparison between the modelled (red line) and the measured (blue line) absorption spectra of 5 ppm of acetylene (from 3000 to 3100 nm) and 4 ppm of methane (from 3150 to 3450 nm). Note that negative values in the measured optical density result from the detection noise.

are found for both gases, demonstrating the feasibility of the method for sensing applications. The smallest concentrations of 0.5 ppm for acetylene and 0.25 ppm for methane are still following the linear response function.

One major advantage of CEAS over other spectroscopic techniques is the possibility to perform detection over a very broad bandwidth. We next exploited this potential to demonstrate multi-component gas analysis over the full bandwidth of the cavity from 3000 to 3450 nm. For this purpose, both methane and acetylene were flown simultaneously through the cavity with nominal concentrations of 5 and 2 ppm, respectively. The results in Fig. 4 show very good agreement between the measured and modelled absorption using the nominal concentrations over the full 450 nm bandwidth. For the modelled absorption, only the low-order polynomial was used as a free running parameter to account for possible drift during the long measurement time. The present experiments have been performed with pure gas samples in a cavity flushed with N_2. From a more practical application viewpoint, it would be desirable to perform similar measurements but in the presence of air, especially because water absorption lines are present in the particular wavelength range used here for the detection. Numerical simulations based on the setup parameters indicate that several absorption lines of acetylene and methane do not overlap with those of water, and thus, it should be possible to retrieve the gas concentrations by taking the water peaks into account in the fitting procedure. Furthermore, enhanced spectral resolution in the detection and reduced pressure in the gas cell would yield better separation of different gas components.

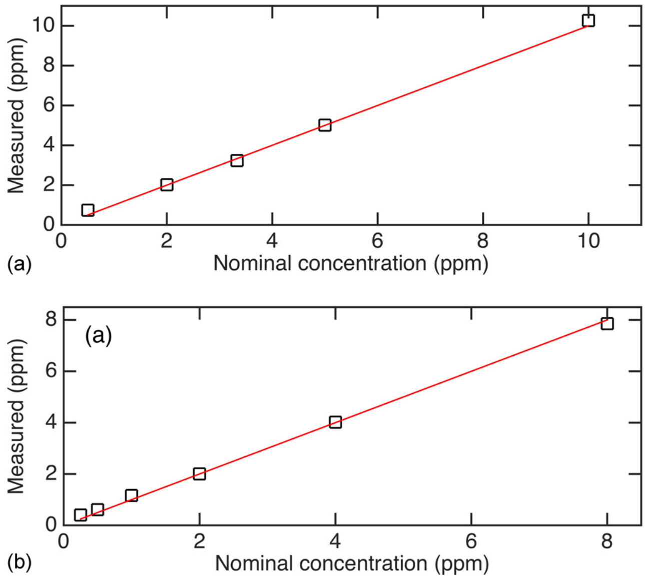

FIG. 3. Measured vs. nominal concentration for (a) acetylene and (b) methane.

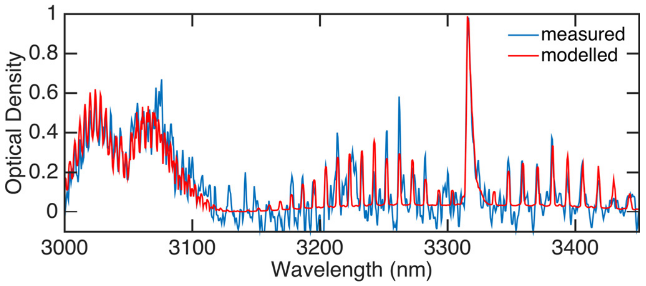

FIG. 4. Simultaneous multi-component detection of 5 ppm of acetylene (from 3000 to 3150 nm) and 2 ppm of methane (from 3150 to 3450 nm). The blue and red lines illustrate the measured and modelled spectra, respectively. Note that negative values in the measured optical density result from the detection noise.

In conclusion, using an all-fiber supercontinuum source, we have demonstrated for the first time CEAS in the mid-infrared over a wavelength range as large as 450 nm, allowing us to retrieve gas concentrations with sub-ppm accuracy. The sensitivity and measurement speed of the technique could be improved in various ways. The intensity of the light source could be increased, e.g., by fusion-splicing the DSF and ZBLAN fibers,[17] which would reduce the connection losses and allow to extend the spectrum further into the mid-infrared with increased power spectral density. Losses resulting from the non-perfect alignment of the cavity mirrors or from the chromatic aberration of the collimating lens could also be reduced with the use of a parabolic mirror. The measurement speed on the other hand is currently limited to 30 nm/min due to the monochromator scanning and long integration time needed to improve the signal-to-noise ratio. This could be significantly reduced by using a spectrometer with a detector array.[18]

This work was supported by the Academy of Finland (Grant No. 298463) and by the European Union Horizon 2020 research and innovation programme under Grant Agreement No. 722380 SUPUVIR. Caroline Amiot also acknowledges the Doctoral School of Tampere University of Technology.

[1] A. O'Keefe and D. A. Deacon, "Cavity ring-down optical spectrometer for absorption measurements using pulsed laser sources," Rev. Sci. Instrum. **59**, 2544–2551 (1988).

[2] D. A. Long, A. J. Fleisher, Q. Liu, and J. T. Hodges, "Ultra-sensitive cavity ring-down spectroscopy in the mid-infrared spectral region," Opt. Lett. **41**, 1612–1615 (2016).

[3] M. J. Thorpe, K. D. Moll, R. J. Jones, B. Safdi, and J. Ye, "Broadband cavity ringdown spectroscopy for sensitive and rapid molecular detection," Science **311**, 1595–1599 (2006).

[4] A. O'Keefe, "Integrated cavity output analysis of ultra-weak absorption," Chem. Phys. Lett. **293**, 331–336 (1998).

[5] J. Ye, L.-S. Ma, and J. L. Hall, "Ultrasensitive detections in atomic and molecular physics: Demonstration in molecular overtone spectroscopy," J. Opt. Soc. Am. B **15**, 6–15 (1998).

[6] R. Engeln, G. Berden, R. Peeters, and G. Meijer, "Cavity enhanced absorption and cavity enhanced magnetic rotation spectroscopy," Rev. Sci. Instrum. **69**, 3763–3769 (1998).

[7] S. E. Fiedler, A. Hese, and A. A. Ruth, "Incoherent broad-band cavity-enhanced absorption spectroscopy," Chem. Phys. Lett. **371**, 284–294 (2003).

[8] W. Ye, C. Li, C. Zheng, N. P. Sanchez, A. K. Gluszek, A. J. Hudzikowski, L. Dong, R. J. Griffin, and F. K. Tittel, "Mid-infrared dual-gas sensor for simultaneous detection of methane and ethane using a single continuous-wave interband cascade laser," Opt. Express **24**, 16973–16985 (2016).

[9] D. Richter, D. Lancaster, R. Curl, W. Neu, and F. Tittel, "Compact mid-infrared trace gas sensor based on difference-frequency generation of two diode lasers in periodically poled $LiNbO_3$," Appl. Phys. B **67**, 347–350 (1998).

[10] I. Armstrong, W. Johnstone, K. Duffin, M. Lengden, A. L. Chakraborty, and K. Ruxton, "Detection of CH_4 in the mid-IR using difference frequency generation with tunable diode laser spectroscopy," J. Lightwave Technol. **28**, 1435–1442 (2010).

[11] O. Mouawad, P. Béjot, F. Billard, P. Mathey, B. Kibler, F. Désévédavy, G. Gadret, J.-C. Jules, O. Faucher, and F. Smektala, "Filament-induced visible-to-mid-IR supercontinuum in a ZnSe crystal: Towards multi-octave supercontinuum absorption spectroscopy," Opt. Mater. **60**, 355–358 (2016).

[12] W. Chen, G. Mouret, D. Boucher, and F. Tittel, "Mid-infrared trace gas detection using continuous-wave difference frequency generation in periodically poled $RbTiOAsO_4$," Appl. Phys. B **72**, 873–876 (2001).

[13] I. Kubat, C. S. Agger, P. M. Moselund, and O. Bang, "Mid-infrared supercontinuum generation to 4.5 μm in uniform and tapered ZBLAN step-index fibers by direct pumping at 1064 or 1550 nm," J. Opt. Soc. Am. B **30**, 2743–2757 (2013).

[14] J. M. Langridge, T. Laurila, R. S. Watt, R. L. Jones, C. F. Kaminski, and J. Hult, "Cavity enhanced absorption spectroscopy of multiple trace gas species using a supercontinuum radiation source," Opt. Express **16**, 10178–10188 (2008).

[15] A. Aalto, G. Genty, T. Laurila, and J. Toivonen, "Incoherent broadband cavity enhanced absorption spectroscopy using supercontinuum and superluminescent diode sources," Opt. Express **23**, 25225–25234 (2015).

[16] J. M. Dudley, G. Genty, and S. Coen, "Supercontinuum generation in photonic crystal fiber," Rev. Mod. Phys. **78**, 1135–1184 (2006).

[17] K. Yin, B. Zhang, J. Yao, L. Yang, S. Chen, and J. Hou, "Highly stable, monolithic, single-mode mid-infrared supercontinuum source based on low-loss fusion spliced silica and fluoride fibers," Opt. Lett. **41**, 946–949 (2016).

[18] H. Kim, E. Plis, J. Rodriguez, G. Bishop, Y. Sharma, L. Dawson, S. Krishna, J. Bundas, R. Cook, D. Burrows *et al.*, "Mid-IR focal plane array based on type-II InAs/GaSb strain layer superlattice detector with nBn design," Appl. Phys. Lett. **92**, 183502 (2008).

II

BROADBAND CANTILEVER-ENHANCED PHOTOACOUSTIC SPECTROSCOPY IN THE MID-INFRARED USING SUPERCONTINUUM

by
Tommi Mikkonen, Caroline Amiot, Antti Aalto, Kim Patokoski, Goëry Genty &
Juha Toivonen, October 2018
Optics Letters, vol 43, no. 20, pp. 5094-5097

Optics Letters

Broadband cantilever-enhanced photoacoustic spectroscopy in the mid-IR using a supercontinuum

Tommi Mikkonen,[1,*] Caroline Amiot,[1,2] Antti Aalto,[1] Kim Patokoski,[1] Goëry Genty,[1] and Juha Toivonen[1]

[1]Laboratory of Photonics, Tampere University of Technology, Tampere, Finland
[2]Institut FEMTO-ST, UMR 6174 CNRS, Université de Bourgogne Franche-Comté, Besançon, France
*Corresponding author: tommi.j.mikkonen@tut.fi

Received 4 July 2018; revised 30 August 2018; accepted 10 September 2018; posted 11 September 2018 (Doc. ID 337787); published 12 October 2018

We demonstrate cantilever-enhanced photoacoustic spectroscopy in the mid-infrared using a supercontinuum source. The approach is broadband and allows for higher photoacoustic signal intensity and an enhanced signal-to-noise ratio as compared to systems employing conventional black body radiation sources. Using this technique, we perform spectroscopic measurements of the full ro-vibrational band structure of water vapor at 1900 nm and methane at 3300 nm with relative signal enhancement factors of 70 and 19, respectively, when compared to measurements that use the black body radiation source. Our results offer a novel perspective for photoacoustic detection opening the door to sensitive broadband analyzers in the mid-infrared spectral region.

OCIS codes: (320.6629) Supercontinuum generation; (060.3735) Fiber Bragg gratings.

https://doi.org/10.1364/OL.43.005094

Photoacoustic spectroscopy (PAS) is an optical sensing technique that detects the pressure wave resulting from local heating and thermal expansion when light is absorbed by a gas sample placed inside an acoustic cell. PAS with high-power lasers is particularly attractive, as the signal detected by a pressure-sensitive detector is directly proportional to the absorbed light power, resulting in highly sensitive background-free measurements. Another significant advantage of PAS is the small volume of gas sample required which makes it generally more compact than, for example, conventional broadband Fourier transform infrared spectrometers (FTIRs) [1]. Microphones with electrical readout are commonly used as detectors in PAS; however, their sensitivity is limited by the electrical noise and resonant acoustic cells are often needed for high sensitivity measurements, which limits the detection to a single modulation frequency. By replacing the microphone with a micromechanical cantilever whose mechanical oscillations are detected with an optical interferometer, acoustic resonance enhancement is not required, either from the cell or from the cantilever, allowing for broadband detection with similar sensitivities [2]. And indeed, sub-parts per trillion sensitivities have been reported using such a cantilever-enhanced photoacoustic spectroscopy approach (CEPAS) [3].

Various types of light sources have been used in laser-based PAS systems, including distributed feedback diode lasers [4,5] and external cavity diode lasers [6] in the near-infrared, or quantum cascade laser [7,8] and optical parametric oscillators [9] in the mid-infrared. These sources are inherently narrowband, or they have a limited wavelength-tuning range. Broadband detection may be achieved using thermal emitters or black body radiators [1,10], but their low brightness limits the sensitivity in this case. Supercontinuum (SC) sources, on the other hand, can exhibit an extremely broad bandwidth with brightness exceeding by orders of magnitude that of thermal emitters, and the unique properties of SC sources have made them ideal light source candidates for many sensing and imaging applications, including spectroscopy, microscopy, or optical coherence tomography [11–15]. In this Letter, combining a broadband supercontinuum source with FTIR CEPAS, we demonstrate sensitive, broadband photoacoustic detection of water vapor and methane in the mid-infrared spectral region. Our results show a significant increase in the signal intensity as compared to using a thermal emitter. A significant advantage of the fiber-based SC source is its high spatial coherence allowing for (1) a much larger power spectral density in the FTIR as compared to blackbody radiators and (2) adjustment of the FTIR beam path and tuning the resolution of the measurement. Our results open up new perspectives for gas sensing and, more generally, spectroscopic applications using broadband photoacoustic detection.

Our experimental setup is shown in Fig. 1. The supercontinuum source is generated by injecting 0.6 ns pulses at 1547 nm from a gain-switched fiber laser (Keopsys-PEFL-K09) with a tunable repetition rate into the anomalous dispersion regime of a 4 m long silica dispersion-shifted fiber (DSF, Corning, Inc. LEAF) followed by an 8 m long fluoride fiber (ZBLAN) as described in Ref. [12]. Here, depending on the gas sample to be characterized, we used a different repetition rate for the pump laser so as to optimize the power spectral density of

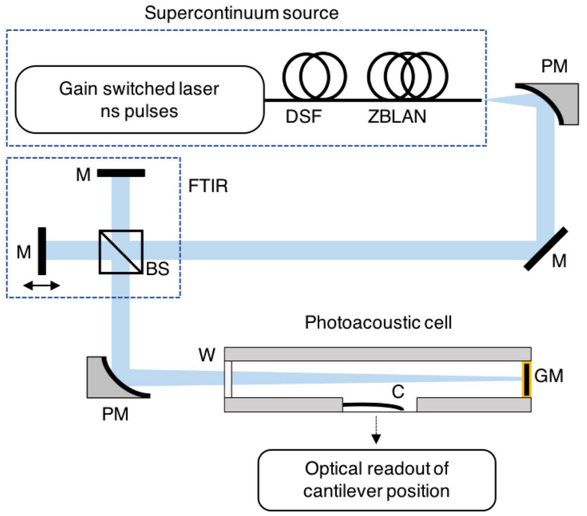

Fig. 1. Experimental setup. PM, off-axis parabolic mirror; M, mirror; BS, beam splitter; W, window; GM, gold mirror; C, cantilever.

the SC in the spectral range of interest. Specifically, for a repetition rate of 70 kHz, the 10 kW peak power of the pump laser pulses leads to the generation of a broadband SC extending from c.a. 1500 nm up to c.a. 3700 nm as the result of multiple cascaded nonlinear dynamics, including modulation instability, soliton formation, and Raman self-frequency shift [16]. When the repetition rate is increased to 400 kHz, the peak power of the pump pulses is reduced to less than 2 kW, and the spectrum extends from 1500 up to 2400 nm. The average SC spectra measured corresponding to 70 kHz and 400 kHz repetition rates for the pump laser are shown in Fig. 2 as the red and blue solid lines, respectively. Note that in the 70 kHz repetition rate case, the short wavelength side of the SC spectrum was limited using a long-pass filter (Northumbria Optical Coating, SLWP-2337) with a cut-on wavelength of 2300 nm. The spectral filter was used to remove the excess noise of the SC source in the 1900 nm band at a lower repetition rate. Note that the sharp features observed at around 2600 nm in the average spectrum obtained for a 70 kHz repetition rate are caused by water vapor absorption present in air. A half-a-meter monochromator (Spectral Products DK480 1/2) was used to measure the SC spectra with a maximal resolution of 1 nm, and a lock-in amplifier (PerkinElmer 7225) was used to increase the signal-to-noise ratio (SNR).

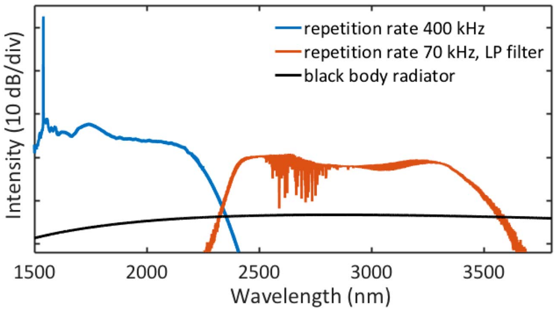

Fig. 2. Supercontinuum spectra corresponding to pump laser repetition rates of 70 (solid red line) and 400 kHz (solid blue line) and used for the photoacoustic spectoscopic measurements of methane and water vapor, respectively. Note that the SC spectrum corresponding to 70 kHz has been spectrally filtered with a long-pass filter with a cut-on wavelength of 2300 nm. The spectrum of the black body radiation source is theoretically estimated based on the temperature of the IR radiator (solid black line).

Light from the SC is collimated into a 2 mm (diameter) beam using a silver reflective collimator and sent to a scanning FTIR interferometer (Bruker IRCube) modulating the spectrum of the light source. For comparison, we also perform reference measurements that use a black body source having a beam diameter of 25 mm are performed with the same FTIR instrument. The order of magnitude smaller beam size of the collimated SC source demonstrates the future potential in miniaturizing the FTIR scanning instrument when used with a spatially coherent light source. At the FTIR output, the beam is focused with a parabolic mirror ($f = 76.2$ mm) into a non-resonant photoacoustic cell (Gasera) that contains the gas sample to be measured. The cell is gold-coated, 10 cm long, and 4.5 mm diameter corresponding to a sample volume smaller than 8 mL. The windows of the cell are made of BaF_2, and a gold-coated mirror is placed right after the back window enabling the optical path length to be increased by a factor of two. Note that the same dual-path cell arrangement was used in all the measurements presented below. The temperature and pressure of the cell were set to 50°C and 1 bar, respectively. The pressure changes inside the cell caused by light absorption in the gas sample are read optically via interferometric detection where a cantilever acts as a moving mirror whose mechanical oscillations change the period of the interference fringes (see Ref. [17] for details on the readout procedure). The cantilever is gold-coated with dimensions of 6 mm, 10 μm, and 1.5 mm (length, thickness, and width, respectively). The FTIR scanning mirror velocity is 1.6 kHz, monitored by a HeNe laser. The modulation frequencies for the considered mid-infrared wavelength range of 1.7–3.5 μm correspond to 600–290 Hz at the optimal frequency range for the CEPAS cell. The gas sample absorption spectrum is obtained by the Fourier transform of the recorded interferogram. The minimum wavelength resolution of the instrument is determined by the FTIR maximum optical path difference of 1 cm.

The experimentally recorded absorption spectrum of normal room air (20°C, RH 30%) water vapor with 7000 ppm concentration in the PAS cell and using the SC source with a repetition of 400 kHz as described above is shown in Fig. 3 (solid blue line). The total SC average power was 414 mW with a power spectral density of 275 μW/nm in the water vapor absorption band, out of which 40% was injected into the CEPAS cell after the FTIR. The spectrum was measured with 1.4 nm resolution and averaged over 10 scans for a total measurement time of 50 s. We observe excellent correspondence with the theoretical spectrum predicted from the HITRAN database (plotted as a mirror image in the figure). For comparison, we also repeated the experiment using the black body radiation source (see the solid black line in Fig. 2 for an illustration of the spectrum). Note that the photoacoustic signal using the black body source has been magnified 10 times in the figure for visualization purposes, showing that the SC yields far better performance in terms of sensitivity and SNR. More specifically, the signal intensity and SNR are increased by a factor of 70 and 13, respectively, when using the SC source.

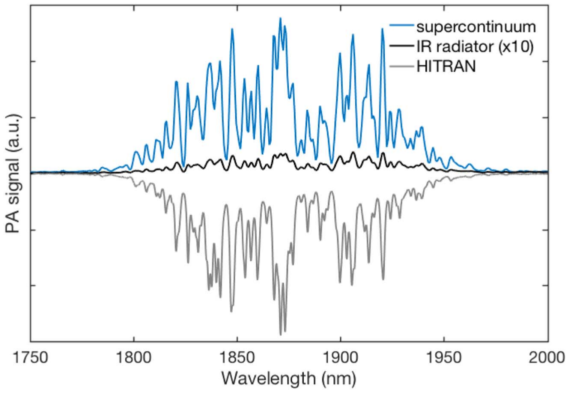

Fig. 3. Experimentally measured absorption spectrum of water vapor with the SC (solid blue line) and black body source (solid black line). The measurement resolution is 1.4 nm, and the spectrum averaged over 10 different scans for both measurements. The theoretical absorption spectrum, as predicted from the HITRAN database, is shown as the mirror image (gray line). Note that the results obtained with the black body have been magnified by 10 for convenient visualization.

We then used the spectrally filtered SC source with a 70 kHz repetition rate to measure the mid-infrared ro-vibrational absorption band of methane sampled from a flow of premixed 400 ppm methane in nitrogen carrier gas. The SC total power in this case (after the filter) was 78 mW with a power spectral density of 71 μW/nm in the absorption band of methane. Again, 40% of this power was finally injected into the CEPAS cell. The results are shown in Fig. 4 (red solid line), where we find excellent agreement with the absorption spectrum predicted from HITRAN. The results from the black body radiation source are also shown in the figure (with a 5 times magnification). As in the case of the water vapor, it is clear that the signal measured when using the SC is significantly increased (19 times), as compared to that obtained with the black body source. However, the increase in the SNR is only 1.8 times in this case, which is due to increased noise in the SC source at a reduced repetition rate. Indeed, there are significant pulse-to-pulse fluctuations in the SC spectrum caused by the initial stage of modulation instability in the SC generating nonlinear dynamics [16], and a lower repetition rate results in an increase in the noise level, as the intensity recorded is then averaged over a reduced number of SC pulses for lower repetition rates.

Besides the increase in the detected signal strength when using the SC source, another significant advantage as compared to a standard black body source lies in the fact that the SC is perfectly spatially coherent and the beam remains collimated independently of the optical path difference used in the FTIR. This means that one can increase the measurement resolution without any line-broadening or shifting effects [18] and still maintain high signal intensity. This is illustrated in Fig. 5 where we show the measured absorption spectrum of methane with different resolutions. The measurement times for resolutions of 1, 2, and 4 nm were 200 s, 100 s, and 50 s, respectively, with corresponding achieved SNRs of 136, 221, and 278. One can see how the lines become sharper, and the signal amplitude is increased for higher resolutions. This contrasts with the use of a spatially incoherent black body source which requires reducing the input aperture size to ensure reasonable collimation over larger distances, thus leading to decreased signal intensities when performing measurements at higher resolutions.

We evaluated the concentration detection limits (3σ, 50 s) to be 2.6 and 1.4 ppm for the black body and SC sources, respectively. The noise level was estimated from the non-absorbing part of the spectrum without methane by dividing the area into 10 blocks each consisting of 10 data points and averaging the standard deviations. The strongest signal value was then compared to the noise level (3σ). The limit of detection was calculated by dividing the concentration by the SNR. The rather low enhancement in the detection limit when using the SC is caused by the high intensity noise level of the supercontinuum source induced by large pulse-to-pulse fluctuations. We anticipate that lower detection limits can be achieved using e.g., a more stable SC source with even higher power spectral density, a resonant acoustic cell, and single-frequency detection, or with a larger measurement setup. Yet, one should consider the detection limits achieved here in the context of broadband measurement from a small sample volume.

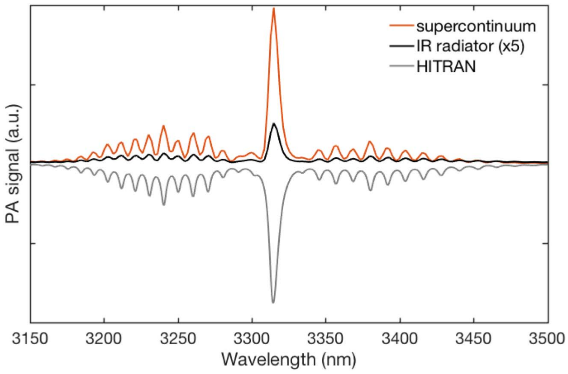

Fig. 4. Experimentally measured absorption spectrum of 400 ppm methane with the SC (red line) and black body source (solid black line). The measurement resolution is 4 nm, and the spectrum averaged over 10 different scans for both measurements. The theoretical absorption spectrum as predicted from the HITRAN database is shown as the mirror image (solid gray line). Note that the results obtained with the black body have been magnified by 5 for convenient visualization.

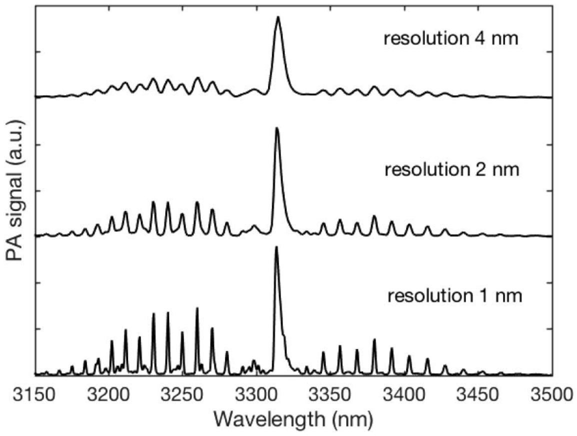

Fig. 5. Measured absorption spectrum of methane for different FTIR resolutions as indicated. The measurement time is inversely proportional to the resolution. The measurement times for resolutions of 1, 2, and 4 nm are 200 s, 100 s, and 50 s, respectively, with corresponding achieved SNRs of 136, 221, and 278.

We have performed broadband CEPAS using a supercontinuum light source and demonstrated the potential of the technique by measuring the absorption spectrum of water vapor and methane in the mid-infrared spectral region. The approach allows for significant improvement in terms of sensitivity and resolution as compared to the use of a conventional black body radiation source. The spatially coherent and collimated SC beam also enables miniaturization of the Fourier transform spectrometer, as the narrow beam can easily be guided even in a small-form-factor instrument. Furthermore, high spatial coherence, in principle, enables multi-pass arrangements through the PAS cell, which could lead to enhanced sensitivity. Lower detection limits may be reached by reducing the intensity noise of the supercontinuum source using for example pump pulses of shorter durations and/or increasing the power spectral density of the supercontinuum source. The measurement time, on the other hand, is mostly limited by the cantilever frequency response which imposes the use of a low scanning speed FTIR. Yet, using a shot-to-shot stable SC source would allow for single scan measurements and improve the measurement speed by an order of magnitude. Our results open up novel perspectives for the development of cost-effective apparatus for broadband gas sensing.

Funding. Academy of Finland (318082); Graduate School of Tampere University of Technology; SPIM Graduate School of University of Burgundy Franche-Comté.

REFERENCES

1. J. Uotila and J. Kauppinen, Appl. Spectrosc. **62**, 655 (2008).
2. J. Kauppinen, K. Wilcken, I. Kauppinen, and V. Koskinen, Microchem. J. **76**, 151 (2004).
3. T. Tomberg, M. Vainio, T. Hieta, and L. Halonen, Sci. Rep. **8**, 1848 (2018).
4. T. Laurila, H. Cattaneo, V. Koskinen, J. Kauppinen, and R. Hernberg, Opt. Express **13**, 2453 (2005).
5. A. A. Kosterev and F. K. Tittel, Appl. Opt. **43**, 6213 (2004).
6. A. Veres, Z. Bozóki, Á. Mohácsi, M. Szakáll, and G. Szabó, Appl. Spectrosc. **57**, 900 (2003).
7. V. Spagnolo, P. Patimisco, S. Borri, G. Scamarcio, B. Bernacki, and J. Kriesel, Opt. Lett. **37**, 4461 (2012).
8. C. B. Hirschmann, J. Lehtinen, J. Uotila, S. Ojala, and R. L. Keiski, Appl. Phys. B **111**, 603 (2013).
9. J. Peltola, M. Vainio, T. Hieta, J. Uotila, S. Sinisalo, M. Metsälä, M. Siltanen, and L. Halonen, Opt. Express **21**, 10240 (2013).
10. K. Wilcken and J. Kauppinen, Appl. Spectrosc. **57**, 1087 (2003).
11. D. Wildanger, E. Rittweger, L. Kastrup, and S. W. Hell, Opt. Express **16**, 9614 (2008).
12. C. Amiot, A. Aalto, P. Ryczkowski, J. Toivonen, and G. Genty, Appl. Phys. Lett. **111**, 061103 (2017).
13. Y. Sych, R. Engelbrecht, B. Schmauss, D. Kozlov, T. Seeger, and A. Leipertz, Opt. Express **18**, 22762 (2010).
14. I. Hartl, X. D. Li, C. Chudoba, R. K. Ghanta, T. H. Ko, J. G. Fujimoto, J. K. Ranka, and R. S. Windeler, Opt. Lett. **26**, 608 (2001).
15. G. Humbert, W. J. Wadsworth, S. G. Leon-Saval, J. C. Knight, T. A. Birks, P. St.J. Russell, M. J. Lederer, D. Kopf, K. Wiesauer, E. I. Breuer, and D. Stifter, Opt. Express **14**, 1596 (2006).
16. J. M. Dudley, G. Genty, and S. Coen, Rev. Mod. Phys. **78**, 1135 (2006).
17. V. Koskinen, J. Fonsen, K. Roth, and J. Kauppinen, Vib. Spectrosc. **48**, 16 (2008).
18. H. Wang, X. Ma, Y. Wang, D. Chen, W. Chen, and Q. Li, Opt. Express **25**, 19077 (2017).

III

SUPERCONTINUUM SPECTRAL-DOMAIN GHOST IMAGING

by
Caroline Amiot, Piotr Ryczkowski, Ari T. Friberg, John M. Dudley & Goëry Genty, October 2018
Optics Letters, vol 43, no. 20, pp. 5025-5028

Optics Letters

Supercontinuum spectral-domain ghost imaging

Caroline Amiot,[1,3,*] Piotr Ryczkowski,[1] Ari T. Friberg,[2] John M. Dudley,[3] and Goëry Genty[1]

[1]Laboratory of Photonics, Tampere University of Technology, Tampere, Finland
[2]Department of Physics and Mathematics, University of Eastern Finland, Joensuu, Finland
[3]Institut FEMTO-ST, UMR 6174 CNRS, Université de Bourgogne Franche-Comté, Besançon, France
*Corresponding author: caroline.amiot@tut.fi

Received 17 July 2018; revised 1 September 2018; accepted 12 September 2018; posted 12 September 2018 (Doc. ID 339943); published 10 October 2018

Ghost imaging is a technique that generates high-resolution images by correlating the intensity of two light beams, neither of which independently contains useful information about the shape of the object. Ghost imaging has been demonstrated in both the spatial and temporal domains, using incoherent classical light sources or entangled photon pairs. Here we exploit the recent progress in ultrafast real-time measurement techniques to demonstrate ultrafast, scan-free, ghost imaging in the frequency domain using a continuous spectrum from an incoherent supercontinuum light source with random spectral fluctuations. We demonstrate the application of this technique to broadband spectroscopic measurements of methane absorption performed with sub-nanometer resolution. Our results offer novel perspectives for remote sensing in low light conditions, or in spectral regions where sensitive detectors are lacking.

OCIS codes: (110.1650) Coherence imaging; (070.7145) Ultrafast processing; (110.2970) Image detection systems; (120.6200) Spectrometers and spectroscopic instrumentation; (320.6629) Supercontinuum generation.

https://doi.org/10.1364/OL.43.005025

Ghost imaging is an unconventional imaging technique that creates the image of an object by correlating two signals: the spatially resolved intensity pattern of a light source incident on the object (a probe pattern) and the total integrated intensity scattered from the object illuminated by those patterns [1,2]. The image is generated by summing over multiple incident patterns, each weighted by the integrated signal scattered by the object. Ghost imaging can be performed using different types of light sources and experimental schemes, including entangled photon pair correlations measured by scanning detectors [3,4], incoherent classical light sources [5–9], and structured light fields recorded by fixed position detectors [10,11].

Significantly, the principle of ghost imaging is not restricted to producing only spatial images and, indeed, ghost imaging has recently been extended into the time domain to measure ultrafast signals on picosecond timescales [12–14]. In the frequency domain, the measurement of wavelength-by-wavelength Hanbury Brown–Twiss intensity correlations of an incoherent superluminescent laser diode has been used to characterize coarse spectral features of chloroform in a proof-of-principle experiment [15]. This approach, however, uses nonlinear detection that requires either a high-power source or very sensitive detection, and it is also experimentally time-consuming as it involves a raster scan approach both in wavelength and time delay.

In this Letter, we introduce a scan-free approach to high-resolution frequency domain ghost imaging that enables the measurement of the spectral transmission (or reflection) of an object using a single-pixel detector without any spectral resolution. The method is ultrafast and broadband, and requires neither a high-power source nor a particularly fast sensitive detector after the object. The technique measures the correlation between the spectrally resolved intensity fluctuation of an incoherent supercontinuum (SC) captured in real-time using dispersive Fourier transform and the integrated intensity after reflection or transmission through the object to be characterized. DFT has recently been applied to many studies in ultrafast nonlinear dynamics for direct spectroscopic measurements, label-free molecular identification, or biomedical diagnostics [16,17], and it is rapidly becoming a standard characterization tool in ultrafast science. As a particular application of our method, we report spectroscopic measurements of methane absorption lines over a 50 nm bandwidth and with sub-nanometer resolution using a simple integrating detector with no spectral resolution. The results are in excellent agreement with direct absorption spectroscopy measurements. In contrast with direct measurements that may require a significant amount of power and/or fast sensitive detectors to measure spatially (or temporally) dispersed signals, spectral ghost imaging measures only the integrated signal after the probed material or sample. This offers great potential for measuring the spectral signature of highly absorbing materials or samples with low-damage threshold, as well as for remote spectral analysis where only a fraction of the illuminated light may be reflected.

Figure 1 introduces the principle of ghost imaging in the spectral domain using a classical light source. Consider an object with wavelength-dependent transmission $T(\lambda)$ which modulates (or modifies) the spectrum of a broadband light beam interacting with this object. Provided the incident light field exhibits random spectral intensity fluctuations, a ghost

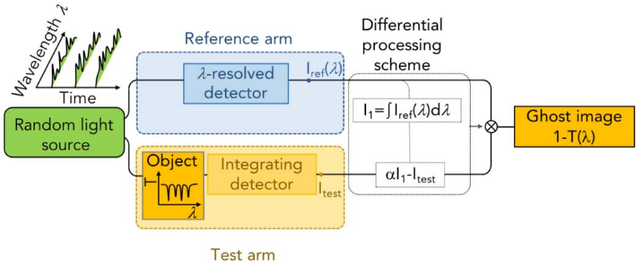

Fig. 1. Ghost imaging in the spectral domain. The wavelength-dependent transmission $T(\lambda)$ of an object is obtained from the correlation of the spectrally resolved fluctuations of a random light source with the spectrally integrated intensity at the object output. Differential detection is numerically implemented to increase the SNR as shown.

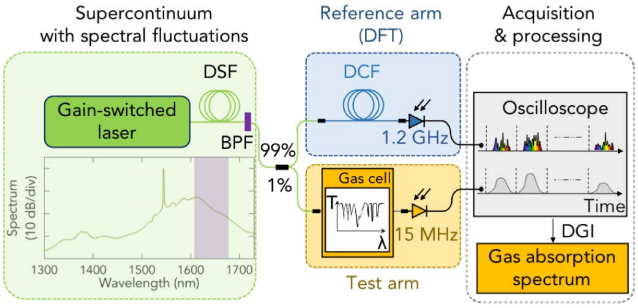

Fig. 2. Experimental setup. DSF, dispersion-shifted fiber; BPF, bandpass filter; DCF, dispersion compensating fiber; DGI, differential ghost imaging. The violet rectangle represents the portion of the SC spectrum after the bandpass filter.

image of the object spectral response can be generated from the normalized correlation function $C(\lambda)$ defined by

$$C(\lambda) = \frac{\langle \Delta I_{\text{ref}}(\lambda) \cdot \Delta I_{\text{test}} \rangle_N}{\sqrt{\langle [\Delta I_{\text{ref}}(\lambda)]^2 \rangle_N \langle [\Delta I_{\text{test}}]^2 \rangle_N}}. \tag{1}$$

Physically, $C(\lambda) = 1 - T(\lambda)$ represents the correlation between multiple measurements of the spectral intensity fluctuations in a reference arm $I_{\text{ref}}(\lambda)$ and the total (or integrated) wavelength-independent intensity I_{test} in the test arm where light interacts with the object. Here $\langle\rangle_{\text{N}}$ denotes ensemble average over distinct N realizations, and $\Delta I = I - \langle I \rangle_N$. Note that in Fig. 1 we consider wavelength-dependent transmission, but the same analysis applies for reflection.

Using this approach, we aim to generate a "ghost image" of the absorption spectrum of gas molecules. In this case, the spectral object which we desire to characterize (the absorption spectrum) is "sparse" in the sense that the absorption lines are significantly narrower than the spectral window of the measurement so that the gas molecules only impart very small changes in the total transmitted light. In order to increase the signal-to-noise ratio (SNR) and reduce the number of measurements, we adopt a differential processing scheme which has the advantage of being sensitive only to the fluctuating part of the transmission [18,19]. The differential detection is a numerical post-processing scheme originally developed in the spatial domain and which is similar to performing balanced detection in the test arm. It is realized by replacing the integrated intensity in the test arm with a numerically generated differential signal $\alpha \int I_{\text{ref}}(\lambda)d\lambda - I_{\text{test}}$ where $\alpha = \langle I_{\text{test}} \rangle_N / \langle \int I_{\text{ref}}(\lambda)d\lambda \rangle_N$.

Our experimental setup is shown in Fig. 2. The light source is a spectrally filtered broadband incoherent SC generated by injecting 1 kW, 700 ps pulses at 1547 nm with a 100 kHz repetition rate (Keopsys-PEFL-K09) into a 6 m long DSF with zero-dispersion wavelength at 1510 nm (Corning Inc LEAF). The SC bandwidth at the output of the DSF extends from c.a. 1300 to over 1700 nm. The relatively long pump pulses used to generate the SC leads to significant shot-to-shot spectral fluctuations caused by an initial stage of modulation instability [20], and it is these random spectral fluctuations that are used in our ghost imaging setup. The SC is filtered in the 1610–1670 nm range with a 50 nm (full-width at half-maximum) bandwidth filter (Spectrogon NB-1650-050). This is to ensure fidelity in the real-time measurements of the spectral fluctuations that may be otherwise distorted because of the attenuation (beyond 1670 nm) and third-order dispersion in the dispersion compensating fiber (DCF) used to perform the DFT. We also specifically adjust the peak power of the pump pulses injected into the DSF in order to maximize the amplitude of the SC spectral fluctuations, which reduces the digitization noise on the oscilloscope and yields an improved SNR when measuring in real time these fluctuations with the DFT technique.

The intensity of the SC source is divided between the reference and test arms unequally with a 99/1 fiber coupler. In the reference arm, the spectral fluctuations are measured in real time using the DFT approach with 0.2 nm resolution, which also sets the resolution of the spectral-domain ghost imaging scheme. The spectral fluctuations are converted into the time domain by a DCF (FS.COM customized 150 km DCF) with total dispersion of 3000 ps × nm^{-1} and measured with a 1.2 GHz InGaAs photodetector (Thorlabs DET01CFC/M) and 20 GHz real-time oscilloscope (Tektronics DSA72004) with 50 GS/s sampling rate.

In the test arm, the spectral object is a fiber-based gas cell (Wavelength References FCS-16-1/4) filled with methane at atmospheric pressure and room temperature. The absorption lines of the 2v3 overtone transition of methane [21] in the spectral range of the filtered SC acts as the spectral object modulating the randomly fluctuating light. Light transmitted through the cell is measured by an integrating photodetector with 50 ns response time (15 MHz bandwidth, Thorlabs PDA10D2) which, alone, cannot resolve any spectral feature of the gas absorption. Multiple single-shot realizations are simultaneously recorded by the oscilloscope, and the differential detection scheme described above is applied in post-processing.

The experimentally recorded spectral fluctuations are shown in Fig. 3. In particular, Fig. 3(c) shows a selection of four different single-shot spectra measured from the reference arm where one can clearly observe significant fluctuations of the spectral intensity. The effective bandwidth here is ≈0.2 nm as seen in the expanded portion in Fig. 3(b). The average spectral envelope of the filtered spectrum over a large number of consecutive single-shot spectra is shown as the black solid line in Fig. 3(a), with this envelope being essentially determined by the transmission curve of the 50 nm bandpass filter. In order to obtain a ghost image with a large SNR over the measurement spectral range, the variance of the fluctuations should be as large as possible across the measurement spectral window to minimize the DC component recorded by both detectors.

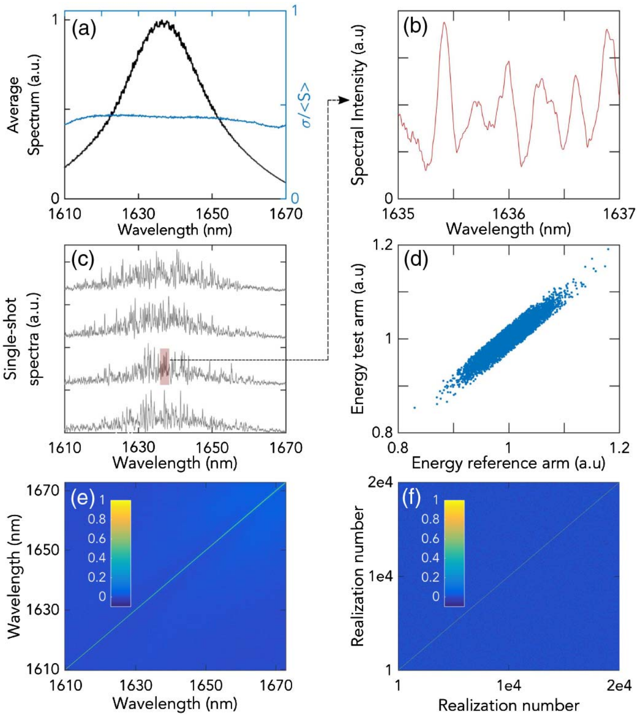

Fig. 3. Spectral fluctuations of the incoherent SC source. (a) Average spectrum (black line) and relative standard deviation of the fluctuations (blue line). (b) Expanded view of the fluctuations over a 2 nm span shown as the highlighted red rectangle in (c). (c) Four selected examples of recorded single-shot spectra using the DFT technique. (d) Correlation between the single-shot spectra energy measured from the reference arm and the energy measured at the gas cell output by the integrating detector. (e) Wavelength-to-wavelength correlations of the filtered SC source measured over 20,000 single-shot spectra. (f) Correlations of the normalized (by the mean spectrum) shot-to-shot fluctuations.

The input pump power used to generate the SC was thus specifically optimized to meet this condition, as shown in Fig. 3(a), where the standard deviation of the spectral fluctuations relative to the average spectrum (solid blue line) is close to 50% across the full (filtered) bandwidth. One can also see that the fluctuations variance is not uniform and follows the envelope of the Gaussian bandpass filter, resulting in the distortion of the ghost image. Furthermore, the spectral response of the experimental setup components varies as a function of wavelength over the 50 nm spectral window of the measurements, and this also distorts the ghost image. In order to remove the distortion induced by both the Gaussian bandpass filter and the experimental setup spectral response, we apply a low-pass filter to the correlation function in the Fourier space, i.e., we multiply the Fourier transform of the correlation function by a narrowband notch function centered over the zero frequency of the Fourier transform. This post-processing effectively suppresses the slowly varying distortion, as compared to the rapidly varying gas absorption features.

Ghost imaging relies on the fact that the reference and test beams are perfectly correlated so that a variation measured in the test arm intensity is caused by the change in the fluctuations of the probe in the reference arm. In the case of a sparse object for which the variations in the spectrally integrated transmission are small from one realization to another, the integrated intensities measured at the output of the test and reference arms should be nearly fully correlated. For our experiments, this is verified in Fig. 3(d) where we can see how the two are indeed very well correlated (Pearson correlation coefficient of $\rho = 0.946$). The random nature of the spectral fluctuations is conveniently visualised in Fig. 3(e), where we plot the wavelength-to-wavelength Pearson correlations [22] of a measured ensemble of 20,000 single shot spectra. The plot shows a high degree of correlation only on the diagonal of the false color plot, clearly indicating that there are no correlations in the spectral fluctuations which is another prerequisite for ghost imaging. Finally, we also emphasize that there are no correlations in the fluctuations (normalized to the mean spectum) from shot to shot, as illustrated Fig. 3(f), which is also one of the requirements in ghost imaging.

The ghost spectral image of the methane absorption lines obtained from 20,000 single-shot SC spectra is shown in Fig. 4 as a solid blue line. For comparison, a direct measurement of the gas absorption using the same filtered SC source and a conventional optical spectrum analyzer with 0.2 nm resolution is also plotted (solid red line). Both the ghost image and the direct measurement are low-pass filtered in the Fourier domain to remove the distortion from the SC spectral envelope. We can see remarkable agreement over the full 50 nm spectral range of the overtone transitions, with the resolution of the ghost imaging very close to that of the direct measurement. The residual negative normalized absorption is an artifact that arises from the post-processing Fourier filtering step. For completeness, we also show in the figure inset the ghost image obtained from the correlation of the reference and test arms without the numerical differential scheme implementation and for the same number of 20,000 realizations. As could be expected for a sparse object, no obvious spectral signature of the gas is observed and we can see how the differential post-processing is extremely powerful in revealing the absorption lines with yet a limited number of realizations.

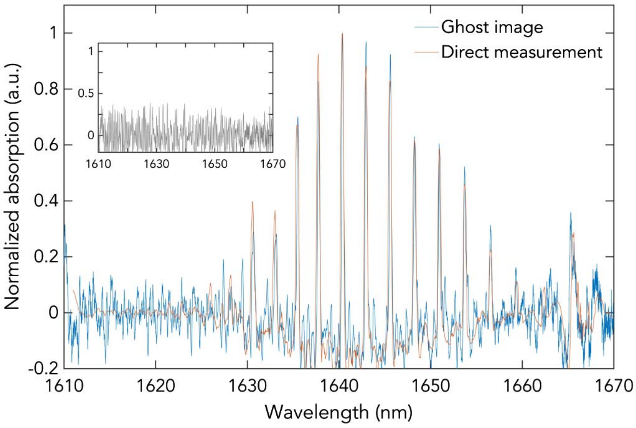

Fig. 4. Experimental ghost image of the 2v3 overtone transition of methane generated from 20,000 realizations using the numerical differential scheme (solid blue line). A direct measurement performed with the SC source and an optical spectrum anaylzer are shown for comparison (solid red line). The inset plots the experimental ghost image without the differential scheme implementation.

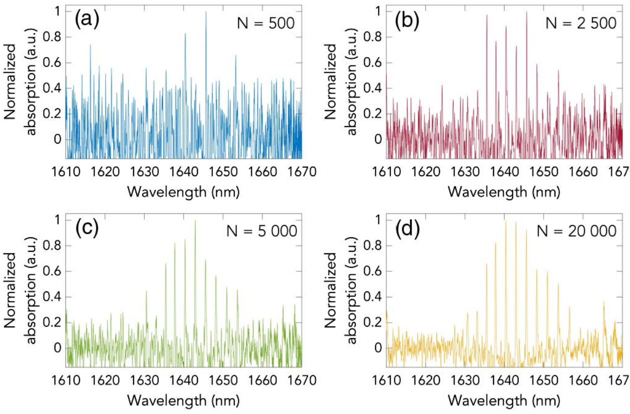

Fig. 5. Ghost image of the methane absorption lines for an increasing number of realizations, as indicated in the sub-panels.

The DFT method employed here to measure in real time the spectral fluctuations allows for fast data acquisition rates. This means that with the 100 kHz repetition rate SC source used, it only takes 200 ms to record the 20,000 realizations and to retrieve the absorption spectrum of the gas. Significantly, even with a much lower number of realizations, the absorption lines are resolved by the ghost measurement, and this is illustrated in Fig. 5, where we show the ghost spectral image obtained for an increasing number of realizations (and using the DGI post-processing). The SNR increases with the number of measurements; yet, one can see how the main absorption lines are already resolved with as little as 2,500 measurements. Note that because the spectral fluctuations are random, obtaining a ghost image with a high SNR requires the use of a larger number of distinct realizations, as compared to a computational or compressive sensing approach where the realizations are orthogonal to each other [1].

We have demonstrated fast, broadband, and scan-free ghost imaging in the spectral domain using an incoherent SC light source with large shot-to-shot spectral fluctuations. We have applied the technique to perform high-resolution spectroscopic measurements of the absorption spectrum of methane in the 1600 nm wavelength range. The current resolution of this technique is limited by the precision with which the linewidth of spectral fluctuations in the reference arm can be measured in real time. Using a dispersive fiber with larger total dispersion and/or a detector with higher bandwidth, in combination with a tailored SC source, we anticipate that picometer or even subpicometer resolution could be reached. A significant benefit of spectral ghost imaging is that one measures only the integrated signal after the probed material or sample. This feature may be advantageously exploited to perform spectroscopic measurements of highly absorbing samples or for distant measurements when only a fraction of the illuminated light may be reflected due to strong scattering, for example. The ghost imaging scheme could also be of interest in wavelength regions where there are no fast sensitive detectors. In this case, the random spectral fluctuations may be measured in real time in a spectral range where fast detectors exist, after frequency upconversion (only applied to the reference arm) via second-harmonic generation in a nonlinear crystal or four-wave mixing in a nonlinear waveguide. Furthermore, one could remove the need for measuring in real time the random spectral fluctuations by using a light source where the spectral fluctuations are actively controlled and pre-programmed, which could be realized using, for example, a frequency comb and a waveshaper. Such a computational spectral ghost imaging approach would also reduce the number of realizations required to obtain spectroscopic measurements with a high SNR. Finally, it is important to stress that, in contrast to direct measurement configurations, the method is insensitive to linear spectral and temporal distortions occurring between the object and the detector [13].

Funding. Tampereen Teknillinen Yliopisto (TTY); SPIM, University of Franche-Comté (UFC); Academy of Finland (298463); Investissements d'Avenir [ISITE-BFC (ANR-15-IDEX-0003)].

Acknowledgment. C. Amiot acknowledges the support from TUT and SPIM graduate schools. J. Dudley acknowledges the support from the French Investissements d'Avenir program, project ISITE-BFC. G. Genty acknowledges the support from the Academy of Finland.

REFERENCES

1. B. I. Erkmen and J. H. Shapiro, Adv. Opt. Photon. **2**, 405 (2010).
2. M. J. Padgett and R. W. Boyd, Philos. Trans. R. Soc. London Ser. A **375**, 20160233 (2017).
3. R. S. Bennink, S. J. Bentley, R. W. Boyd, and J. C. Howell, Phys. Rev. Lett. **92**, 033601 (2004).
4. T. B. Pittman, Y. H. Shih, D. V. Strekalov, and A. V. Sergienko, Phys. Rev. A **52**, R3429 (1995).
5. R. S. Bennink, S. J. Bentley, and R. W. Boyd, Phys. Rev. Lett. **89**, 113601 (2002).
6. A. Gatti, E. Brambilla, M. Bache, and L. A. Lugiato, Phys. Rev. A **70**, 1 (2004).
7. F. Ferri, D. Magatti, A. Gatti, M. Bache, E. Brambilla, and L. A. Lugiato, Phys. Rev. Lett. **94**, 183602 (2005).
8. D. J. Zhang, H. G. Li, Q. L. Zhao, S. Wang, H. B. Wang, J. Xiong, and K. Wang, Phys. Rev. A **92**, 013823 (2015).
9. F. Devaux, P.-A. Moreau, S. Denis, and E. Lantz, Optica **3**, 698 (2016).
10. B. Sun, M. P. Edgar, R. Bowman, L. E. Vittert, S. Welsh, A. Bowman, and M. J. Padgett, Science **340**, 844 (2013).
11. R. I. Stantchev, B. Sun, S. M. Hornett, P. A. Hobson, G. M. Gibson, M. J. Padgett, and E. Hendry, Sci. Adv. **2**, e1600190 (2016).
12. T. Shirai, T. Setälä, and A. T. Friberg, J. Opt. Soc. Am. B **27**, 2549 (2010).
13. P. Ryczkowski, M. Barbier, A. T. Friberg, J. M. Dudley, and G. Genty, Nat. Photonics **10**, 167 (2016).
14. P. Ryczkowski, M. Barbier, A. T. Friberg, J. M. Dudley, and G. Genty, APL Photon. **2**, 046102 (2017).
15. P. Janassek, S. Blumenstein, and W. Elsäßer, Phys. Rev. Appl. **9**, 021001 (2018).
16. K. Goda and B. Jalali, Nat. Photonics **7**, 102 (2013).
17. A. Mahjoubfar, D. V. Churkin, S. Barland, N. Broderick, S. K. Turitsyn, and B. Jalali, Nat. Photonics **11**, 341 (2017).
18. F. Ferri, D. Magatti, L. A. Lugiato, and A. Gatti, Phys. Rev. Lett. **104**, 253603 (2010).
19. B. Sun, S. S. Welsh, M. P. Edgar, J. H. Shapiro, and M. J. Padgett, Opt. Express **20**, 16892 (2012).
20. J. M. Dudley, G. Genty, and S. Coen, Rev. Mod. Phys. **78**, 1135 (2006).
21. J. M. Hollas, *Modern Spectroscopy* (Wiley, 2004).
22. T. Godin, B. Wetzel, T. Sylvestre, L. Larger, A. Kudlinski, A. Mussot, A. Ben Salem, M. Zghal, G. Genty, F. Dias, and J. M. Dudley, Opt. Express **21**, 18452 (2013).

IV

GHOST OPTICAL COHERENCE TOMOGRAPHY

by
Caroline Amiot, Piotr Ryczkowski, Ari T. Friberg, John M. Dudley & Goëry Genty, Submitted to Optics Letters

Ghost Optical Coherence Tomography

CAROLINE G. AMIOT[1,3,*], **PIOTR RYCZKOWSKI**[1], **ARI T. FRIBERG**[2], **JOHN M. DUDLEY**[3], **AND GOËRY GENTY**[1]

[1] *Laboratory of Photonics, Tampere University of Technology, Tampere, Finland*
[3] *Department of Physics and Mathematics, University of Eastern Finland, Joensuu, Finland*
[3] *Institut FEMTO-ST, UMR 6174 CNRS, Université de Bourgogne Franche-Comté, Besançon, France*
[*] *Corresponding author: caroline.amiot@tut.fi*

Compiled October 9, 2018

We demonstrate experimentally ghost optical coherence tomography using a broadband incoherent supercontinuum light source with shot-to-shot random spectral fluctuations. The technique is based on ghost imaging in the spectral domain where the object is the spectral interference pattern generated from an optical coherence tomography interferometer in which a physical sample is placed. The image of the sample is obtained from the Fourier transform of the correlation between the spectrally-resolved intensity fluctuations of the supercontinuum and the integrated signal measured at the output of the interferometer. The results are in excellent agreement with measurements obtained from a conventional optical coherence tomography system.

http://dx.doi.org/10.1364/ao.XX.XXXXXX

---

1. INTRODUCTION

Optical coherence tomography (OCT) is an interferometric imaging technique commonly used to obtain images of materials with high in-depth resolution [1–3] and it is commonly employed for industrial characterization of materials and components [4]. Due to its non-invasive character and the absence of ionizing radiation or toxic contrast agents in its implementation, OCT has also found multiple medical applications and it is now widely used in retinal, skin, and blood vessel examination [5, 6]. A particular variant of OCT is performed in the spectral (wavelength) domain, based on measuring the phase relation between different wavelength components of a broadband light source in order to determine the distance to the sample under test [7]. A major benefit of spectral-domain OCT is that it does not require scanning along the sample direction allowing for significantly faster acquisition speeds compared to its time-domain counterpart. Spectral-domain OCT has been demonstrated using various types of light sources including broadband stationary and pulsed sources or swept-wavelength sources [8]. In parallel to the rapid development in OCT technologies, there has also been much recent interest in the unconventional imaging technique known as ghost imaging. Ghost imaging is based on the principle of image creation from the correlation between a known structured pattern that illuminates an object and the total integrated intensity transmitted (or reflected) by the object [9, 10]. The defining feature of ghost imaging is that neither of the beams alone actually carries enough information to reconstruct the image. Rather, it is only by correlating the two measurements of the structured illuminating source and the integrated intensity from the object that an image can be generated. In this regard, the fact that the light actually detected from the object is an integrated intensity has also led to ghost imaging to be referred to as single-pixel imaging. A significant advantage of ghost imaging when compared to conventional imaging is that it is insensitive to distortions of the wavefront occurring after the object as only the total light intensity is measured [11], making it ideal for measurements in turbid media or in the presence of other noise. Ghost imaging can be performed using light sources with random spatial intensity patterns [12] or patterns which are controlled using e.g. programmable digital micro-mirrors [13–16]. Ghost imaging has also been extended to the temporal domain [17, 18] and very recently in the frequency domain for real-time broadband greenhouse-gas spectroscopic measurements [19].

2. EXPERIMENTS

In this work, we combine the technique of OCT with the concept of spectral-domain ghost imaging to introduce a new methodology of ghost optical coherence tomography. This method generates a “ghost” spectral interferogram from the correlation between the spectrally-resolved intensity fluctuations of the light source and the integrated signal measured at the output of an OCT interferometer where a physical sample is placed. As in conventional OCT, the image of the sample is then retrieved from the Fourier transform of the interferogram. As a proof-of-principle demonstration, we (i) characterize the relative displacement of a perfectly reflecting mirror and (ii) perform measurement of the thickness of a microscope cover glass. The results are in excellent agreement with those obtained from a conventional OCT setup. A significant advantage of the ghost OCT scheme is that it does not require any particularly sensitive detector or spectrometer at the interferometer output. This could be extremely useful in situations where the object to be measured is highly absorbing or diffusing, for samples with low damage threshold or and for imaging in spectral regions where sensitive detectors are not available.

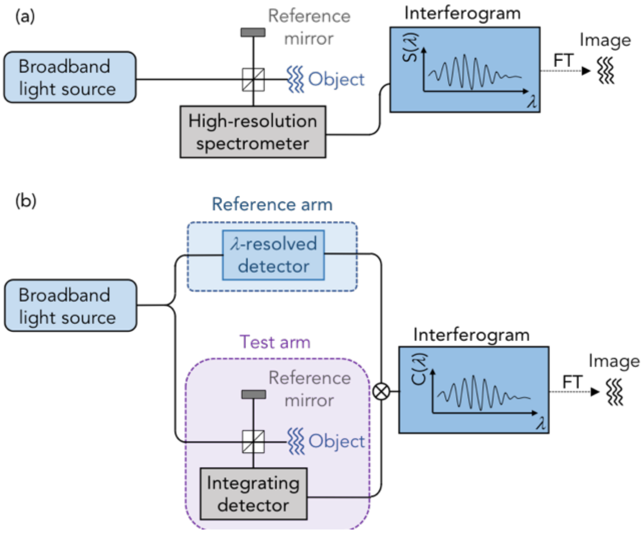

Fig. 1. Schematic illustration of (a) a conventional spectral-domain OCT system and (b) the ghost spectral-domain OCT scheme. FT: Fourier transform.

We begin by illustrating the concept of ghost spectral-domain OCT. To this end, Figure 1 compares the schematics of a conventional spectral-domain OCT system (1a) and that of the ghost spectral-domain OCT approach (1b). In a conventional OCT system, the beam from a broadband light source is equally divided between the two arms of an equal path Michelson interferometer. The image of the object inserted in one arm is generated by measuring with a high-resolution spectrometer the spectral interference pattern resulting from the superposition of the beams reflected from the reference mirror and object.

The axial resolution of the system is inversely proportional the spectral bandwidth of the source as z = 0.4402/(for a Gaussian spectral envelope) where 0 is the light source center wavelength. The imaging depth on the other hand is set by the spectrometer resolution. In spectral-domain ghost OCT, the beam from a light source with random spectral intensity fluctuations is divided between a reference arm where the fluctuations are measured in real time and a test arm consisting of a Michelson interferometer where the object to be measured is placed. The high-resolution spectrometer at the output of the interferometer is replaced by a slow integrating detector with no spectral resolution. The 'ghost' spectral interference pattern produced by the presence of object in the interferometer is then given by the normalized correlation function C() between the reference and test arm signals defined by:

$$C(\lambda) = \frac{\langle \Delta I_{ref}(\lambda) . \Delta I_{test} \rangle_N}{\sqrt{\langle \Delta I_{ref}(\lambda)^2 \rangle \langle \Delta I_{test}^2 \rangle}}. \qquad \textbf{(1)}$$

Specifically, the normalized wavelength-dependent correlation function $C()$ represents correlation between multiple measurements of the spectral intensity fluctuations in the reference arm $I_{ref}()$ and the total (or integrated) wavelength-independent intensity I_{test} in the test arm at the output of the interferometer. $\langle \rangle_N$ denotes ensemble average over distinct N realizations, and $\Delta I = I - \langle I \rangle_N$. The axial resolution z of the ghost OCT scheme is identical to that of the conventional OCT and the imaging depth is now determined by the resolution with which the spectral intensity fluctuations are measured. Figure 2 shows our experimental setup. The light source is a spectrally incoherent SC extending from ~ 1300 to over 1700 nm and generated by launching 1 kW, 700 ps pulses at 1547 nm with 100 kHz repetition rate (Keopsys-PEFL-K09) into a 6-m long dispersion-shifted fiber (DSF) with zero-dispersion wavelength at 1510 nm (Corning Inc LEAF). The SC generating dynamics arise from noise-seeded modulation instability and soliton dynamics [20] resulting in large and random shot-to-shot spectral fluctuations across the entire SC spectrum [21]. These spectral fluctuations produce the (random) structured patterns that are used to probe the spectral OCT interferogram. Light from the SC source is divided between the reference and test arms with a 99/1 fiber coupler. In the reference arm, the spectral fluctuations are measured in real time using the dispersive Fourier transform technique [22, 23]. Specifically, the single-shot spectra are converted into the time domain by a 150 km dispersion compensating fiber (DCF, FS.COM customized 150 km) with total dispersion of 3000 ps.nm-1 and measured with 0.2 nm resolution using a 1.2 GHz InGaAs photodetector (Thorlabs DET01CFC/M) and 20 GHz real-time oscilloscope (Tektronics DSA72004) with 6.5 GS/s sampling rate. In order to avoid spectral distortion in the DCF due to attenuation and third-order dispersion, we restrict the SC bandwidth to the 1610–1670 nm range with a bandpass filter (Spectrogon NB-1650-050) corresponding to an axial resolution of ~ 20 m. In the test arm, light is directed to a standard interferometer whose output intensity is measured with a slow photodetector (15 MHz bandwidth, Thorlabs PDA10D2). We emphasize that this simple detector cannot resolve the spectral interference pattern arising from an optical path difference between the two arms of the interferometer. The single-shot SC spectra from the reference arm and the corresponding spectrally integrated signal from the interferometer are recorded simultaneously by the oscilloscope. The correlation between these two computed over multiple realizations then yields the spectral interferogram whose Fourier transform gives the optical path difference between the interferometer arms.

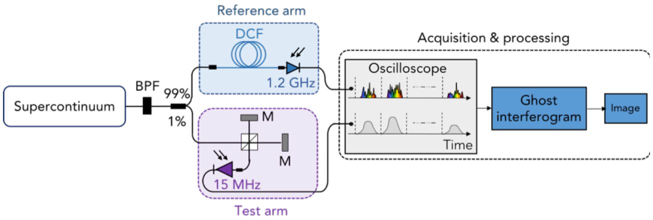

Fig. 2. Experimental setup. BPF: band-pass filter, DCF: dispersion compensating fiber. M: mirror.

A. Results and discussion

We first demonstrate the operating principle of ghost OCT by displacing the position of one of the interferometer mirrors from the zero-path difference position. The OCT interferogram is generated from the correlation function between the spectrally-integrated intensity measured at the interferometer output and the intensity of the single-shot SC spectra. The optical path difference between the two interferometer arms is then simply obtained from the Fourier transform of the interferogram. The results are plotted in Fig. 3a for increasing optical path difference between the mirrors. For comparison, we repeated the same measurements using the conventional OCT scheme by replacing the slow detector at the output of the OCT interferometer with a high-resolution optical spectral analyzer (OSA). The interferogram in this case is measured directly by the OSA and the reference arm measurements are not needed. The results are shown in Fig. 3(b) and we can see the excellent correspondence between the ghost and conventional OCT schemes across the full range of measured optical path differences.

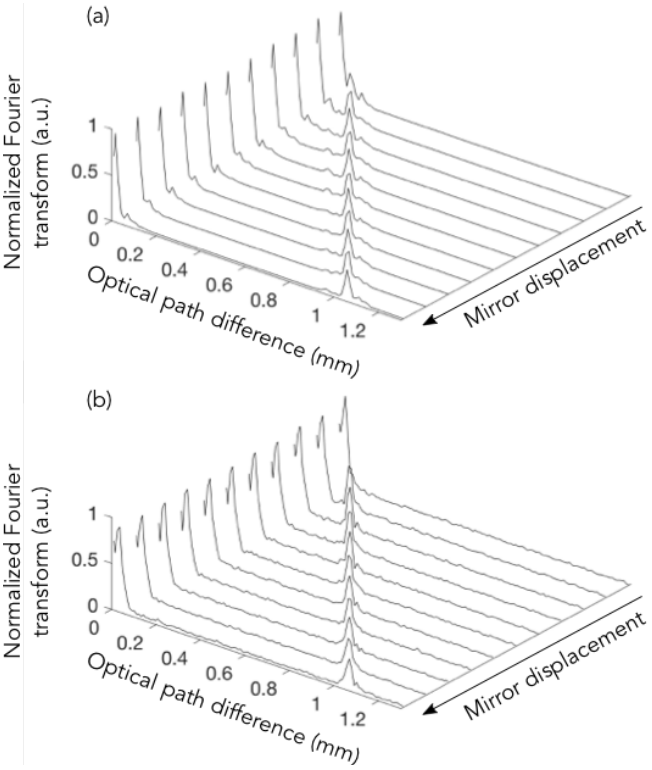

Fig. 3. Optical path difference between the two arms of the Michelson interferometer measured by (a) the ghost OCT configuration and (b) conventional OCT. The arrow indicates the direction of the mirror displacement increasing the optical path difference.

In ghost imaging, the signal-to-noise (SNR) increases with the number of realizations used to compute the correlation, and we illustrate this in Fig. 4 where we show how the Fourier transform of the interferogram evolves as a function of the number of distinct SC pulses for a specific optical path difference (c.a. 0.55 mm in this case) in the interferometer. We can see that even with as few as 200 realizations corresponding to a total recording time of less than 2 ms, and although the SNR is not especially high, the interference fringes are already visible and the optical path difference can be retrieved. For a larger number of realizations, the SNR increases with the square of the number of realizations.

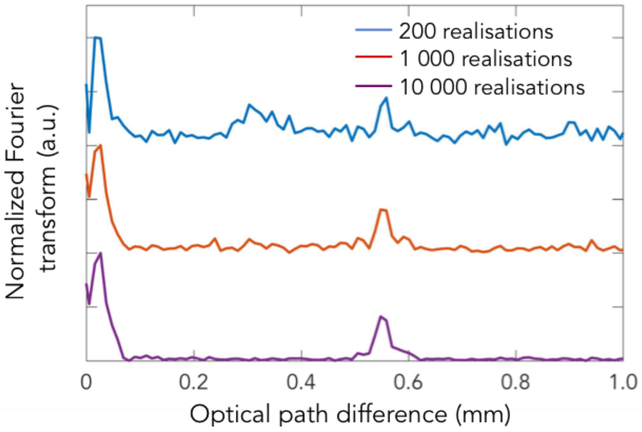

Fig. 4. Normalized Fourier transform of the ghost interferogram for an optical path difference of 0.55 mm between the two arms of the interferometer and for an increasing number of realizations as indicated.

We next performed a second series of experiments using a dual-interface sample. For this purpose, we replaced one of the mirrors in the interferometer by a 210 m thick (optical thickness) microscope cover slip consisting of two air-glass interfaces and the optical path difference between the two arms was set to be c.a. 1mm. The Fourier transform of the resulting interferogram is shown in Fig. 5 both for the conventional OCT system (Fig. 5a) and the ghost OCT setup (Fig. 5b). The results are again in excellent agreement and the positions of the two air-glass interfaces can be clearly identified. The distance between the two interfaces is measured to be 220 m (optical thickness) close to the nominal value of 210 m provided by the manufacturer.

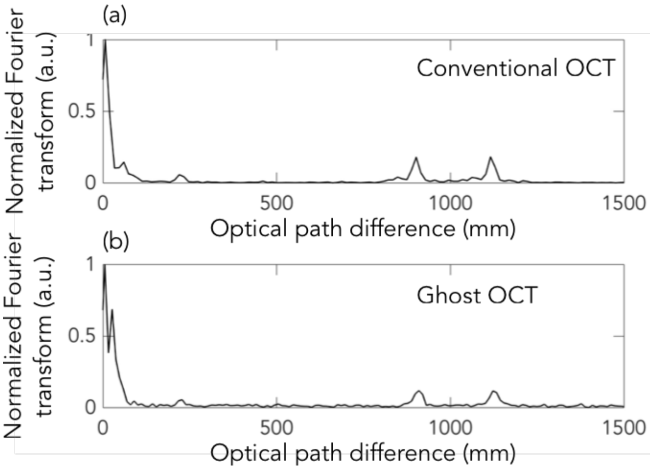

Fig. 5. Optical path difference measured by (a) conventional OCT and (b) the ghost OCT configuration when one of the mirrors is replaced by a 210 m microscope cover slip (optical thickness).

3. CONCLUSIONS

In conclusion, we have experimentally demonstrated proof-of-concept ghost OCT in the spectral domain using a broadband, spectrally incoherent, supercontinuum source. As in a conventional OCT setup, the resolution is determined by spectral bandwidth of the source. The imaging depth on the other hand is given by the spectral resolution with which the spectral fluctuations of the light source can be measured in real time (and therefore the total dispersion if fiber dispersive Fourier transform is used). No particularly sensitive detector or spectrometer is needed at the interferometer output, which could be a significant advantage when the object is highly absorbing or diffusing, when the sample under has a low damage threshold and does not tolerate high intensity, or for imaging in spectral regions where sensitive detectors are not available. Finally, we note that the method can be implemented both with classical light sources and entangled photon sources and that a computational version may be realized by using e.g. controllable frequency combs which would eliminate for the need of single shot spectral measurements to perform the correlation.

C.A. acknowledges the support from TUT and SPIM graduate schools. J.M.D. acknowledges support from the French Investissements d'Avenir program, project ISITE-BFC (contract ANR-15-IDEX-0003). G.G. acknowledges the support from the Academy of Finland (grant 298463).

REFERENCES

1. A. F. Fercher, W. Drexler, C. K. Hitzenberger, and T. Lasser, Reports on progress physics **66**, 239 (2003).
2. B. Bouma, *Handbook of optical coherence tomography* (CRC Press, 2001).
3. W. Drexler and J. G. Fujimoto, *Optical coherence tomography: technology and applications* (Springer Science & Business Media, 2008).
4. C. O'Mahony, M. Hill, M. Brunet, R. Duane, and A. Mathewson, Meas. Sci. Technol. **14**, 1807 (2003).
5. W. Drexler, U. Morgner, F. Kärtner, C. Pitris, S. Boppart, X. Li, E. Ippen, and J. Fujimoto, Opt. letters **24**, 1221 (1999).
6. A. G. Podoleanu, G. M. Dobre, and D. A. Jackson, Opt. Lett. **23**, 147 (1998).
7. J. F. De Boer, B. Cense, B. H. Park, M. C. Pierce, G. J. Tearney, and B. E. Bouma, Opt. letters **28**, 2067 (2003).
8. D. P. Popescu, C. Flueraru, Y. Mao, S. Chang, J. Disano, S. Sherif, M. G. Sowa *et al.*, Biophys. reviews **3**, 155 (2011).
9. B. I. Erkmen and J. H. Shapiro, Adv. Opt. Photonics **2**, 405 (2010).
10. M. J. Padgett and R. W. Boyd, Phil. Trans. R. Soc. A **375**, 20160233 (2017).
11. D. Shi, C. Fan, P. Zhang, J. Zhang, H. Shen, C. Qiao, and Y. Wang, Opt. Express **20**, 27992 (2012).
12. K. W. C. Chan, M. N. O'Sullivan, and R. W. Boyd, Phys. Rev. A **79**, 033808 (2009).
13. R. S. Bennink, S. J. Bentley, R. W. Boyd, and J. C. Howell, Phys. review letters **92**, 033601 (2004).
14. R. S. Bennink, S. J. Bentley, and R. W. Boyd, Phys. Rev. Lett. **89**, 113601 (2002).
15. F. Ferri, D. Magatti, A. Gatti, M. Bache, E. Brambilla, and L. A. Lugiato, Phys. review letters **94**, 183602 (2005).
16. B. Sun, M. P. Edgar, R. Bowman, L. E. Vittert, S. Welsh, A. Bowman, and M. Padgett, Science **340**, 844 (2013).
17. P. Ryczkowski, M. Barbier, A. T. Friberg, J. M. Dudley, and G. Genty, Nat. Photonics **10**, 167 (2016).
18. F. Devaux, P.-A. Moreau, S. Denis, and E. Lantz, Optica **3**, 698 (2016).
19. C. Amiot, P. Ryczkowski, A. T. Friberg, J. M. Dudley, and G. Genty, Opt. Lett. (in press) (2018).
20. J. M. Dudley, G. Genty, and S. Coen, Rev. modern physics **78**, 1135 (2006).
21. B. Wetzel, A. Stefani, L. Larger, P.-A. Lacourt, J.-M. Merolla, T. Sylvestre, A. Kudlinski, A. Mussot, G. Genty, F. Dias *et al.*, Sci. reports **2**, 882 (2012).
22. K. Goda and B. Jalali, Nat. Photonics **7**, 102 EP (2013).
23. A. Mahjoubfar, D. V. Churkin, S. Barland, N. Broderick, S. K. Turitsyn, and B. Jalali, Nat. Photonics **11**, 341 (2017).

Tampereen teknillinen yliopisto
PL 527
33101 Tampere

Tampere University of Technology
P.O.B. 527
FI-33101 Tampere, Finland

ISBN 978-952-15-4273-2

ISSN 1459-2045